

Design and Optimization of ‘Smart’ Nanoparticles for Targeting of the STING Pathway with
Applications in Cancer Immunotherapy

By

Daniel Shae

Dissertation

Submitted to the Faculty of the
Graduate School of Vanderbilt University
in partial fulfillment of the requirements

for the degree of

DOCTOR OF PHILOSOPHY

in

Chemical and Biomolecular Engineering

March 31, 2019

Nashville Tennessee

Approved:

Date

John T. Wilson, Ph.D

Justin M. Balko, Pharm.D, Ph.D

Paul E. Laibinis, Ph.D

Jeffrey C. Rathmell, Ph.D

Scott A. Guelcher, Ph.D

Acknowledgements

First, I would like to thank my advisor Professor John T. Wilson for his guidance throughout my graduate school career. Your willingness to always keep your office door open for brainstorming sessions as well as your tireless search for funding to sustain this research has built this lab from the ground up. This has been a truly special environment to be a graduate student: one in which I felt my research was never limited by anything other than what we could dream up. It has been one of the most creatively fulfilling experiences I've had to date, and for this I will always be grateful. Likewise, I would like to thank the members of my committee, Professors Justin Balko, Paul Laibinis, Jeffrey Rathmell, and Scott Guelcher, who provided a diverse array of advice and expertise without which much of this research would have been impossible.

To my parents, Ling-fang and Zon-yin, to whom I owe everything: I will never fully be able to express the depths of my gratitude for the endless sacrifices you made in parenthood to fill my life with opportunity. Your story of immigration to America is still one of the most inspiring I have ever heard, and being a part of this loving family has shaped me into the person I am today. Thank you for providing anything and everything that a son could reasonably ask for, and know that this accomplishment is as much yours as it is mine. To my brother Alvin, who foreran life 5 years ahead of me: life has always felt a little safer and more approachable following your lead, and I can say that watching someone with similar life experiences make it in life has instilled me with the confidence that sustains me every day. Thanks for being a friend and a role model.

To my partner-in-crime Tara, whose unwavering love has given me the perseverance to see this work through, and who always had my back, especially when I was at my lowest: you make everything in my life better. Thanks for giving me the strength every day to get out of bed

in the morning. To your parents Mary Jo and Karel: thanks for treating me like family and making Nashville feel like a home away from home.

To the young scientists I've been lucky enough to mentor: Anna Caldwell, Chuong Nguyen, Harrison Paul, and Kasey Coleman. It was a privilege to be a small part of early research careers. Each of you demonstrated an ambition and thoughtfulness that was beyond me at a similar age, and I know you all have great things ahead of you. Many thanks as well to my past and present lab mates who number too many to list, but are nonetheless deeply appreciated.

Finally, I acknowledge and thank the many resources that made this research possible. This work was funded by grants from Alex's Lemonade Stand (SID924), the National Science Foundation (1554623), the National Institutes of Health (CA204726/CA/NCI, R00CA181491, 5R35GM119569-03), the Vanderbilt-Ingram Cancer Center (Support Grant P30 CA68485, Ambassador Discovery Grant, Vanderbilt Center for Immunobiology Pilot Grant), the Melanoma Research Alliance (503565), and Stand up to Cancer (SU2C-AACR-IRG 20-17). Research was facilitated by the Vanderbilt Institute of Nanoscale Science and Engineering, Vanderbilt University Medical Center Flow Cytometry Shared Resource, Vanderbilt Digestive Disease Research Center, Vanderbilt Translational Pathology Shared Resource, Vanderbilt Technologies for Advanced Genomics, and Koch Institute Swanson Biotechnology Center core facilities, as well as resources from the lab of Craig Duvall.

Table of Contents

	Page
ACKNOWLEDGMENTS	ii
LIST OF FIGURES	vii
LIST OF ABBREVIATIONS.....	xi
CHAPTER	
1 Introduction and Background	1
1.1 Cancer Immunity and the State of Patient Care	1
1.2 The Immunosuppressive Tumor Microenvironment Inhibits Tumoricidal Immunity	3
1.3 Innate Immunity and Priming of Adaptive Immunity	7
1.4 Exploiting the cGAS/STING Pathway in Cancer Immunotherapy	11
1.5 Developing Nanoparticle Delivery Platforms to Improve CDN Delivery	14
1.6 Aims and Scope	17
2 Design and Optimization of STING-NPs	19
2.1 Introduction	19
2.2 Design, Synthesis, and Optimization of STING-NPs.....	22
2.3 <i>In Situ</i> Crosslinking is Critical to Achieving Endosomolytic Potency and Vesicular Morphology in STING-NPs.....	27
2.4 Evaluation of the Direct Hydration Method for cGAMP Encapsulation	37
2.5 <i>In Vitro</i> Validation of STING-NP Activity	41
2.6 Conclusion	45
2.7 Materials and Methods	46
3 Evaluation of STING-NPs in Murine Tumor Models	53
3.1 Introduction	53

3.2	STING-NP Treatment Induces Pro-Inflammatory Gene Expression in the TME.....	54
3.3	Nanoparticle Formulation Increases Cellular Uptake of CDNs	58
3.4	STING-NPs Traffic to the Tumor Draining Lymph Node, Facilitating Priming of T Cells	62
3.5	Intratumoral Administration of STING-NP is Not Associated With Onset of Long-Term Toxicological Side Effects.....	63
3.6	STING-NPs Treatment Drives an Influx of Activated T-cells and Myeloid Cells Into the TME	66
3.7	<i>In Situ</i> Vaccination with STING-NPs Generates Sustained and Systemic Immune Rejection of Cancer Cells.....	72
3.8	STING-NPs are Effective Antitumor Immunotherapeutics when Administered Intravenously	76
3.9	Evaluation of Biodistribution Following Systemic STING-NP Administration and qPCR.....	81
3.10	Cellular Uptake of STING-NPs in the Tumor and Lymphoid Organs.....	85
3.11	STING-NPs Stimulate Pro-Inflammatory Signaling in Resected Human Melanoma	89
3.12	Methods	90
4	Conclusions and Outlook.....	99
4.1	STING-NPs Improve the Delivery of cGAMP to STING, Activating Myeloid and T Cells to Tumoricidal Effect	99
4.2	Suggestions for Future Work.....	100
	REFERENCES	114
	APPENDIX.....	122
A.1	Nanoparticle Size Distribution Used for Theoretical Encapsulation Efficiency Calculations.....	122
A.2	Synthetic Scheme for PDSMA	123
A.3	Synthetic Scheme for PEG-DB and PEG-DBP Block Copolymers	124
A.4	¹ H NMR and GPC Characterization of pH-responsive Diblock Polymers	125

A.5 Synthetic Scheme for PEG-CTA synthesis.....	126
A.6 Synthetic Scheme for 2'3'-cGAMP.....	127
A.7 ¹ H-NMR Spectrum of Synthesized 2'3'-cGAMP.....	128
A.8 LCMS Characterization of 2'3'-cGAMP.....	129
A.9 Comparison of Biological Activity of Synthesized and Commercially Available 2'3'-cGAMP.....	130
B.1 Nanostring analysis of upregulated genes following IT STING-NP or cGAMP treatment.....	131
B.2 Synthetic scheme for fluorescent polymer labeling.....	132
B.3 Gating scheme for flow cytometric analysis of immune cell populations in the TME.....	133

List of Figures

	Page
1.1 Immunosuppressive mechanisms in the TME abrogate tumoricidal CD8+ T cell functions. Schematic of some critical mechanisms and cell types that mitigate T cell function in the tumor microenvironment	6
1.2 Stimulating innate immunity induces T cell priming and tumor destruction in a positive feedback loop. Schematic of the self-reinforcing processes of the cancer immunity cycle that can be jump-started <i>via</i> stimulation of innate immunity	10
1.3 The cGAS/STING immune surveillance pathway. Schematic of DAMP detection and pro-inflammatory signaling by the cGAS/STING immune sensors, the primary target of immunotherapy explored in this work	12
2.1 pH responsive polymers mediate endosomal escape through the proton sponge effect. Schematic of the use of pH responsive, buffering polymers for inducing disruption of the endosomal membrane	20
2.2 STING-NPs are potent activators of the STING immune sensing pathway. Schematic of the cause of differential activity of free cGAMP and STING-NPs. STING-NPs improve cGAMP by facilitating cellular uptake and disruption of the endosomal membrane transport barrier	22
2.3 Formulation of STING-NPs. Description of the functional activity of chemical moieties comprising STING-NP polymers and schematic of formulation process	24
2.4 Characterization of STING-NPs. DLS, zeta potential, and electron microscopy particle characterization techniques. Data indicate that particles are monodisperse, of appropriate size for lymphatic drainage, PEG shielded, and of a vesicular structure, with a stimulus responsive ‘smart’ functionality that is expected to cause particle disassembly and drug release in the endosome of endocytic cells.....	26
2.5 Confirmation of STING-NP crosslinking. GPC and UV-vis spectroscopy confirm that DTT treatment causes crosslinking of chains comprising STING-NPs. Data are suggestive that the reduction reaction occurs stoichiometrically.....	28
2.6 Hemolysis of PEG_{2k}-DBP_{4.5k} and PEG_{2k}-DB_y formulations. The ability of polymers to cause hemoglobin leakage in red blood cells at various pH is used to predict the ability of polymers to mediate endosomal membrane disruption and subsequent endosomal escape. Data indicate that high molecular weight of the hydrophobic block is a requisite parameter of potent hemolytic activity, which is achieved through optimal crosslinking of PEG _{2k} -DBP _{4.5k} polymers. Hemolytic nanoparticles are not active at physiological due to PEG shielding, which is expected to make the particles well suited for IV administration	29

2.7	Self-assembled morphologies of PEG_x-DB_y BCPs. Electron micrographs show that low molecular weight PEG _{2k} -DB _{5k} polymers self-assemble into vesicular structures, while larger PEG _{5k} -DB _y and PEG _{10k} -DB _y with comparable W _{PEG} are biased towards micellar self-assembly. These data highlight a tension between vesicular self-assembled architectures and potent endosomolytic activity characteristic of high molecular weight polymers	31
2.8	The effect on self-assembled morphology on the stretching of the polymer corona block. Schematic of polymer corona stretching in bilayer, cylindrical micelle, and spherical micelle morphologies. Surface curvature favors micellar morphologies as the molecular weight of the hydrophilic block increases.....	33
2.9	The effect of particle diameter on interfacial surface tension. Schematic of interfacial surface area and particle diameter. At a fixed W _{PEG} , increasing molecular weight of the hydrophobic block makes micellar morphologies less unfavorable relative to bilayer morphologies.....	36
2.10	Schematic of the BCC unit cell. Unit cell is used for theoretical calculation of the encapsulation efficiency of direct hydration	39
2.11	STING-NPs dramatically enhance cGAMP potency by enhancing cytosolic delivery efficiency. Dose response curves in IRF3 reporter cell lines and fluorescent quantification of CDN uptake demonstrate that STING-NPs are 2-3 orders of magnitude more potent than free cGAMP. Dose response curves with control formulations and flow cytometric quantification of CDN uptake demonstrate that STING-NPs enhance cGAMP potency by facilitating cellular uptake and by improving drug endosomal escape.....	42
2.12	STING-NPs induce IFN-I production and expression of antigen presentation/co-stimulatory proteins in DCs. STING-NPs are effective in both primary and immortalized DCs, inducing a pro-inflammatory phenotype that is expected to be conducive to activation of T cells.	44
2.13	STING-NPs reprogram M2 polarized bone marrow derived macrophages to a pro-inflammatory M1 phenotype. qPCR analysis of changes in gene expression in BMDMs following STING-NP treatment.....	45
3.1	IT STING-NP induces a pro-inflammatory and T cell recruiting gene expression profile. Consistent with <i>in vitro</i> data, STING-NPs demonstrate enhancements in cGAMP potency <i>in vivo</i> when injected intratumorally into B16.F10 tumors. Among upregulated genes in the TME are critical T cell chemokines <i>Cxcl9</i> and <i>Cxcl10</i>	55
3.2	STING-NP treatment generates sustained expression of IFN in the TME. Longitudinal analysis of IFN expression in the TME through use of subcutaneous B16.F10 tumors transfected with an ISRE-luc reporter construct	56
3.3	NanoString multiplexed gene analysis of B16.F10 melanoma tumors. High throughput mRNA quantification demonstrates a broad array of tumoricidal genes are	

upregulated following STING-NP treatment	58
3.4 Macrophages and DCs are the primary initiators of the immune response following STING-NP treatment. Flow cytometric quantification of cellular uptake of STING-NPs and qPCR analysis of cell subsets treated with STING-NPs. Data indicate that DCs and macrophages are likely the primary initiators of the IFN-I response	60
3.5 STING-NPs drain to the TDLN and induce a gene expression profile supportive to T cell priming. STING-NPs accumulate far more efficiently than free CDN to the TDLN, increasing IFN-I expression and surface expression of co-stimulatory CD86 by DCs	64
3.6 Evaluation of IT administered STING-NP and cGAMP toxicity. The STING-NP IT therapeutic regimen was not observed to cause persistent liver or kidney related pathologies	67
3.7 STING-NP treatment alters the myeloid cell profile in the TME. Flow cytometric quantification of cells in the TME. Neutrophils and MDSCs are recruited following IT STING-NP administration. Macrophage density is not affected, but surface of expression of CD206 on macrophages is decreased in tumors treated with STING-NPs, indicative of repolarization away from an immunosuppressive phenotype	69
3.8 STING-NP treatment recruits cytotoxic T cells to the TME. Flow cytometric analysis of the TME reveals an influx of CD8+ and CD4+ T cells following STING-NP treatment	70
3.9 T cells recruited to the TME are not regulatory T cells. Flow cytometric analysis of T cells in the TME reveals no FoxP3 expression, a regulatory T cell marker	71
3.10 T cells in STING-NP treated tumors are of an activated, tumoricidal phenotype. Flow cytometric analysis; T cells isolated from STING-NP treated tumors are more primed to produce tumoricidal cytokine than analogous cells from control tumors	71
3.11 Increased secretion of cytotoxic cytokines by T cells is not accompanied by secretion of immunosuppressive cytokines. Flow cytometric analysis; increased production of tumoricidal cytokines by T cells is not accompanied by secretion of immunosuppressive cytokines	72
3.12 STING-NPs enhance the immunotherapeutic efficacy of cGAMP and generate long-lived, systemic immunity. STING-NP monotherapy suppresses tumor growth and can induce complete tumor rejection. Complete responders are resistant to tumor rechallenge as far as 65 days after inoculation	75
3.13 <i>In situ</i> vaccination with STING-NPs suppresses established distal tumors and synergizes with immune checkpoint blockade. STING-NP monotherapy suppresses both primary and distal tumors in a contralateral tumor model. Contralateral tumor suppression is significantly enhanced if treatment is combined with ICB	76

3.14	Intravenous STING-NP administration suppresses tumor growth and increases the effectiveness of ICB. Systemic administration of STING-NPs suppresses tumor growth but does not induce complete tumor rejection unless combined with ICB. Complete responders show resistance to tumor rechallenge, but 0/4 mice completely resisted secondary inoculation	77
3.15	Toxicological analysis of IV administered STING-NP and cGAMP. Blood chemistry and histological analyses did not reveal evidence of long-term liver or kidney related pathology associated with IV administration of STING-NPs in isolation or in combination with ICB.....	79
3.16	Randomly selected H&E stained liver sections. Images were part of cohorts used to generate scores of vacuolation severity presented in figure 3.15.....	80
3.17	STING-NPs largely accumulate in the liver with lesser but significant accumulation in the lymphoid organs. IVIS quantification of organ accumulation of IV administered STING-NPs labeled with a fluorescent tag. The majority of STING-NPs are found in the liver, with a lesser degree of accumulation in the liver, spleen and kidney	83
3.18	Longitudinal analysis of proinflammatory gene expression in the tumor and lymphoid organs. qPCR analysis of the tumor, liver, and TDLN over 24h. STING-NPs induce higher magnitudes <i>Ifnb1</i> and <i>Cxcl10</i> than free cGAMP.....	84
3.19	Flow cytometric analysis of cellular uptake profiles of IV administered STING-NPs. Differing cell uptake profiles are found in the spleen, TDLN, and tumor, which is suggestive of different transport mechanisms responsible for STING-NP accumulation in the tumor and lymphoid organs.....	86
3.20	STING-NPs enhance cGAMP activity in human metastatic melanoma. An <i>ex vivo</i> IT model of treatment using resected human metastatic melanoma indicates that STING-NP demonstrate similar activity in human tissue	91
4.1	Potential targets for synergistic combination therapy with STING-NPs. Analysis of selected genes that were identified by nanoString to be significantly upregulated and potential targets for combination therapy	105

List of Abbreviations

ACN – Acetonitrile

APC – Antigen presenting cell

Arg - Arginase

BCP – Block copolymer

BHT – Butylated hydroxytoluene

BMA – Butyl methacrylate

BMDC – Bone marrow derived dendritic cell

BMDM – Bone marrow derived macrophage

CD – Cluster of differentiation

CDN – Cyclic dinucleotide

CRT – Calreticulin

CTA – Chain transfer agent

CTL – Cytotoxic T lymphocyte

CTLA-4 – Cytotoxic T lymphocyte associated protein 4

CPADB – 4-Cyano-4-(phenylcarbonothioylthio)pentanoic acid

DAMP – Damage associated molecular pattern

DBP – 2-(diethylanimo)ethyl methacrylate-*co*-butyl methacrylate-*co*-pyridyl disulfide ethyl methacrylate

DC – Dendritic cell

DCC – N,N'-Dicyclohexylcarbodiimide

DCM – Dichloromethane

DNA – Deoxyribonucleic acid

dsDNA – Double stranded deoxyribonucleic acid

DEAEMA – 2-(Diethylamino)ethyl methacrylate

DMAP – 4-Dimethylaminopyridine

DMXAA – 5,6-Dimethylxanthenone-4-acetic acid

DT – Doubling time

DTT – Dithiothreitol

Dy547 – Dylight554

HMGB1 – High mobility group box 1 protein

ICB – Immune checkpoint blockade

ICD – Immunogenic cell death

IFNAR – Interferon alpha/beta receptor

IRF – Interferon regulatory factor

ISRE – Interferon stimulated response element

FoxP3 – Forkhead box P3

GITR – Glucocorticoid-induced TNFR-related protein

GPC – Gel permeation chromatography

ICOS – Inducible T cell costimulator

IDO – Indoleamine 2,3-dioxygenase

IFN - Interferon

IL – Interleukin

IT – Intratumoral/Intratumorally

IV – Intravenous/Intravenously

LAG-3 – Lymphocyte activation gene 3

LN – Lymph node

MDSC – Myeloid derived stem cell

MFI – Median fluorescent intensity

MHC – Major histocompatibility complex

NK – Natural Killer

mCTA – Macro chain transfer agent

mRNA – Messenger ribonucleic acid

MS – median survival

PAMP – Pathogen associated molecular pattern

PD-1 – Programmed cell death protein 1

PD-L1 – Programmed death ligand 1

PDI – Polydispersity index

PDS – Pyridyl disulfide

PDSMA – Pyridyl disulfide ethyl methacrylate

PEG – Poly(ethylene glycol)

PEG-DB – Poly[(ethylene glycol)-*block*-[(2-(diethylamino)ethyl methacrylate)-*co*-(butyl methacrylate)]]

PEG-DBP – Poly[(ethylene glycol)-*block*-[(2-(diethylamino)ethyl methacrylate)-*co*-(butyl methacrylate)-*co*-(pyridyl disulfide ethyl methacrylate)]]

PEI – Poly(ethylenimine)

PMA – Phorbol 12-myristate 13-acetate

RAFT – Reversible addition fragmentation transfer

RBC – Red blood cell

RES – Reticuloendothelial system

ROS – Reactive oxygen species

STING – Stimulator of interferon genes

TAA – Tumor associated antigen

TAM – Tumor associated macrophage

TCR - T cell receptor

TDLN – Tumor draining lymph node

TEM – Transmission electron microscopy

TGF- β – Transforming growth factor beta

TIL – Tumor infiltrating lymphocyte

TIM-3 – T cell immunoglobulin and mucin domain containing 3

TME – Tumor microenvironment

TNF- α – Tumor necrosis factor alpha

UV - Ultraviolet

UV-vis – Ultraviolet-visible light

V501 – 4,4'-Azobis(4-cyanovaleric acid)

V70 – 2,2'-Azobis(4-methoxy-2,4-dimethylvaleronitrile)

VISTA – V domain Ig suppressor of T cell activation

W_{PEG} – Hydrophilic weight fraction

Chapter 1: Introduction and Background

1.1 Cancer Immunity and the State of Patient Care.

Cancer arises when genetic mutations result in runaway cell growth. As cancer cells replicate aggressively, they invade surrounding tissue and may metastasize to distant parts of the body, ultimately causing organ failure and mortality in patients. Until recently, clinical treatment has relied heavily on a combination of physical excision of malignant tissue, localized radiotherapy, and systemically administered chemotherapeutics. Unfortunately, these techniques eliminate target cancerous growths at the cost of causing significant damage to healthy tissue, and complete eradication of cancer cells with tolerable treatment regimens is often impossible, especially in late stage diseases in which cancer cells have begun to metastasize. Many treated patients will therefore go on to experience recurrent disease as escaping cancer cells continue to replicate.

The problems of metastasis and recurrence have caused investigators to turn to the immune system for antitumor therapy. In principle, the immune system can differentiate between cancerous and healthy tissue, providing an avenue for systemic elimination of cancerous cells that is less subject to toxicity limited efficacy. This potential has inspired investigation into the use of immunotherapy for cancer treatment, which has roots in observations made in the 19th century describing a relationship between tumor remission and the onset of bacterial skin infection.^{1,2} These observations inspired the first widespread immunotherapeutic cancer treatment; so-called ‘Coley’s Toxins’ consisting of heat-inactivated bacteria were reported to generate tumor remission after administration³, although the mechanism of action remained elusive at the time.

More than 100 years later, tireless investigation by innumerable researchers has elucidated several critical aspects of cancer immunity. Immune phenotyping has revealed that across a wide variety of tumor types, tumor infiltrating cluster of differentiation 8 positive (CD8+) T cells serve as a positive prognostic indicator for cancer patients, correlating with a lower rate of recurrence and post-operative long-term survival.⁴ Part of the adaptive branch of immunity, T cells surveil the body for cells expressing aberrant proteins, identifying them for destruction through antigen specific T cell receptor-major histocompatibility complex-I (TCR-MHC-I) interactions. In the context of cancer immunity, the very genomic instabilities that result in tumorigenesis are often accompanied by mutations in the cancer genome that lead to expression of neoantigens: proteins that differ from those secreted by healthy cells which can mark cancerous cells for T cell mediated destruction when processed and presented on MHC-I.⁵ In this way, a properly activated immune system can systemically and selectively suppress metastatic growths and remaining cancer cells that survive standard-of-care treatments, dramatically improving patient outcomes.

A critical question thus arises: if cognate CD8+ T cells are capable of destroying malignant cells, why do immunocompetent patients so often succumb to cancer? Part of the answer lies in the immune suppressed tumor microenvironment (TME). Tumors are often characterized by high levels of infiltrating immunosuppressive cell subsets such as tumor associated macrophages⁶ (TAMs), myeloid derived suppressor cells⁷ (MDSCs), and regulatory T-cells⁸ (Tregs), all of which inhibit effective antitumor T cell immunity through expression of proteins that interfere with effector T cell function. Much of recent progress in cancer immunotherapy has focused on blocking these immunosuppressive pathways to restore tumoricidal T cell function in the TME. These efforts have led to the development of immune checkpoint blockade (ICB), a watershed event that revolutionized the standard of care in cancer treatment by demonstrating cases of

complete tumor remission in advanced and inoperable metastatic disease following antibody mediated blockade of the T cell inhibitory programmed cell death-1 (PD-1) and cytotoxic lymphocyte-associated protein-4 (CTLA-4) pathways^{9,10}.

Despite this exciting development, complete tumor regression following checkpoint blockade therapy remains the exception rather than the rule, with clinical trials typically reporting complete tumor remission in <10% of cases⁹⁻¹³. A significant fraction of treated patients fail to demonstrate any objective response at all. Phenotypic investigation of patients has revealed that broadly speaking, responsiveness to checkpoint blockade tends to correlate with a tumor characterized by high levels of infiltrating CD8+ T cells.¹⁴ In cases of PD-1 checkpoint blockade for metastatic melanoma for instance, it has been reported that roughly 38% of patients fall into a tumor infiltrating lymphocyte (TIL) and PD-1 high TME classification, which are thought to represent the vast majority of patients that benefit from checkpoint blockade. Roughly 20% of patients were found to exhibit a TIL high and PD-1 low phenotype, indicative of a phenotype in which T cell immunity was likely inhibited by another immunosuppressive pathway. The remaining 42% of patients are thought to demonstrate little sensitivity to checkpoint blockade and exhibit low TIL counts, indicating a phenotype in which the immune system has failed to mount an antigen specific T cell response of any appreciable magnitude. In a conceptually simple framework, these patients can be grouped into a spectrum of immunologically ‘cold’ and ‘hot’ phenotypes, in which the latter describes a T cell inflamed tumor in which tumor eradication is inhibited by various immunosuppressive mechanisms in the TME, while the former represents a case in which the host has failed to mobilize adaptive antitumor immunity. Quite reasonably, checkpoint blockade tends to be more effective in hot tumors, which contain a preexisting T cell response that can be targeted for reinvigoration. Thus, two grand challenges in moving cancer

immunotherapy forward arise. First, it is necessary to continue to develop strategies that abrogate a broader set of immunosuppressive mechanisms in the TME to fully unleash the potential of antitumor T cells. Second, treatments will need to prime *de novo* T cell responses in the significant fraction of patients who fail to achieve endogenous antitumor T cell mobilization. This work explores the use of immunostimulatory stimulator of interferon genes (STING) activating agonists as a solution to both of these grand challenges.

1.2 The Immunosuppressive Tumor Microenvironment Inhibits Tumoricidal Immunity.

While antibodies blocking the PD-1 and CTLA-4 checkpoint pathways have demonstrated striking clinical success, by no means do they exhaustively abrogate the many mechanisms of immunosuppression in the TME. Improving patient outcomes therefore relies critically on more broadly stymieing T cell inhibitory pathways in the TME. The list of checkpoint blockade antibodies being investigated continues to grow rapidly, including those targeting the LAG-3, TIM-3, VISTA, OX40, 4-1BB, B7-H3, GITR, and ICOS pathways¹⁵. As these checkpoint blockade continue to move through clinical trials, we may expect to see cancer immunotherapy continue to deliver increasingly impressive outcomes in the clinic.

Nevertheless, several immunosuppressive mechanisms in the TME are not amenable to antibody mediated ICB. TAMs for instance express immunosuppressive cytokines such as IL-10, and TGF- β , which can inhibit conventional T cell cytotoxicity¹⁶ or contribute to proliferation of regulatory Tregs¹⁷. MDSCs and TAMs, in addition to expressing checkpoint molecules such as PD-L1, B7-H4 and VISTA, both express intracellular proteins such as arginases¹⁸ (Arg) and indoleamine deoxygenase¹⁹ (IDO) which act to deplete the TME of the critical T cell nutrients arginine and tryptophan, respectively. Depletion of these amino acids leads to inhibition of CD3 ζ

signal transduction in T cells, severely abrogating their cytotoxicity and ability to proliferate in the TME. Additionally, IDO catabolizes tryptophan to a family of compounds known as kynurenines which actively promotes differentiation of CD4⁺ T cells into Tregs²⁰. Tregs then abrogate effector T cell function by scavenging IL-2, a critical cytokine in effector T-cell survival from the TME, secretion of immunosuppressive cytokines, and expression of CTLA-4⁸. These immunosuppressive mechanisms are pernicious in the process of tumor progression, and high levels of TAM, MDSC, and Treg infiltration in the tumor milieu have each been correlated with poor patient outcomes (**Figure 1.1**).

Given the wide swath of immunosuppressive proteins that are produced by these cell types, combinatorial inhibition of each of these immunosuppressive pathways in the TME, through administration of targeted small molecule inhibitors and antibodies, while not impossible, is a daunting task. This challenge is made especially difficult due to the possibility of immune related adverse events following administration of checkpoint blockade antibodies²¹. While further development of checkpoint blockade antibodies will no doubt continue to play a critical role in the cancer immunotherapeutic toolbox, it alone may be insufficient comprehensively abrogate T cell inhibitory pathways in the TME.

Interestingly, TAMs and MDSCs have been reported to demonstrate phenotypic plasticity, switching between immunoregulatory and proinflammatory phenotypes depending the immune context. TAMs for instance may be repolarized to an ‘M1’ phenotype when exposed to proinflammatory signals, resulting in high production of tumoricidal reactive oxygen species (ROS) and tumor necrosis factor alpha (TNF- α) with a simultaneous decrease in Arg-1 expression.²² MDSCs consist of a heterogeneous population of immature dendritic cells (DCs), macrophages, and granulocytes and can be readily differentiated into functional antitumor myeloid

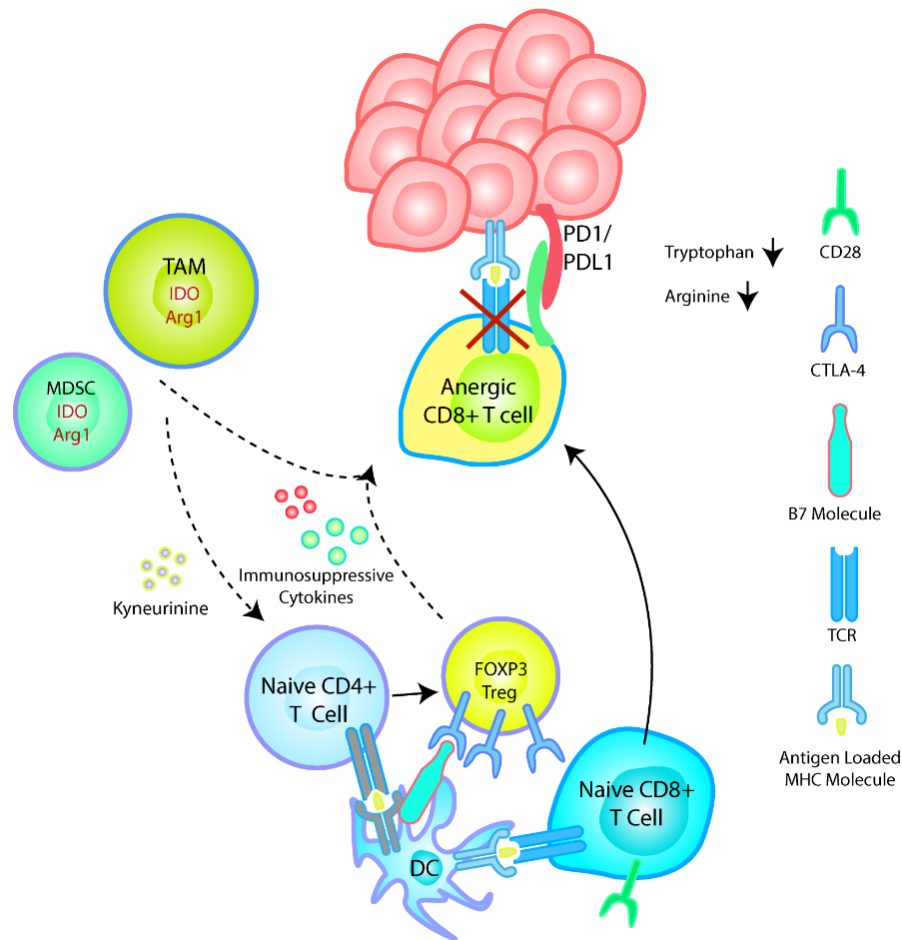


Figure 1.1. Immunosuppressive mechanisms in the TME abrogate tumoricidal CD8+ T cell functions. IDO expression by TAMs and MDSCs generates kynurenine, biasing CD4+ T cell differentiation into a FoxP3 regulatory phenotype. Tregs overexpress CTLA-4 to compete away B7/CD28 co-stimulation of naïve CD8+ T cells. T cells differentiate into anergic phenotype. Expression of immunosuppressive cytokines such as IL-10 and TGF- β suppress CD8+ tumoricidal function, along with PD-1/PD-L1 signaling. Expression of IDO and Arg1 depletes tryptophan and arginine in the TME, leading to loss of CD3 ζ expression and loss of TCR dependent signal transduction.

cells upon pro-inflammatory stimulation.²³ Depletion of these immunosuppressive cell subsets may then lead to decreased IDO expression in the TME, resulting in a lower magnitude of CD4+ T cell differentiation into Tregs. These phenomena demonstrate that pro-inflammatory treatment of tumors can result in a broad a robust reprogramming of the TME, inducing a tumoricidal phenotype in tumor resident myeloid cells while mitigating a broad range of T cell immunosuppressive mechanisms that are associated with TAMs and MDSCs that may not be

amenable to ICB. As such, we expect that stimulation of pro-inflammatory pathways within the TME is a strategy that is well-positioned to build on the gains of ICB.

1.3 Innate Immunity and Priming of Adaptive Immunity.

Innate immunity in general refers to rapid responses mediated by myeloid cells upon detection of pathogen associated molecular patterns (PAMPs) and danger associated molecular patterns (DAMPs), widely produced danger signals that are the hallmarks of pathogens.²⁴ By contrast, T cells, classified as adaptive immunity, surveil the body on the basis of protein expression and antigen specificity. Through somatic recombination, T cells combinatorically cut and splice segments of their DNA responsible for TCR production, allowing for expression of a diverse set of TCRs capable of recognizing an extremely broad set of protein derived antigens despite originating from a relatively limited genome.²⁵ Activated T cells then surveil the body for production of aberrant proteins in infected or malignant cells, which are routinely cut into smaller amino acid peptides for presentation on MHC-I for T cell examination. This process that ultimately triggers a pro-inflammatory signaling cascade or cellular destruction upon recognition of a MHC-I bound peptide by a cognate TCR.

Developing an antitumor T cell response is reliant on the process of antigen presentation. In a dormant state, naïve T cells reside in lymphoid organs such as the LN and spleen and lack tumoricidal function. Mobilization is most critically mediated by the DC, a specialized antigen presenting cell (APC) that readily consumes TAAs for antigen presentation and traffics to the LN upon encountering PAMPs or other pro-inflammatory signals.^{26,27} Upon TCR recognition of tumor antigen presenting DCs, which critically also provide co-stimulatory support through the CD28 signaling pathway,²⁸ T cells proliferate and migrate into the vasculature to begin antigen specific

immune surveillance. As previously discussed however, a large portion of patients typically fail to develop a large magnitude of tumor infiltrating lymphocytes even in melanoma,¹⁴ a cancer type with a notoriously high mutational load for neoantigen expression.²⁹ This breakdown in antigen presentation and T cell priming one of the critical factors holding back progress in cancer immunotherapy.

This phenomenon can be partially attributed to DC dysfunction in the immunosuppressive TME. High levels of immunosuppressive cytokines such as IL-10 found in the TME suppress maturation of DCs, lowering their expression of MHC and co-stimulatory molecules, inhibiting their T cell priming ability.³⁰⁻³¹ The tumor immunosuppressive program disrupts the steady state balance of DC production and maturation systemically, and fewer numbers of both DCs in the periphery and in the LNs are typically found in tumor bearing patients when compared to healthy cohorts.³² As expected, this decrease in immunosupportive DCs is typically accompanied by an increase in immature and monocytic DC precursors throughout the host that then perpetuate an immunosuppressive feedback loop by expressing molecules such as IL-10, IDO, Arg-1 and various checkpoint molecules.³³ In addition to suppressing T cell function in the TME, this effect is especially pernicious in the LN, in which immunosuppressive DCs and DC precursors fail to generate effector cytotoxic T lymphocytes (CTLs) while actively promoting the expansion of Tregs.³⁴

Another potential cause of failed antitumor T cell mobilization is simply lack of availability of antigen for presentation. CD8+ T-cell mobilization is reliant on presentation of antigens by MHC-I on DCs. In contrast to cells relying on classical MHC-I peptide presentation, a cytosolic process in which intracellularly produced proteins are systematically cleaved and loaded on MHC-I,³⁵ Certain DC subsets are associated with of cross-presentation: a set of mechanisms through

which DCs are capable class I presentation of antigens encountered exogeneously.^{36,37} In a properly stimulated TME, pro-inflammatory leukocytes produce tumoricidal factors such as ROS, TNFs, and interferons (IFNs) that mediate constant apoptosis and necrosis in the TME. This process facilitates TAA cross presentation by consistently releasing large amounts of tumor antigen for DC uptake³⁸ and by causing expression of damage associated molecular patterns (DAMPs) such as calreticulin (CRT) and high mobility box protein 1 (HMGB1) which can mark cancer cells for phagocytosis by DCs. However, a significant portion of patients fail to achieve this tumoricidal phenotype, leaving a large quantity of tumor antigen locked within viable tumor cells.

Thus, in addition to suppressing tumoricidal T cell function, the immunosuppressive TME inhibits T cell immunity by interfering with DC mediated TAA uptake and presentation. This provides further motivation for developing strategies to reprogram myeloid cells in the TME to a proinflammatory phenotype. Effects of these strategies are multifaceted and are neatly described in a concept known as the cancer immunity cycle (**Figure 1.2**). First, inducing secretion of pro-inflammatory and tumoricidal factors such as ROS, TNFs and IFNs result in tumor cell death and TAA liberation. Second, DCs encounter and present TAAs. Stimulated by pro-inflammatory cytokines and DAMPs, DCs mature and migrate to the LN and serve as effective primers of naïve T-cells with cognate TCR. Third, activated T cells proliferate, migrate to the tumor, and play critical roles in selective destruction of cancerous cells, a process that serves to liberate more antigen for DC uptake in a positive feedback loop. Thus, interventions targeted at innate immunity have a unique and critical role that is not well addressed by currently available technologies.

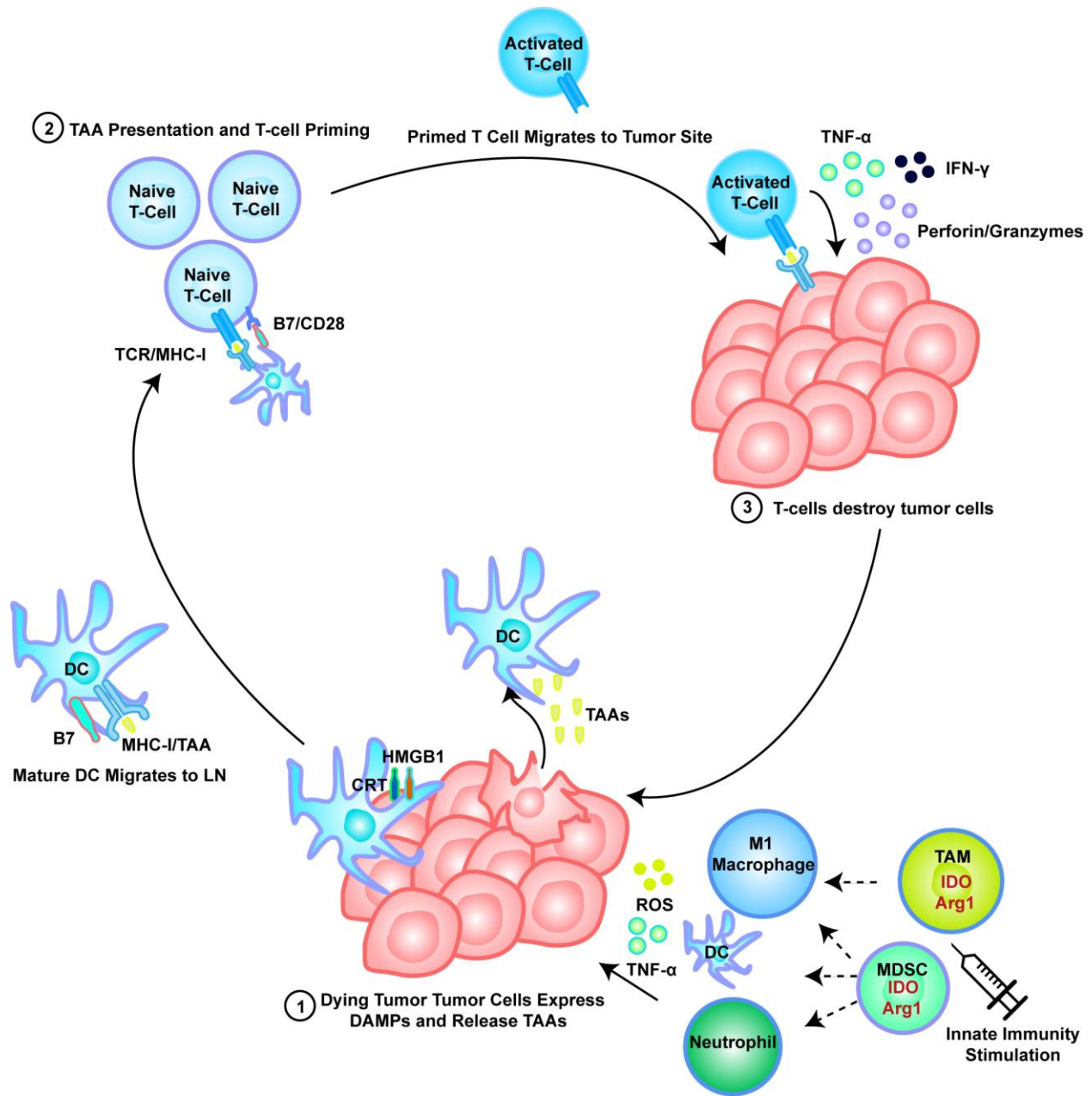


Figure 1.2. Stimulating innate immunity induces T cell priming and tumor destruction in a positive feedback loop. Administration of PRR agonists in the TME reprograms myeloid cells to pro-inflammatory phenotypes. Activated cells produce pro-inflammatory/pro-apoptotic factors such as ROS and TNF α , causing (1) tumor cell death and upregulation of DAMPs (HMGB1, CRT) that opsonize tumor cells for uptake. Cells and TAAs are engulfed by DCs, which mature and migrate to the LN for antigen presentation. (2) DCs prime and activate T-cells, which migrate to tumor site. (3) Activated T-cells release TNF α , IFN- γ , and ROS upon recognition of MHC-I bound antigen, causing further cell death and DAMP expression.

1.4 Exploiting the cGAS/STING Pathway in Cancer Immunotherapy.

Discovered in 2013, the cyclic guanosine monophosphate adenosine monophosphate synthase (cGAS) protein surveils the cell interior for the presence of cytosolic double stranded DNA,³⁹ a hallmark of cancerous cells with damaged genomic DNA.⁴⁰ Activation of cGAS leads to production of 2'3'-cyclic adenosine monophosphate guanosine phosphate (cGAMP), an endogenous DAMP that serves as the agonist for the stimulator of interferon genes (STING) protein.⁴¹ This process ultimately triggers a signaling cascade through the interferon regulatory factor 3 (IRF3) and nuclear transcription factor kappa B (NF-κB) proteins, characterized by production of pro-inflammatory cytokines, most notably IFN-I (**Figure 1.3**). In the years since its discovery, the cGAS/STING pathway has rapidly emerged as one of the pattern recognition receptors that mediates cancer cell detection by innate immunity. Mice deficient in STING demonstrate blunted IFN-I response, antitumor T cell mobilization, and subsequently, increased susceptibility to tumor progression.⁴² Critically, these mice are more recalcitrant to ICB due to lack of spontaneous T cell priming. Interestingly, STING deficiency also appears to affect the efficacy of radiotherapy, which is expected to accelerate genomic stress in cancerous cells, increasing leakage of DNA into the cytosol for cGAS detection. While analogous mechanistic data are far less plentiful in human patients, similar trends of poor prognosis associated with decreased STING expression have been identified in the clinic, suggesting that similar phenomena are at play in human cancers.⁴³ Taken altogether, these data indicate that STING activation plays a critical role in the mobilization of endogenous antitumor immunity and can determine the efficacy of the most important therapies currently used in cancer treatment today. This set of data serves as the motivation for use of STING agonists over other activators of innate immunity for cancer immunotherapy that are explored in this work.

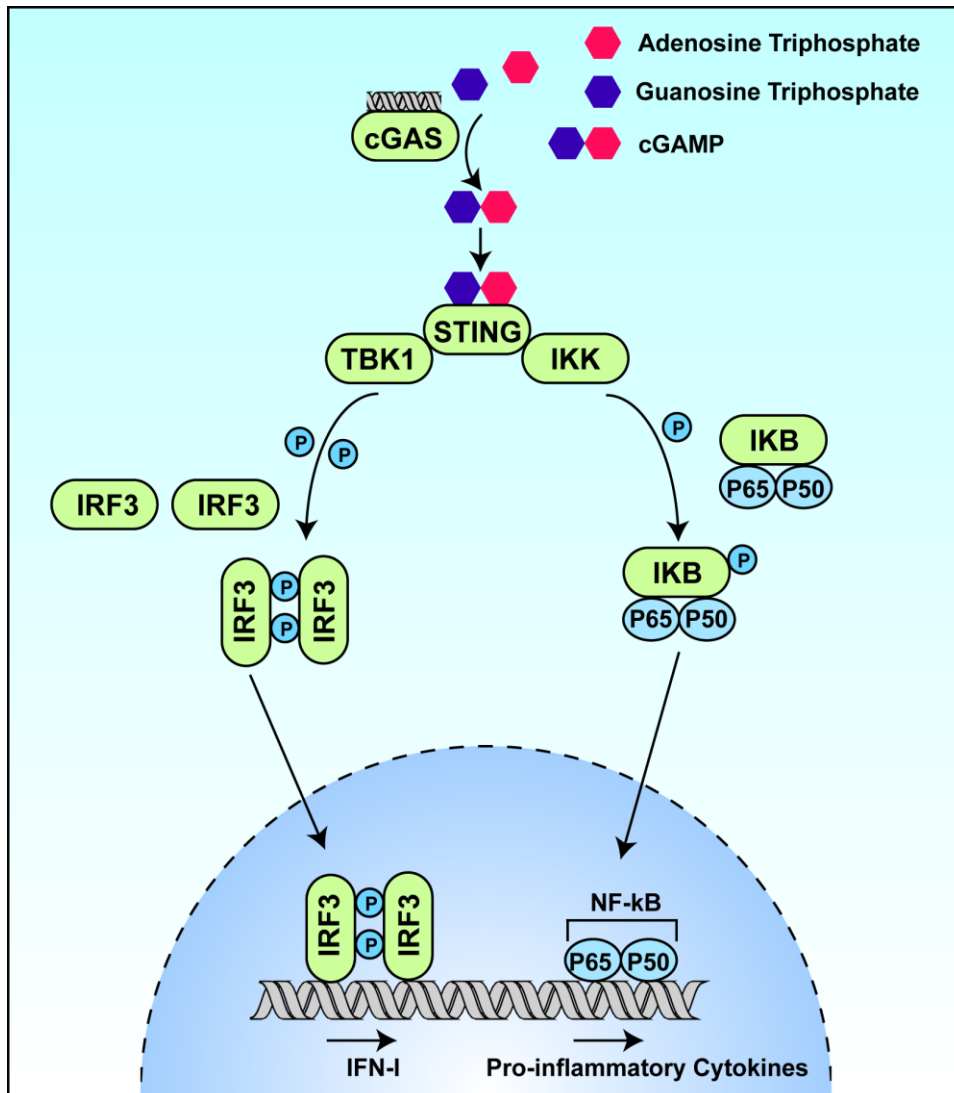


Figure 1.3. The cGAS/STING immune surveillance pathway. cGAS detects dsDNA and synthesizes cGAMP. cGAMP binds to STING, which phosphorylates IRF3 and the inhibitor of kappa B (IκB)-P65-P50 complex, respectively through tank binding kinase (TBK1) and inhibitor of kappa B kinase (IKK), respectively. Phospho-IRF3 dimerizes and translocates to the nucleus to stimulate IFN-I production. P65 and P50, comprising NF-κB dissociates from phospho-IκB and translocates to the nucleus to upregulate gene transcription.

Currently, the most well-developed use of STING based immunotherapy involves direct intratumoral (IT) injection of STING agonists which has demonstrated efficacy in a variety of murine tumors.⁴⁴⁻⁴⁸ Benefit is effected through a pleiotropic mechanism; STING activation has been reported to recruit tumoricidal natural killer (NK) cells to the TME,⁴⁹ reprogram TAMs to induce damage in the tumor vasculature in TNF- α dependent manner,⁴⁴ and generate an increased

number of antigen specific CD8+ T cells both in the circulation and in the tumor milieu.⁵⁰ The efficacy of the natural STING ligand cGAMP however has been limited due to drug delivery challenges. In the context of endogenous cancer detection, cGAMP is produced intracellularly for STING recognition by cGAS upon detection of dsDNA in the cytosol. By contrast, the vast majority of exogenously administered cGAMP is thought not to reach STING due to its physicochemical properties as a small, hydrophilic and negatively charged molecule that is not well suited for diffusion across the phospholipid bilayer membrane.⁵¹ This delivery challenge is further exacerbated by rapid leakage of cGAMP from the injection site into the bloodstream and subsequent clearance from the body.^{50,52} Additionally, cGAMP is vulnerable to enzymatic degradation, further reducing the amount of cGAMP that will ultimately be available for STING activation.

Several small molecule engineering innovations have ameliorated, but not eliminated, the delivery challenges associated with CDN administration. State-of-the-art synthetic CDNs typically include substitution of phosphorothioatediester linkages within the cGAMP molecule and related CDN analogues.⁴⁸ Modification renders the molecule resistant to enzymatic cleavage and marginally increases hydrophobicity. Thioated CDNs have therefore been reported to be roughly 5 to 10 times potent *in vitro* and demonstrate improved antitumor efficacy in murine tumor models, likely due to improved transcellular permeation and sustained intracellular cGAMP activity. These strategies represent critical progress in the field of STING dependent cancer immunotherapy, but nevertheless only mitigate the delivery challenges associated with CDN delivery. Pharmacokinetics properties remain relatively poor, with the half-life of synthetic CDNs reported to be roughly 15-30 minutes.⁵⁰ These challenges can be partially overcome through high dose IT administration of synthetic CDNs, which is capable of generating complete responses in murine

tumor models. Nevertheless, several challenges still remain in STING-based immunotherapy. Extremely high dose administration of modified CDNs can lead to systemic biodistribution and uncontrolled inflammation: a phenomenon that can be exacerbated due to the ability of synthetic CDNs to resist cleavage by endogenous phosphodiesterases. Rapid clearance of CDNs remains a problem, especially in the setting of intravenous (IV) administration for which even high doses of CDNs struggle to generate tumor rejection.⁵³ These pharmacokinetic challenges have likely contributed to mixed results in early clinical trials for STING ligands, wherein one trial performed by Merck reported 0/20 partial responses for STING monotherapy and 6/25 partial responses for combination therapy with PD-1 blockade in patients with solid tumors and lymphomas (NCT03010176). Another trial performed by Aduro Biotech demonstrated 2/40 partial response and 11/40 achievement of stable disease, along with broad increases in CD8+ cells in injected tumors, in patients who were treated with STING monotherapy. A combination therapy trial with PD-1 blockade is ongoing (NCT02675439). While these results indicate promise for the relatively young field of STING targeted cancer immunotherapy, it is clear that there is significant room for improvement.

1.5 Developing Nanoparticle Delivery Platforms to Improve CDN Delivery.

Nanoparticulate delivery platforms present several advantages over direct administration of small molecule therapeutics. While CDNs are typically reliant on diffusion to cross the cellular membrane, appropriately sized nanoparticles (NPs) can be endocytosed by target cells and therefore significantly improve intracellular CDN localization by exploiting an active transport mechanism. Furthermore, while small molecule CDNs easily leak into the vasculature following IT administration, nanoparticles can have more difficulty crossing the small pores of tumor blood

vessels and are thus more strongly retained at the site of injection. Thus, through a combination of size-determined faster uptake kinetics and increased retention times, nanoparticles can significantly improve the delivery efficiency of CDNs to intracellular compartments in the TME.

Yet another critical aspect of CDN delivery involves localization of drug in the LN. As stated above, the LN is the locus of T cell priming, and proper immune context is critical to priming of an adaptive immune response. In the context of cancer progression however, the lymphatic network often serves as a primary site of cancer metastasis.⁵⁴ As a result, the tumor draining lymph node (TDLN), the LN that serves as the nearest site of lymph drainage for established tumors, is often replete with tumor associated antigen and is a natural site for T cell priming. The TDLN microenvironment however, is characterized by high expression of the immunosuppressive proteins such as IL-10, transforming growth factor β (TGF- β) and IDO.^{34,55-57} Without proper pro-inflammatory signaling, TDLN DCs exist in an immature state. As such, TDLNs are often not capable of serving as effective sites of T cell priming.

Nevertheless, the TDLN appears to contain all of the components that would theoretically be required to generate antitumor T cell investigation and thus serves as a natural site of interest for immunotherapeutic intervention. Several investigators have reported antitumor efficacy following delivery of PRR agonists to the TDLN.^{52,58,59} Similar to analogous situations in the TME, STING activation in the TDLN is expected to trigger a pro-inflammatory program that results in DC maturation, expression of co-stimulatory molecules, and effective antigen presentation. Notably, IFN-I that is produced as a result of STING activation in the TDLN is known to serve as a 'signal 3' cytokine that is critical for CD8⁺ T cell activation,^{60,61} without which antigen presentation can lead to a short-lived and ultimately tolerogenic T cell phenotype.⁶²

Achieving efficient nanoparticle delivery to the TDLN involves exploiting differences in vascular and lymphatic transport in the TME. Due to the high rate of fluid transport by the vasculature relative to the lymph system⁶³, any administered drug that is capable of quickly crossing blood vessel walls is rapidly swept into the vasculature through convection. Although the vasculature in the TME is known to be significantly more porous than normal blood vessels (reaching pore sizes of up to hundreds of nm in diameter), the vast majority of blood vessel pores are typically on the order of ~10 nm in diameter.⁶⁴ Whereas small molecule CDN's easily pass through this transport barrier, larger nanoparticles are resistant to leakage into the vasculature. Meanwhile, transport to the lymph relies on weak pressure gradients originating from lymph and skeletal muscle cell contractions that force lymph fluid through interstitial cellular space⁶³, through which extremely large particles have difficulty trafficking. Achieving efficient lymphatic nanoparticle delivery is therefore a problem of balancing competing size effects; nanoparticles should be large enough to resist transport into the vasculature but small enough to easily drain into the lymphatics. Through empirical investigations of well-defined poly(propylene sulfide) nanoparticles, Reddy *et al.* reported that this balance is best achieved by nanoparticles greater than 20 nm in diameter and less than 100 nm in diameter, which have been reported to accumulate well in the LN following subcutaneous or IT injection.⁶⁵ Building on these successes, a rationally designed nanoparticle delivery platform can significantly improve CDN localization in the TDLN, addressing a weakness of CDN-based immunotherapy that is not easily addressed by small molecule engineering approaches.

Finally, a benefit of nanoparticle-mediated CDN delivery is the potential for improved tumor delivery following IV administration. Blood vessel defects in the vicinity of the TME present an opportunity to improve nanoparticle accumulation in tumor sites through the enhanced

permeation and retention (EPR) effect.⁶⁶ This effect once again arises from transport barriers that inhibit transport of nanoparticles across blood vessel walls. Due to differential pore sizes found in healthy and tumor associated vasculature, nanoparticles typically experience higher rates of extravasation in the vicinity of the tumor, an effect that drug delivery scientists routinely use to enrich administered cargo at the tumor site. Furthermore, nanoparticles larger than roughly ten nanometers typically can often avoid the renal ultrafiltration process, and thus may improve the circulation time of encapsulated drugs relative to direct administrations.⁶⁷ As such, IV administered CDN-loaded nanoparticles can passively accumulate in the TME and induce therapeutic benefit in a way that even high doses of free CDN have historically struggled to achieve.⁵³

1.6 Aims and Scope.

The research presented in this work details the use of nanoparticles to optimize the therapeutic potency of cGAMP. Chapter 2 describes the rational and iterative design choices that informed the optimized cGAMP-nanoparticle formulation (herein referred to as STING-NP), comprising self-assembled polymers encapsulating cGAMP. STING-NPs are stimulus responsive, ‘smart’ nanoparticles that protect and facilitate the endocytosis of cGAMP. I show that in the acidic endosomal environment, STING-NPs solvate molecularly, resulting intracellular delivery and endosomal escape of cGAMP to the cytosolic STING protein. I demonstrate that design choices relating to nanoparticle composition and formulation are critical to the efficacy of STING-NPs in several cell lines relevant to the TME.

Chapter 3 details the *in vivo* use of STING-NPs in murine cancer models. STING-NPs are shown to elicit tumor suppression and in some cases, complete tumor rejection in a variety of

tumor models. In addition to rejection of the tumor, treatment generates long lived, systemic antitumor immunity, as demonstrated through elicited resistance to rechallenge with follow up tumor cell inocula. Particular focus is given to characterization of the effect of the STING-NP on the tumor microenvironment. Treatment is shown to induce a multifaceted immune response, characterized by increased expression of pro-inflammatory proteins and chemokines with concomitant leukocyte infiltration, which most notably include a strong influx of activated CD8⁺ T cells. The development of systemic antitumor immunity following STING-NP treatment is shown to synergize well with checkpoint blockade both through IT and IV administration routes. Finally, STING-NPs are validated in an *ex vivo* model of IT treatment in melanoma tissue isolated from patients. Collectively, this set of experiments details the use of rational nanoparticle engineering to solve delivery challenges associated with a promising class of CDNs. The resulting STING-NPs are a promising immunotherapeutic treatment that can address several weaknesses in the current arsenal of standard-of-care treatments for cancer patients.

Chapter 2: Design and optimization of STING-NPs

2.1. Introduction.

Several critical design requirements were considered in the design of STING-NPs. We conceived of nanoparticles of less than roughly 100 nm in diameter to facilitate efficient cellular uptake and lymphatic trafficking. To increase circulation time for potential use in an IV administration route, we designed the particles to have a non-fouling surface coating to mitigate absorption of opsonizing serum proteins that mark nanoparticles for uptake and eventual clearance by the reticuloendothelial system (RES).⁶⁸ Importantly, the nanoparticle was also designed to facilitate rapid intracellular drug release and endosomal escape: a phenomenon that describes translocation of cGAMP from the endosome to the cytosolic STING protein following endocytosis.⁶⁹

Nanoparticle design was inspired by previous research focused on cytosolic delivery of nucleic acids. In particular, a large body of research has focused on the use of cationic polymers such as polyethylenimine (PEI) and poly(N,N-dimethylaminoethyl methacrylate) polymers as self-assembled delivery vehicles.⁷⁰⁻⁷⁵ Exploiting the polyvalent negative charge of nucleic acids, investigators noted that nucleic acids could complex with cationic polymers through charge-charge interactions into nanoscale ‘polyplex’ aggregates. Investigators have consistently reported many orders-of-magnitude-fold enhancements in nucleic acid potency using this strategy, in part due to polymer mediated endosomal escape of the nucleic acid. Following endocytosis, these cationic polymers protonate in response to the lowering pH of the endosomal compartment.⁷⁶ Progression of the endolysosomal acidification process requires continued influx of hydrogen and chloride ion pairs, which is thought to be concurrent with polymer swelling due to development of positive

charge on the polymer backbone. Collectively, these phenomena are referred to as proton-sponge effects, and are hypothesized to result in a positive osmotic pressure within the endosomal compartment that leads to rupture and leakage of endosomal drugs into the cytosol (**Figure 2.1**).⁷⁷

Cationic polymers are also thought to interfere with endosomal membrane integrity through direct interaction with the negatively charged phospholipid bilayer membrane. Several investigations into optimization of polymer chemistries for induction of endosomal escape have revealed that in general, hydrophobic modification of polyelectrolyte polymers appears to increase endosomolytic potency, likely by increasing interaction between polymer chains and lipid molecules comprising the endosomal membrane.^{70,75} This phenomenon can then induce endosomal destabilization by disrupting hydrophobic forces in the self-assembled lipid bilayer.

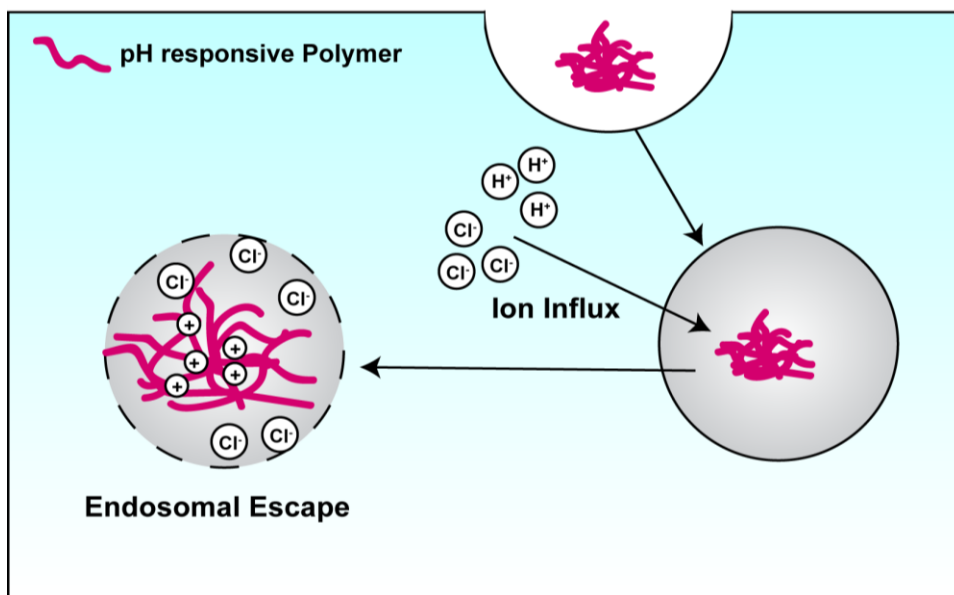


Figure 2.1 – pH responsive polymers mediate endosomal escape through the proton sponge effect. Following endocytosis, endolysosomal acidification brings hydrogen and chloride ion pairs into the endosome. The polymer chains buffer the hydrogen ions, leading to an expansion in specific chain volume. Excess Cl⁻ ions contribute to osmotic pressure differential in the endosome and cytoplasm, rupturing the endosomal membrane.

Recognizing that this class of carriers is well suited to mediate cytosolic cargo delivery, we sought to design a carrier that would leverage cationic and hydrophobic polymer chains for cGAMP delivery. In contrast nucleic acids however, CDNs do not demonstrate a large enough magnitude of polyvalent charge to stably complex to a positively charged polyelectrolyte. Whereas nucleic acids can simply be mixed with cationic polymer to form self-assembled nanoparticles, CDNs require formulation with bespoke polymers for nanoparticle formation. This work leverages block copolymers containing two spatially segregated blocks of differing hydrophilicity that provide the thermodynamic driving force for phase separation and particle self-assembly. Specifically, STING-NPs consist of a hydrophilic poly(ethylene glycol) (PEG) chemical block that is commonly used to inhibit protein absorption and particle opsonization⁶⁸ connected to a hydrophobic and pH responsive poly[(2-diethylaminoethyl methacrylate)-co-(butyl methacrylate)-co-(pyridyldisulfide ethyl methacrylate)] (DBP) copolymer block that was optimized for disruption of the endosomal membrane. The polymer (PEG-DBP) demonstrates reversible pH responsive behavior, capable of self-assembling into a PEG-shielded vesicle encapsulating an aqueous core loaded with cGAMP in physiological conditions while molecular solvating in endolysosomal pH to release cGAMP intracellularly. Following particle dissolution, unshielded blocks demonstrated endosomolytic behavior to mediate the endosomal escape of cGAMP (**Figure 2.2**). Notably, STING-NPs were crosslinked *in situ* through utilization of pyridyl disulfide (PDS) moieties, leading to a marked enhancement in STING-NP potency. Optimization of STING-NPs for cGAMP delivery was informed by an iterative process involving screening of several test polymers spanning a variety of synthesis parameters.

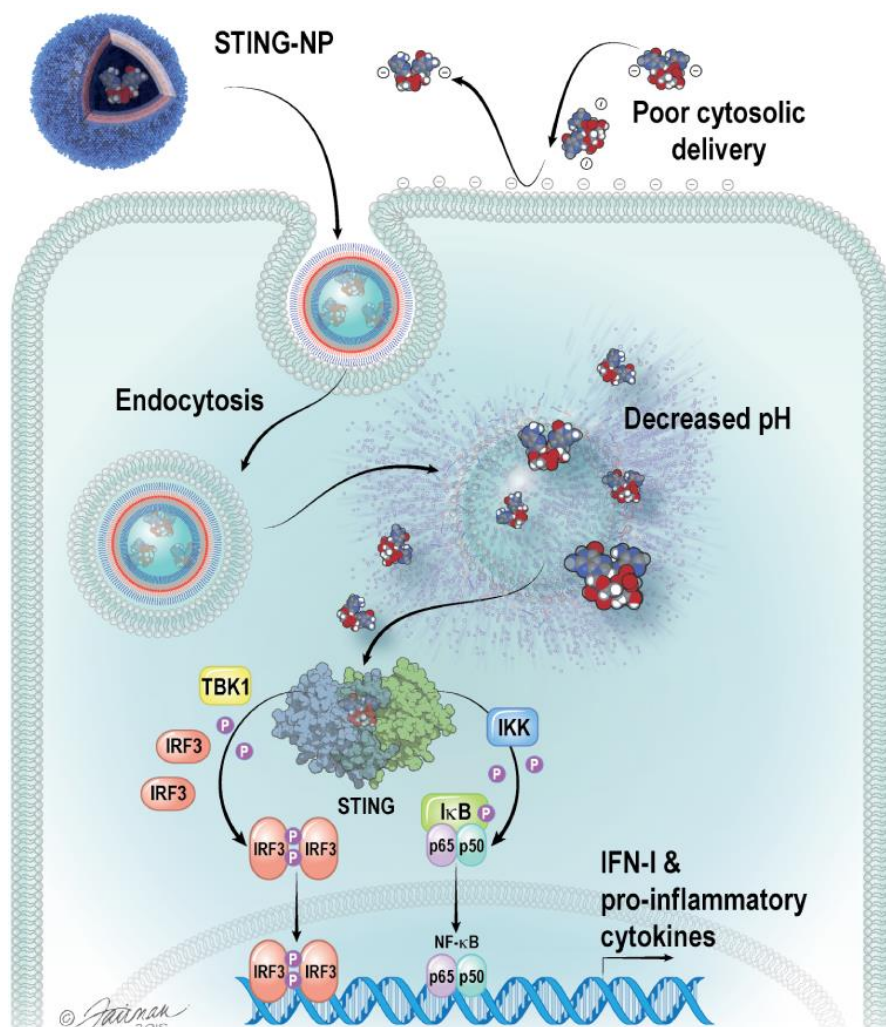


Figure 2.2 – STING-NPs are potent activators of the STING immune sensing pathway. STING-NPs comprise cGAMP molecules encapsulated by pH responsive and endosomolytic PEG-DBP polymers self-assembled into a PEGylated vesicular structure. Where free cGAMP molecules are repelled by the negatively charged cell membrane, STING-NPs are endocytosed. Endolysosomal acidification causes particle disassembly, unveiling membrane destabilizing DBP blocks that disrupt the endosomal membrane and allow cGAMP to escape to the cytosolic STING protein.

2.2. Design, Synthesis, and Optimization of STING-NPs.

PEG-b-DBP polymers were synthesized using reversible addition fragmentation transfer (RAFT) polymerization, a facile and versatile technique that produces well-defined polymer chains with a relatively low polydispersity index (PDI).^{78–80} Composition and length of the hydrophobic DBP block was controlled through changing monomer and chain transfer agent (CTA) ratios in the feed of the polymerization reaction, which allowed for rapid synthesis and

screening of PEG_x-DBP_y polymers for cGAMP delivery, where x and y denote the molecular weights of each polymer block. All polymers included a molar ratio of 6:4 of 2-(diethylamino)ethyl methacrylate (DEAEMA) to butyl methacrylate (BMA) monomers comprising the hydrophobic block of the polymer, which was reported by Manganiello *et al.* to exhibit an optimized balance of hydrophobic and cationic material,⁸¹ achieving three design criteria that are critical for achieving efficient cytosolic drug delivery. First, this composition contains sufficient BMA groups to impart an overall hydrophobic character into the DBP polymer block at physiological pH, generating the thermodynamic driving force to mediate separation of the polymer chain into a hydrated PEG corona and DBP interior phase. Second, inclusion of sufficient DEAEMA moieties in the pH responsive block ensures that that self-assembled nanoparticle demonstrates pH responsive behavior. Upon being exposed to acidic conditions, development of positive charge in the DEAEMA amines results in a shift in the DBP block to a hydrophilic state, eliminating any driving force for self-assembly and causing molecular solvation of the polymer chains. Finally, this balance of DEAEMA and BMA has been reported to mediate potent endosomal membrane disruption due to a balance of proton sponging and cationic DEAEMA groups and hydrophobic BMA moieties.

With this DEA:BMA ratio, STING-NPs comprise PEG_{2k}-DBP_{4.5k} with an addition of thiol reactive pyridyl disulfide (PDS) moieties for post-assembly crosslinking. To maximize cGAMP loading, polymer was formulated with cGAMP using a modified direct hydration method⁸² in which polymer is solvated in the minimum amount of organic solvent. An equivalent volume of maximally concentrated cGAMP in water was then added to the formulation mixture to drive self-assembly and allowed to equilibrate before eventual dilution and dispersion of polymersomes into an injectable formulation. In contrast to more dilute formulation methods such as solvent or pH

exchange in which polymersomes are formed in a relatively large reservoir water/drug solution, direct hydration ensures that polymersomes are formed at the highest possible polymer to encapsulant volume ratio to maximize encapsulation efficiency (EE). After dilution, polymersomes were then crosslinked *in situ* via addition of dithiothreitol (DTT) to induce partial reduction of PDS groups, resulting in formation of disulfide crosslinks between polymer chains (Figure 2.3).

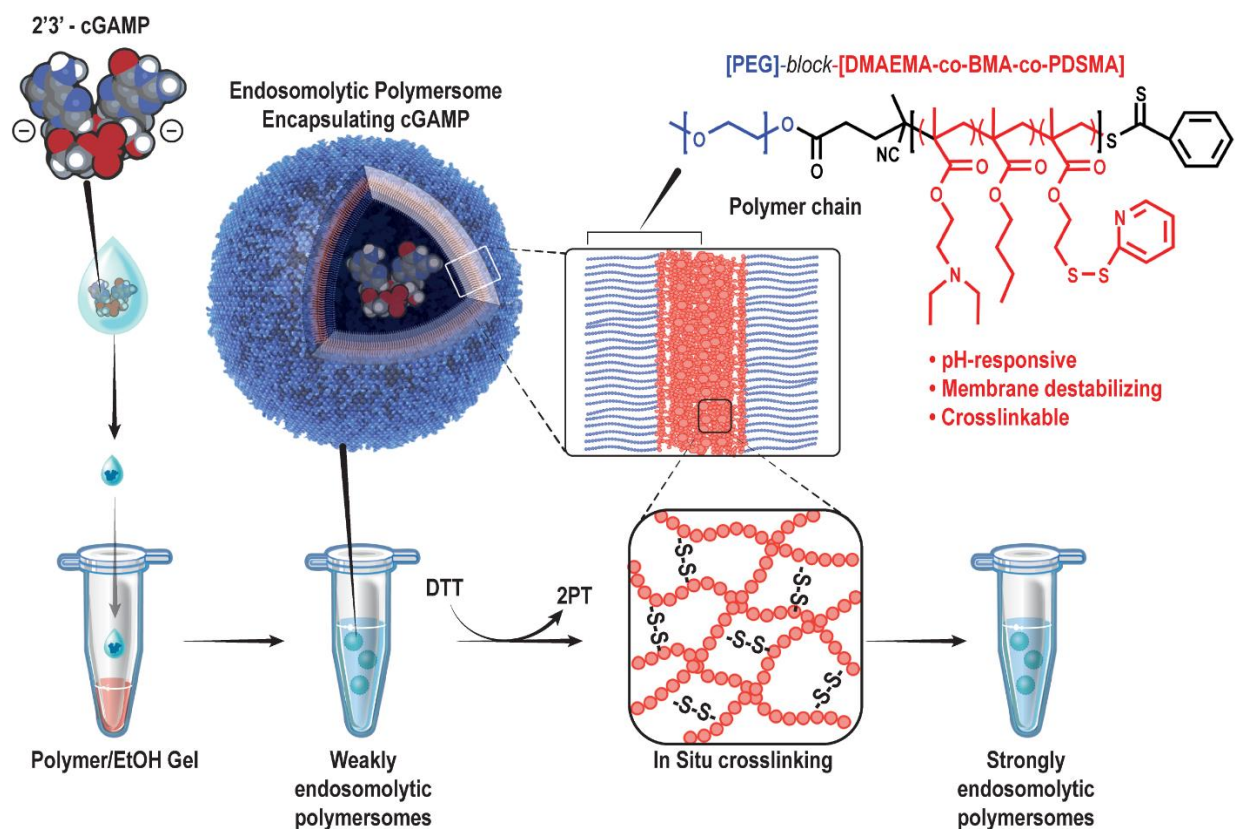


Figure 2.3 – Formulation of STING-NPs. STING-NPs comprise PEG-DBP polymer chains, which contain a pH responsive (DEAEMA), membrane destabilizing (DEAEMA + BMA), and crosslinkable (PDSMA) hydrophobic block. Polymers are dissolved in the minimum amount of ethanol, followed by addition of concentrated aqueous cGAMP to drive phase separation and self-assembly into a polymer gel. Further addition of water and sonication disperses this gel into PEGylated vesicles encapsulating cGAMP. Polymersome are then treated via addition of DTT to create disulfide crosslinks in the polymersome bilayer, causing release of 2PT (2-pyridinethione) as a byproduct, and increasing the endosomolytic activity of the formulation.

The resulting nanoparticles were PEGylated vesicles with a number average hydrodynamic radius of ~80 nm. Polymerization conditions were chosen to incorporate an average of ~2 PDS groups per chain to prevent the formation of a fully crosslinked network structure within the vesicle bilayer. STING-NPs therefore retained pH-responsive functionality after crosslinking, as observed through a sharp decrease in nanoparticle diameter when exposed to acidic pH (**Figure 2.4a**). Dynamic light scattering (DLS) analysis before and after crosslinking revealed no clear evidence of shifts in particle size distribution, suggesting that crosslinking largely occurs within the bilayer of any given particle (**Figure 2.4b-d**). Formation of large aggregates driven by thiol-PDS reactivity was therefore not a concern in STING-NP formulations. Zeta potential measurement of the formulation at pH 7.4 revealed a neutral surface charge despite the presence of cationic amines within the PEG-DBP chains, consistent with a well-assembled, PEG shielded nanoparticle (**Figure 2.4e**). The vesicular structure and in particular presence of a hydrophobic bilayer in STING-NPs were then confirmed via conventional and cryogenic electron microscopy (**Figure 2.4f-g**). Chain crosslinking was observed directly via gel permeation chromatography (GPC), which revealed nearly a doubled number average molecular weight ($M_n=11$ kDa, PDI=1.2) of lyophilized polymer chains derived from STING-NPs treated with DTT (**Figure 2.5a**). Crosslinking was further confirmed via absorbance spectrophotometric observation of 2-pyridinethione release, a byproduct of the reduction of PDS (**Figure 2.5b**). Notably, the reaction appeared to approach completion following addition of 0.5 molar equivalents of DTT to every PDS moiety, with further addition of DTT having no effect on the absorbance peak associated with 2-pyridinethione. This suggests that both the PDS reduction and subsequent crosslinking reaction occur with nearly stoichiometric efficiency.

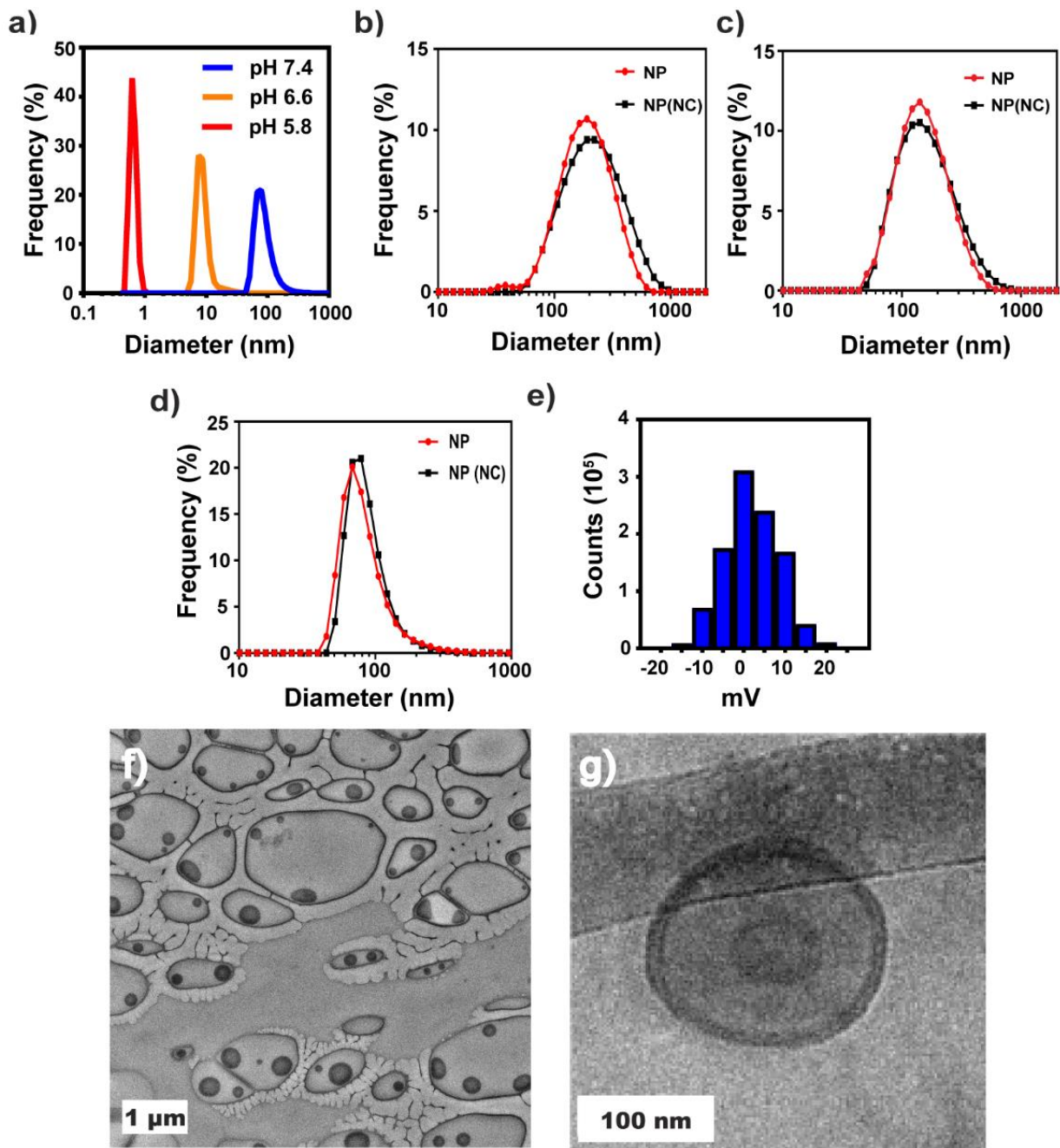


Figure 2.4 – Characterization of STING-NPs. a) Number average DLS traces indicating hydrodynamic diameter of crosslinked STING-NPs at various pH. b-d) Intensity, volume, and number average, respectively, DLS traces of crosslinked and non-crosslinked (NC) STING-NPs e) Zeta potential of crosslinked STING-NPs. f-g) Conventional and cryogenic, respectively, electron micrographs of STING-NPs.

Section 2.3. *In Situ* Crosslinking is Critical to Achieving Endosomolytic Potency and Vesicular Morphology in STING-NPs.

The pH-responsive, membrane destabilizing activity of polymersomes was evaluated using an erythrocyte hemolysis assay in which formulated nanoparticles are incubated with human red blood cells (RBCs) at various pH. By using the RBC membrane as a proxy for the endosomal bilayer, this assay approximates the ability of the polymer to mediate cell membrane destabilization at various pH⁸³ and is a relatively simple colorimetric assay that is commonly used to predict endosomolytic activity of drug carriers in a high throughput way. Testing a series of polymersomes reduced with different amounts of DTT revealed that in general, crosslinked polymersomes were more hemolytic than uncrosslinked analogues in acidic environments, likely a consequence of an increased number average molecular weight of the membrane destabilizing DBP blocks in chains comprising the polymersomes after crosslinking (**Figure 2.6a**). Notably, an optimum in crosslinking behavior was observed in NPs treated with 0.5 molar equivalents of DTT to every PDS functional group, conditions that are expected to lead to maximal crosslinking of the polymersome formulation. Importantly, all tested formulations induced negligible hemolysis at pH 7.4, indicating that hemolytic DBP blocks are well sequestered in the polymersome bilayer in physiological conditions. This indicated that PEG_{2k}-DBP_{4.5k} polymeromes were promising candidates for *in vivo* and specifically for IV administration, suggesting that formulations can be likely injected systemically without causing lysis of circulating red blood cells, which are well known to have minimal endocytic activity relative to myeloid cells.⁸⁴ This pH responsive, ‘smart’ functionality is at the core of STING-NPs, allowing the PEG corona to impart stealth behavior and biocompatibility to the nanoparticle platform while mediating potent membrane destabilization in endolysosomal conditions for cytosolic delivery of cGAMP.

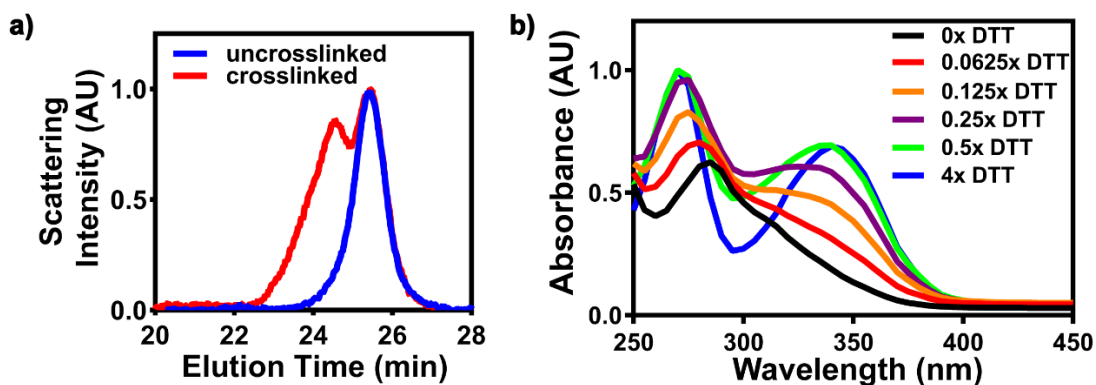


Figure 2.5 – Confirmation of STING-NP crosslinking. **a)** GPC trace of PEG_{2k}-DBP_{4.5k} polymer chains before and after crosslinking. Particles were formulated, crosslinked via addition of 0.5 molar equivalents of DTT per PDSMA group and lyophilized to generate the crosslinked polymer chains. **b)** UV-vis absorbance curves of STING-NPs crosslinked to varying degrees via addition of differing molar equivalents of DTT. DTT normalization is to total PDSMA moieties in the formulation. Reaction progress was analyzed through quantification of 2-pyridinethione absorbance ($\lambda=343$ nm) Nanoparticles were dissolved in pH 5.8 PBS prior to analysis to remove particle light scattering.

Observation of molecular weight dependent increases in hemolytic activity were consistent with analogous studies conducted on a series of PEG_{2k}-*bl*-(DEAEMA-*co*-BMA) (PEG_{2k}-DB_y) ranging from 7kDa to 38kDa in total molecular weight demonstrating a positive relationship between the length of the hydrophobic DB block and hemolytic behavior of the comprising polymer (**Figure 2.6b**). However, of tested polymers, only weakly hemolytic PEG_{2k}-DB_{5k} and PEG_{2k}-DBP_{4.5k} polymers self-assembled into vesicles capable of encapsulating cGAMP. Critically, longer and more hemolytic PEG_{2k}-DB_x polymer failed to self-assemble in aqueous media, instead forming poorly define aggregates likely due to insufficient hydrophilic material within the polymer chains required to stabilize increasing sizes of hydrophobic DB blocks (**Table 2.1, Figure 2.7**). This is consistent with several investigations of similar block copolymer (BCP) aqueous self-assembly properties in the literature, which have described a transition from vesicular to complex aggregate morphology at a hydrophilic weight fraction of $W_{\text{PEG}} \sim 0.25$.^{85–89}

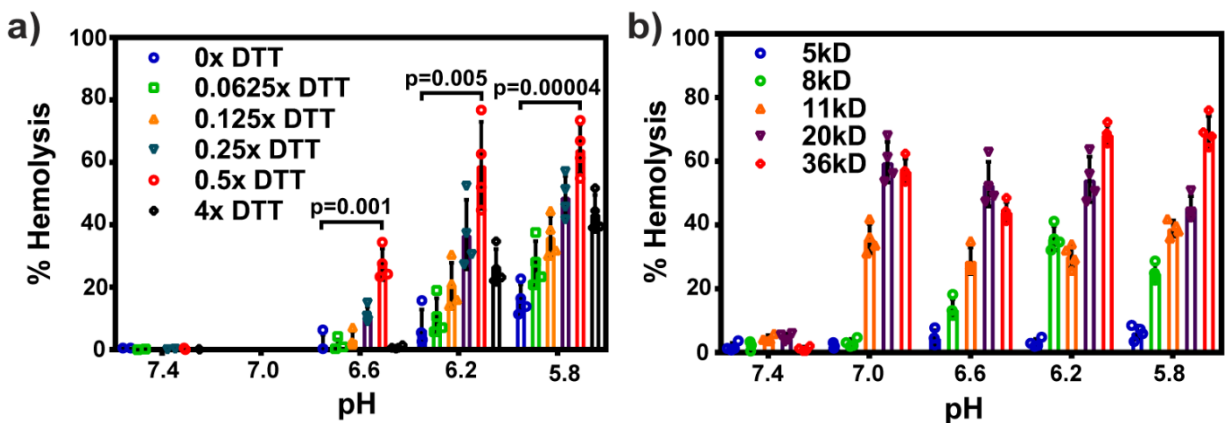


Figure 2.6 – Hemolysis of PEG_{2k}-EBP_{4.5k} and PEG_{2k}-EB_y formulations. a) Hemolytic activity of PEG_{2k}-EBP_{4.5k} polymersomes treated with varying amounts of DTT, normalized to total PDSMA moieties (One-way ANOVA, post-hoc Tukey test). b) Hemolytic activity of PEG_{2k}-DB_y polymers. The legend refers to molecular weight of the DB block. Data are presented as mean \pm SD.

To determine if hemolytic activity could be increased while maintaining a vesicular structure, we synthesized PEG-DB with larger PEG blocks (5 and 10 kDa), allowing us to synthesize BCPs with relatively large DB blocks. In the case of PEG_{10k}-DB_y this allowed us to synthesize DB blocks as high as 30 kDa while maintaining the boundary condition while maintaining the boundary condition $W_{\text{PEG}} > \sim 0.25$. However, all tested PEG_{5k}-DB_y and PEG_{10k}-DB_y self-assembled into wormlike and spherical micelles which were unsuitable for cGAMP encapsulation due to their lack of an aqueous core (**Table 2.1, Figure 2.7**). While these nanoparticles were capable of complexing to cGAMP through electrostatic interactions, encapsulation efficiencies were significantly lower than those observed for vesicular morphologies.

The inability of larger PEG-DB polymers to form self-assembled polymersomes is an interesting consequence of entropic effects due to polymer stretching within self-assembled morphology, and is consistent with previous reports in the literature.⁹⁰ BCP self-assembly is determined largely by three contributors to free energy: the interfacial energy between the hydrophobic core of the nanoparticles and the non-solvent medium, the loss of polymer entropy

arising from stretching of the hydrophobic blocks, and a similar loss of entropy arising from stretching in the hydrophilic block. All of these factors are affected by the surface area to core volume ratio of a self-assembled polymer morphology.

Table 2.1. Characterization of diblock copolymer properties, self-assembly behavior, and cGAMP encapsulation efficiency.

Polymer	DEAEMA(%) ^a	BMA(%) ^a	PDSMA(%) ^a	PDI ^b	EE ^c	W _{PEG} (%)	Morphology ^d
PEG _{2k} -b-DB _{5k}	36.3	36.3	0	1.23	45 ± 8	28.6	V
PEG _{2k} -b-DB _{7.8k}	61.7	38.3	0	1.09	0	20.4	P
PEG _{2k} -b-DBP _{4.5k}	57	35.2	7.8	1.01	38 ± 3	30.7	V
PEG _{2k} -b-DB _{10.8k}	67.4	32.6	0	1.08	N/A	15.6	P
PEG _{2k} -b-DB _{20k}	62.1	37.9	0	1.06	N/A	9.1	P
PEG _{2k} -b-DB _{36k}	61.6	38.4	0	NS	N/A	5.3	P
PEG _{5k} -b-DB _{9.2k}	65	35	0	1.14	16 ± 11	35.2	F
PEG _{5k} -b-DB _{14.3k}	59.5	40.5	0	1.23	18 ± 12	25.9	F+S
PEG _{10k} -b-DB _{21.2k}	58.9	41.1	0	1.14	16 ± 11	32.1	S
PEG _{10k} -b-DB _{30.2k}	57.3	42.7	0	1.23	12 ± 5	24.8	F+S
<p>^a Molar percent determined NMR</p> <p>^b Determined by GPC, NS: Not soluble in DMF mobile phase</p> <p>^c Encapsulation efficiency and morphology from direct hydration formulation. Determined <i>via</i> HPLC. Data are presented as mean ± SD. n=3 independent samples.</p> <p>^d Morphology determined by TEM. V = Vesicles, F = Fibrillar micelles, S = Spherical micelles, P = Macroscopic Precipitation</p>							

Geometric analysis of micelle versus bilayer self-assembled architectures readily reveals why corona stretching effects in large molecular weight polymers favor micellar assembly. The surface area of a polymer chain comprising a spherical micelle at the outer edge of the hydrophobic core is given by⁸⁷:

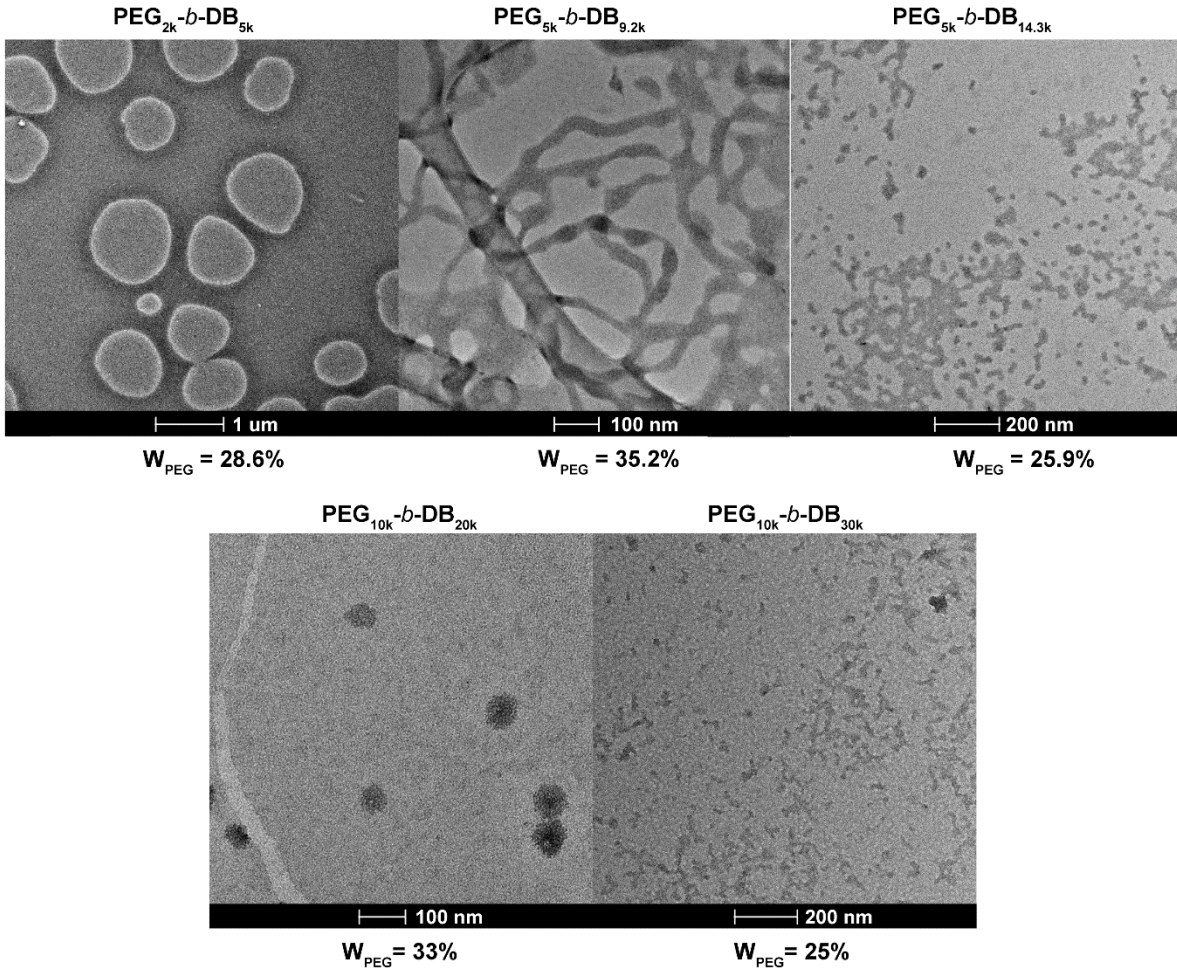


Figure 2.7 – Self-assembled morphologies of PEG_x-DB_y BCPs. Electron micrographs of self-assembled PEG_x-DB_y BCPs. Polymers were drop cast on carbon grids and stained with methylamine tungstate to improve contrast of nanoparticles. Excess stain was washed away, leaving a positively stained sample for imaging.

$$A_S = \frac{4\pi R_{SM}^2}{N_{agg}} \quad (2.1)$$

Where A represents the surface area of the hydrophobic core, R represents the radius of the hydrophobic core, N_{agg} represents the aggregate number of a nanoparticle and the S subscripts represent a spherical micelle morphology. The volume contribution to the hydrophobic core of an individual chain is given by:

$$V_S = \frac{4\pi R_S^3}{3N_{agg}} \quad (2.2)$$

By combining 2.1 and 2.2 we can calculate:

$$A_S = \frac{3}{R_S} V_S \quad (2.3)$$

Similarly, for a cylindrical morphology:

$$A_C = \frac{2}{R_C} V_C \quad (2.4)$$

And for a idealized bilayer morphology:

$$A_B = \frac{1}{R_B} V_B \quad (2.5)$$

For simplicity, we assume that R_S , R_C and R_B are influenced only by the number of repeat units in the hydrophobic DB block, and are thus equal. Similarly, we assume that the density of the hydrophobic material is not affected by its self-assembled morphology. Thus on a per-chain basis, $V_S = V_C = V_B$, from which, it is clear that $A_S > A_C > A_B$. As the degree of stretching in the PEG corona block decreases as the amount of per-chain surface area of the self-assembled morphology, nanoparticles are formulated from polymers with larger PEG blocks (i.e PEG_{5k} and PEG_{10k}) that require a relatively large surface area to retain an unstretched and higher entropy state, they are thermodynamically biased away from vesicular structures even at a W_{PEG} that may be amenable to polymersome formulation for lower molecular weight chains. This effect is more easily visualized using a geometric curvature argument; put simply, as the length of the corona block increases, a higher curvature self-assembled geometry will be preferred to maximize the available surface area and volume for the hydrophilic polymer block (**Figure 2.7**).

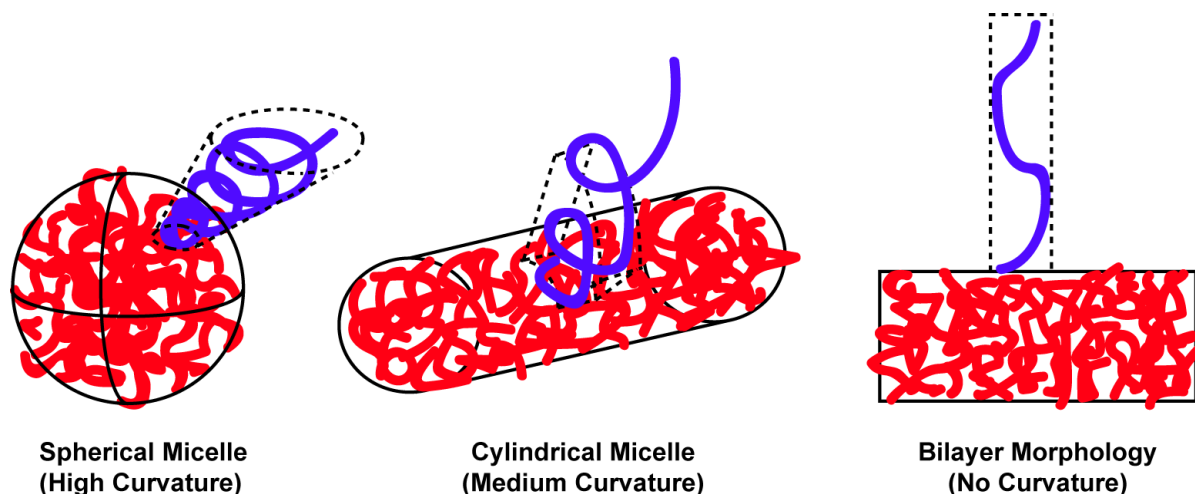


Figure 2.7 – The effect of self-assembled morphology on stretching of the polymer corona block. Curvature in the spherical micelle structure maximizes the surface area available for the corona block, allowing the hydrophilic block to maintain an un-stretched state. Dotted borders represent the amount of space allowed for the hydrophilic portion of a single chain in the corona. Bilayer structure has no curvature in either direction on the hydrophobic core surface; the corona block is forced to stretch to accommodate hydrophilic material in a limited surface area, leading to a loss in corona entropy. Cylindrical micelle architecture is an intermediate between the spherical micelle and bilayer morphology, with curvature in only one direction on the hydrophobic core surface. Schematic is simplified to represent idealized structures, as cylindrical micelles and bilayers comprising vesicles typically bend in realistic colloids.

A second reason why higher molecular weight polymer chains favor spherical and cylindrical structures involves the interfacial surface area of the particles and the degree of stretching found in the hydrophobic core blocks. Provided that repulsive effects in the corona are not strong enough to destabilize the nanoparticle, the self-assembled morphology in general favors minimizing surface between the hydrophobic core and the non-solvent media to minimize interfacial surface tension. This effect generally favors high particle aggregation numbers, as the total interfacial energy in the system is proportional to the total number of aggregates in the colloid. While the aggregate number is limited in spherical micelles by the degree of polymerization in the polymer chain as the radius of the particle cannot exceed the length of a fully extended polymer chain, it is in principle unbounded in a bilayer morphology that can extend as long as necessary to incorporate all free chains. Thus for lower molecular weight polymer chains, assuming a spherical

micelle morphology requires formation of a relatively large number of aggregates to incorporate all polymer chains, resulting in a concomitantly high total interfacial energy. By contrast, total interfacial energy can be minimized through assembly into a bilayer architecture due to the ability of this morphology to increase particle aggregation number. As polymer molecular weight increases however, specifically the molecular weight of the hydrophobic block, nanoparticles with larger core diameters are naturally formed, allowing for incorporation of polymer chains in a smaller number of total aggregates due to the cubic scaling of volume in a spherical geometry. Thus the differential between surface area of nanoparticles between spherical and bilayer morphologies decreases, once again with an associated decrease in total system surface tension. Collectively, these effects can be interpreted as a relative driving force towards micellar morphologies as overall polymer molecular weight increases (**Figure 2.8**).

This can be formalized mathematically by making the simplifying assumption of a dry polymer core. In this condition, the surface area of a bilayer is:

$$SA_B = N_{ch}A_{ch} \quad (2.6)$$

where SA_B is the surface area of the sphere, N_{ch} is the total number of polymer chains, and A_{ch} is the surface area per chain of the hydrophobic core in a bilayer morphology. The surface area of a sphere is given as:

$$SA_S = N_p * 4\pi R^2 \quad (2.7)$$

where N_p represents the total number of self-assembled particles in solution, R represents the particle radius, and the S subscript represents a spherical geometry. As the total amount of hydrophobic mass must be accounted for in self-assembled particles, we have:

$$M_{hyd} = \rho_c * 4/3\pi R^3 * N_p \quad (2.8)$$

where M_{hyd} represents the total amount of hydrophobic mass in solution, and ρ_c represents the density of material in the particle core. Combining (2.7), (2.8), we can derive:

$$SA_S = \frac{3M_{hyd}}{R*\rho_c} \quad (2.9)$$

Finally, combining (2.6), (2.9) and a basic surface energy equation, we can derive the surface energy differential between the two morphologies:

$$\Delta H(interfacial)_{B \rightarrow S} = \left(\frac{3M_{hyd}}{R*\rho_c} - N_{ch}A_{ch} \right) * \gamma \quad (2.10)$$

where γ represents the per area surface tension between the hydrophobic core and aqueous media. Assuming that ρ_c is constant in both low and high molecular weight chains, we see clearly that the first term decreases as larger polymer chains lead to higher R. In the second term, A_c is likely to increase as polymer chains increase in size, with the PEG corona demanding increasing surface volume to maintain an unstretched state. Thus, we once again see that the interfacial energy difference between spherical and bilayer morphologies generally decreases as the molecular weight of the of the polymer chain increases. Using similar geometric arguments, an analogous relationship can be derived for cylindrical nanoparticles:

$$\Delta H(interfacial)_{B \rightarrow cylinder} = \left(\frac{2M_{hyd}}{R*\rho_c} - N_cA_c \right) * \gamma \quad (2.11)$$

Thus, there is a thermodynamic driving force towards micellar morphologies for large polymer chains, with all other influencing factors held constant. This effect is driven by a combination chain stretching both in the nanoparticle corona and hydrophobic core, as well as a tendency for self-assembled particles to minimize interfacial surface tension between the hydrophobic core and the aqueous medium.

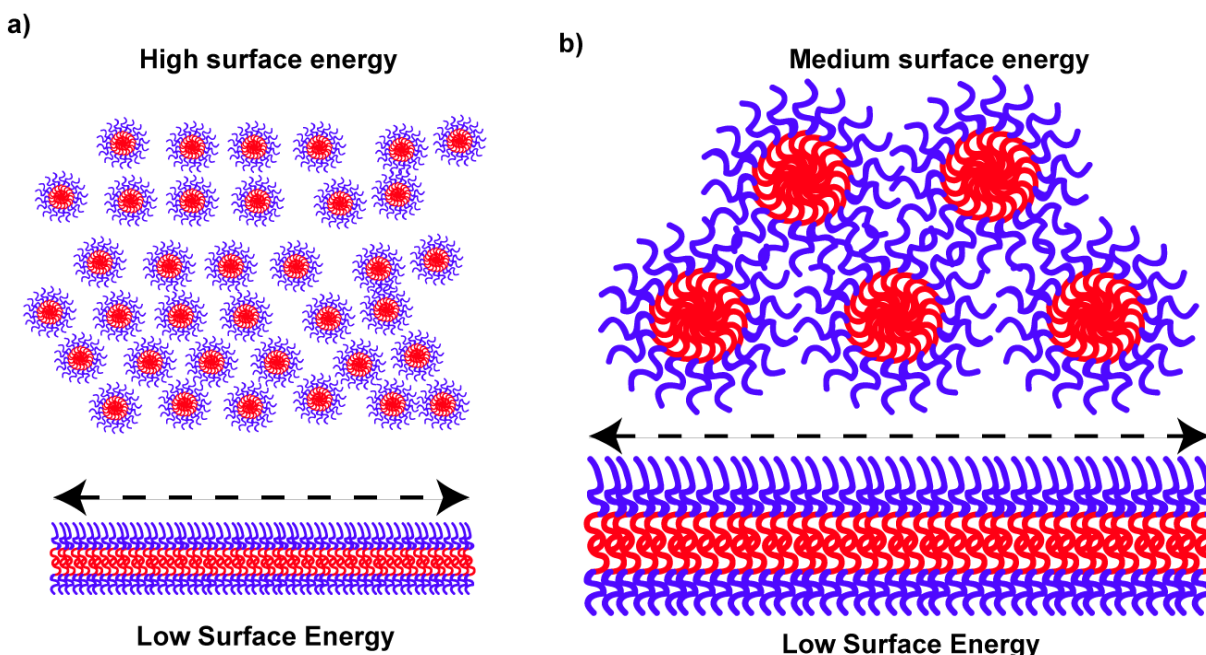


Figure 2.8. The effect of particle diameter on interfacial surface tension. **a)** For low molecular weight polymers, limited core radius R requires a self-assembly of a large number of nanoparticles with a low aggregation number N_{agg} to incorporate all polymer chains. This leads to a high system surface tension, which is proportional to $4\pi R^2/N_{agg}$. There is a large differential in total surface area between bilayer and spherical morphologies. **b)** For high molecular weight polymers, an increase in particle R mitigates this effect by increasing the allowable N_{agg} .

In summary, our experiments revealed an inherent tension in achieving both potent endosomolytic activity and a vesicular morphology in PEG-DB polymers that motivated the use of an *in situ* crosslinking strategy for STING-NPs; while high molecular weight ($>10\text{kDa}$) DB blocks were required to mediate efficient endosomal escape, they were incapable of vesicular self-assembly even when extended off of larger PEG_{5k} and PEG_{10k} blocks. These effects of synthetic parameters on self-assembled morphology are well supported both in theory and in empirical reports found in the literature.⁹⁰ Through combination a formulation method using relatively low molecular weight and poorly hemolytic PEG_{2k}-DBP_{4.5k} polymer chains with post-assembly crosslinking, STING-NPs are able to efficiently encapsulate cGAMP while serving as potent mediators of endosomal escape.

Section 2.4. Evaluation of the Direct Hydration Method for cGAMP Encapsulation.

Drug encapsulation in self-assembled polymersomes is a complex process that involves transition of polymer chains from a bulk or well-solvated state to a vesicular morphology. Neglecting for the moment any interactions that may cause preferential association of the encapsulant to the polymer chains as well as any leakage or particle loss that may occur during the purification process, drug encapsulation efficiency is the ratio of the sum total of aqueous media encapsulated within all nanoparticles to the amount of total media in the formulation reservoir. As previously stated, the formulation method involves solubilization of PEG_{2k}-DBP_{4.5k} in a minimal amount of ethanol, followed by addition of aqueous addition of cGAMP. The mixture is allowed to equilibrate, and additional water is added slowly to ensure that particle formation and closure of the vesicular bilayer occurs at as high a concentration as possible. This subsection attempts to give theoretical estimates of maximum encapsulation efficiency using this method and demonstrates that they are in line with experimental results.

The direct hydration method, first described by O'Neill *et al.*,⁸² appears to be inspired in part by work by Battaglia and Ryan, in which investigators detail the evolution of poly[(EG)-b-(butylene oxide)] (PEG-b-BO) from the bulk to a dispersed vesicular morphology through a bicontinuous sponge intermediate phase as additional amounts of nonsolvent (water) are added.⁹¹ The sponge phase consists of stacked vesicular precursors containing curved bilayers that have not fully closed yet to entrap the encapsulant. The direct hydration method seeks to load cGAMP within these vesicular precursors, and thus the encapsulated volume fraction at the point of transition from this sponge phase to fully closed vesicles theoretically is the maximum encapsulation efficiency for this formulation method.

While we did not perform detailed characterization of this vesicular precursor phase for our polymers, we can arrive at a theoretical encapsulation efficiency by looking at the evolution of similar systems in the literature. Alexandridis *et al.* examined the sponge phase in similar PEG-b-BO BCPs *via* small angle x-ray scattering, which revealed a well-ordered body centered cubic (BCC) crystal lattice (**Figure 2.9**).^{91,92} Assuming that transition from precursors to vesicles occurs from this lattice, and making the simplifying assumption of monodisperse vesicles of 80 nm in diameter, we can calculate a theoretical entrapped volume using simple geometric arguments. The unit cell of a BCC contains two atoms and has spatial dimensions of:

$$a = \frac{2D}{\sqrt{3}} \quad (2.12)$$

where a is the length of one side of the cubic unit cell and D is the diameter of the repeating sphere. There are two atoms per unit lattice. The encapsulated volume is then:

$$V_e = 2 * \frac{4/3\pi(R-T)^3}{a^3} \quad (2.13)$$

Where V_e is the encapsulate volume, R is the radius of the repeating sphere, and T is the thickness of the vesicle bilayer. From cryo-EM imaging, we approximate the bilayer of the nanoparticle as ~14nm in thickness. Combining (2.12 - 2.13) we can thus calculate that $V_e = 18.7\%$.

Given the many assumptions required to arrive at that number, we here present an alternative method of approximating V_e . Battaglia and Ryan reported for their PEG-BO system that transition from the sponge to vesicular morphology occurred between 10 and 30 wt% of polymer in non-solvent. Assuming that transition occurs around a similar weight percent for PEG_{2k}-DBP_{4.5k}, we can determine that polymersomes become fully formed in a reservoir of roughly 10-20 microliters of nonsolvent per milligram of polymer in the formulation feed.

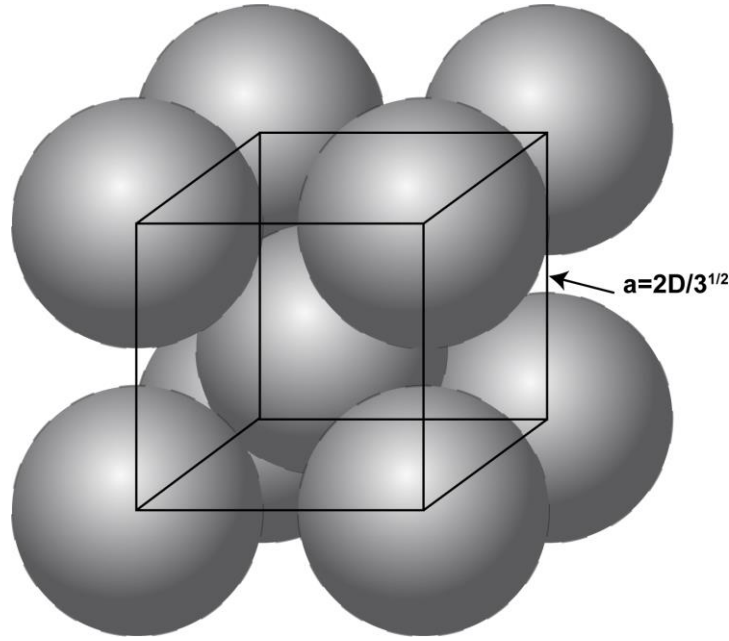


Figure 2.9. Schematic of the BCC unit cell. a represents the dimensions of the cubic unit cell, and D represents the diameter of the repeating sphere. The number average hydrodynamic radius of nanoparticles determined by DLS is substituted for D for volume calculations.

This method of V_e approximation allows for use of a polydisperse nanoparticle size distribution. Frequencies of nanoparticle size are provided as a table and used for subsequent calculations (**Appendix A.1**). Assuming a fixed polymer density, we can calculate the amount hydrophobic material required to comprise the bilayers of nanoparticles in a given size distribution using a mass balance:

$$\frac{M_{hyd}}{\rho_{hyd}} = N * \sum \left(\frac{4\pi}{3} x_i (R_i^3 - (R_i - T)^3) \right) \quad (2.14)$$

Where M_{hyd} and ρ_{hyd} represent the total mass and density of the hydrophobic material, T represents the thickness of the polymersome bilayer, R_i and x_i represent the radius of a nanoparticle and the frequency of that nanoparticle, and N represents the total number of formed polymersomes in the formulation. The amount of volume in the formulation feed at the point of vesicle formulation in an ideally equilibrated mixture, again assuming fixed densities, is:

$$Total\ Volume = M_T / \rho_{pol} + \left(\frac{M_T}{W_T} - M_T \right) / \rho_{solvent} \quad (2.15)$$

Where M_T represents the total mass of polymer in the system, W_T represents the weight fraction of polymer in nonsolvent at the point of vesicle formation, and ρ_{pol} and $\rho_{solvent}$ represents the density of the polymer and nonsolvent, respectively. The amount of encapsulated volume at the point of transition is:

$$V_e = N * \Sigma\left(\frac{4\pi}{3} x_i (R_i - T)^3\right) \quad (2.16)$$

Finally, from equations (2.14-2.16) in combination with empirically determined values, V_e can be approximated. We use the value of $T \sim 14\text{nm}$, ρ_{pol} and $\rho_{hyd} \sim 1.1 \text{ mg}/\mu\text{L}^3$, $\rho_{sol} = 1 \text{ mg}/\mu\text{L}^3$ and values for R_i and x_i derived from dynamic light scattering measurements. For PEG_{2k}-DBP_{4.5k}, $M_{hyd} = 0.69 * M_T$. Taking the values of $30\% > W_T > 10\%$ that were reported by Battaglia and Ryan for PEG-b-BO BCPs and substituting in all terms and combining equations (2.14-2.16), we can calculate that $22\% > V_e > 7.2\%$, depending on the transition point W_T .

Thus, we have calculated two theoretical loading efficiencies that are in agreement with each other using a different set of assumptions, with a maximum encapsulation efficiency of roughly 20%. Notably, this is significantly lower than the observed experimental encapsulation of 38% for PEG_{2k}-DBP_{4.5k} vesicles. In table 2.1 however, we also see that several of the self-assembled micellar morphologies were capable of ‘encapsulating’ cGAMP, which is likely due to electrostatic interactions between cGAMP and the positively charged DEAEEMA within the hydrophobic core. We thus expect some contribution to measured encapsulation efficiency in STING-NPs due to loading of cGAMP within the hydrophobic phase of the material. We expect complexation efficiency to largely depend on the ratio of positively charged cationic groups to negatively charged cGAMP molecules, and notably to be relatively independent of self-assembled morphology. As such, a reasonable approach to modeling the encapsulation of cGAMP in STING-NPs is to sum the contributions of electrostatic complexation and physical encapsulation, the former of which

we expect to be similar to magnitudes of complexation observed in non-vesicular morphologies. Referring again to table 2.1, we see that complexation efficiencies for PEG-DB micelles were found to be between 12 and 18%, which is sufficient to close the gap between measured encapsulation efficiencies and theoretical encapsulated volume in the direct hydration formulation method.

Section 2.5. *In Vitro* Validation of STING-NP Activity.

Given the critical role of IFN-I in antitumor immunity,^{93,94} we evaluated the ability of STING-NPs to stimulate IFN-I responses in monocyte, macrophage, and melanoma cell lines (**Figure 2.10a**). Delivery of cGAMP in crosslinked PEG-DBP vesicles increased cGAMP activity by several orders of magnitude ($EC_{50} = 67 \pm 12$ nM, 36 ± 14 nM, and 230 ± 1.0 nM in THP-1 ISG, RAW ISG, and B16 ISG cell lines, respectively), whereas free cGAMP elicited little response even at high concentrations ($EC_{50} = 31 \pm 1$ μ M, 22 ± 4 μ M, 55 ± 2 μ M). We observed a relationship between hemolytic activity at endosomal pH values and increased STING-NP activity, as weakly hemolytic PEG-DB and uncrosslinked PEG-DBP vesicles only modestly increased cGAMP activity.

Mixing cGAMP with pre-formulated vesicles resulted in a negligible increase in activity, indicating that cGAMP encapsulation was critical to efficient STING activation. This finding was further supported by evaluating the activity of PEG-DB polymers that did not form vesicular structures. Although we observed some association between cGAMP and the micellar structures formed using higher molecular weight PEG-DB polymers, we found that these morphologies mediated minimal enhancements in cGAMP activity despite being highly hemolytic (**Figure 2.10b**). This highlights an important distinction between delivery of oligonucleotide therapeutics

(e.g., siRNA), which can be stably complexed to cationic carriers via a multivalent electrostatic interaction,⁹⁵ and CDNs, which may lack a sufficient degree of charge for stable electrostatic complexation with DEAEEMA groups.

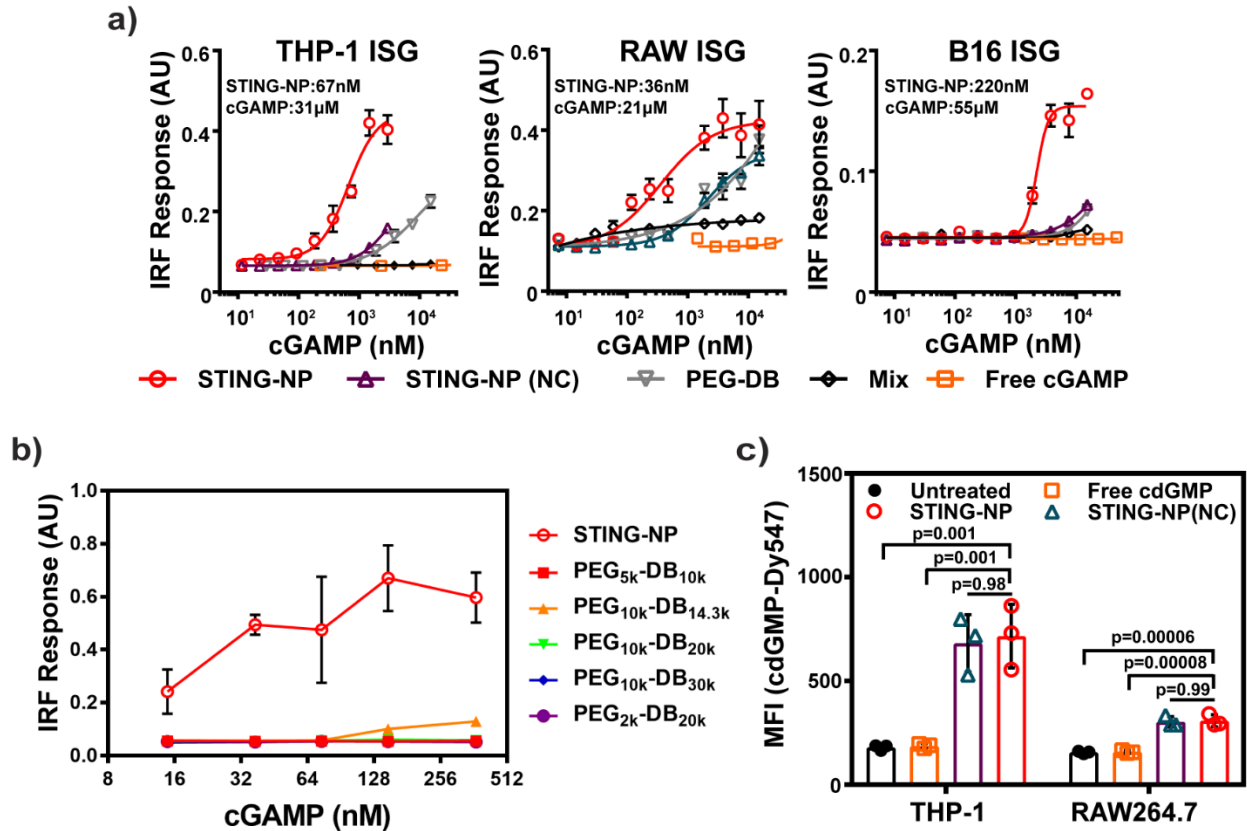


Figure 2.10 – STING-NPs dramatically enhance cGAMP potency by enhancing cytosolic delivery efficiency. **a)** Relative IRF3 response of reporter cell lines following treatment with cGAMP formulations for 24h. Mix denotes a mixture of free cGAMP and empty crosslinked PEG_{2k}-DBP_{4.5k} polymersomes. **b)** Comparison of IRF3 response elicited by STING-NPs and a series of hemolytic PEG_x-DB_y cGAMP formulations in reporter THP-1 cell lines, 24h after treatment. **c)** Quantification of cdGMP-Dy547, a fluorescent CDN analog, uptake in THP-1 and RAW264.7 cell lines treated for 2h. All data are presented as mean ± S.D. Statistical test: one-way ANOVA with post-hoc Tukey test.

We next evaluated the capacity of polymersomes to enhance cellular uptake of cGAMP by co-encapsulating cGAMP with a fluorescently labeled CDN (cdGMP-Dy547). While cdGMP-Dy547 uptake varied between cell types, STING-NPs increased uptake ~1.5-3.5x, with no significant differences observed between crosslinked and uncrosslinked STING-NPs (**Figure 2.10c**). While some increase in cGAMP activity can be attributed to enhanced intracellular uptake,

the magnitude of reduction in EC50 achieved with STING-NPs is likely primarily a consequence of enhanced endosomal escape and cytosolic delivery of cGAMP. Hence, by combining precisely designed diblock copolymers, a formulation method that enables high cGAMP encapsulation efficiency (~38%), and vesicle membrane crosslinking to enhance endosomolytic activity, STING-NPs enhance cGAMP potency 240-610 fold, the largest carrier-mediated fold-increase in CDN activity reported to date.^{51,96}

DCs are key players in the T cell priming process, and examining the activity of STING-NP treatment on the DC phenotype is critical to evaluating the potential of STING-NPs as an antitumor therapeutic. Quantification of IFN-I via ELISA in treated DC 2.4 dendritic cells revealed similar trends to those described above, with STING-NPs acting as much more potent activators of IFN-I production than free cGAMP (**Figure 2.11a**). To further validate STING-NPs beyond their ability to elicit IFN-I production, we treated bone marrow derived dendritic cells (BMDCs), which we expect to be more representative of DCs found *in vivo*, to determine whether or not STING-NPs could induce dendritic cell maturation. 24h after treatment with STING-NPs, BMDCs exhibited increased surface expression of antigen presenting MHC-I and MHC-II molecules and costimulatory CD40, CD80, and CD86 molecules (**Figure 2.11b-f**). Consistent with data in cell lines, STING-NPs were more potent inducers of DC maturation marker expression than was free cGAMP. Similarly, bone marrow derived macrophages (BMDMs) were isolated and polarized via IL-4 exposure to an immunosuppressive M2 phenotype. 4h after treatment, qPCR analysis revealed that STING-NP treated BMDMs repolarized to a pro-inflammatory M1 phenotype, with increased expression of *Ifnb1* and *Tnf* genes and decreased expression of the immunosuppressive *Tgfb* and *Arg1* genes (**Figure 2.12**). These data demonstrate that STING-NPs induce desirable phenotypic changes in cell types that are implicated in failure of antitumor immunity in the TME.

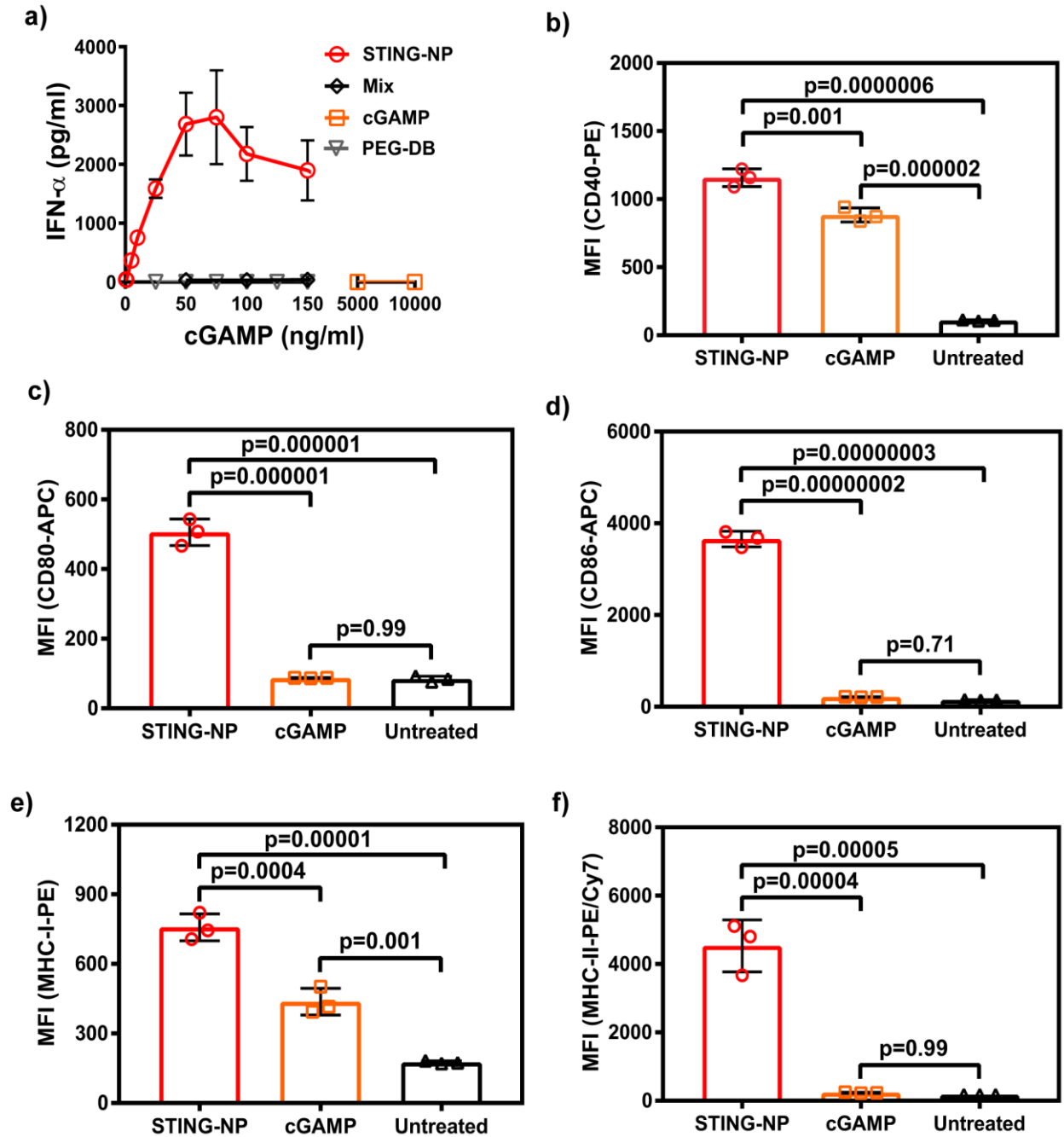


Figure 2.11 – STING-NPs induce IFN-I production and expression of antigen presentation/co-stimulatory proteins in DCs. **a)** Quantification of IFN- α produced by cultured DCs after treatment with various cGAMP formulations. **b-f)** Median fluorescent intensity (MFI) of co-stimulatory molecules CD40, CD80, and CD86 and antigen presentation molecules MHC-I and MHC-II in BMDCs following treatment with STING-NP or cGAMP.

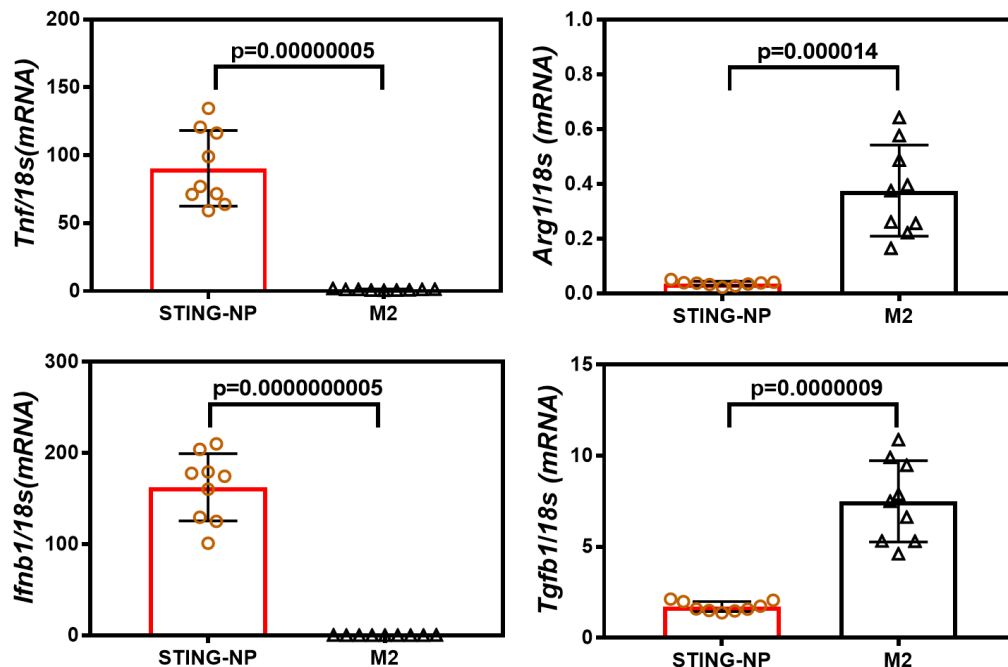


Figure 2.12 – STING-NPs reprogram M2 polarized bone marrow derived macrophages to a pro-inflammatory M1 phenotype. qPCR quantification of expression of M1 related genes with pro-inflammatory, tumoricidal function (*Ifnb1*, *Tnf*) and M2 immunosuppressive genes (*Arg1*, *Tgfb1*) following STING-NP treatment.

Section 2.6. Conclusion.

In summary, this chapter has focused on the design and optimization of crosslinked PEG_{2k}-DBP_{4.5k} polymers for cGAMP delivery. Using hemolysis assays, we established a positive relationship between membrane destabilizing activity and molecular weight of DB blocks comprising block copolymers. We exploited this relationship to improve the potency of STING-NPs using an *in situ* crosslinking strategy. Furthermore, we demonstrate that *in situ* crosslinking is critical to achieving an endosomolytic polymersome formulation due to entropic factors that favor micellar self-assembly in high molecular weight block copolymers.

STING-NPs appear to be well suited for *in vivo* administration, self-assembling into ~80nm particles that are well suited for cellular uptake and lymphatic drainage. Particles were PEG-shielded and surface neutral, mediating negligible cytotoxicity to RBCs in physiological pH. Meanwhile, STING-NPs maintain a pH-dependent disassembling functionality to mediate

intracellular release and endosomal escape of cGAMP. STING-NPs were validated against several control formulations in several reporter cell lines, in which optimally crosslinked STING-NPs were demonstrated to be more potent than both free cGAMP and less hemolytic cGAMP formulations. This motivated further testing of STING-NPs in more representative primary immature DCs and immunosuppressive macrophages: two cell types that we expect are particularly important in the TME. STING-NPs induced repolarization to a pro-inflammatory phenotype in macrophages and maturation in DCs, suggesting that STING-NPs have the potential to both reprogram immunosuppressive elements in the TME that may be inhibiting antitumor immunity as well as to jump starting DC mediated antigen presentation for priming of an antigen specific T cell response. Collectively, these data indicate that STING-NPs are a promising immunotherapeutic for treatment of tumors, which is explored in more detail in the subsequent chapter.

Section 2.7. Materials and Methods.

Synthesis and Characterization of Block Copolymers. Butyl methacrylate (BMA), poly(ethylene glycol) 4-cyano-4-(phenylcarbonothioylthio)pentanoate, $M_n=2,000$ Da and $M_n=10,000$ Da (PEG-CPADB), 4-cyano-4-(phenylcarbonothioylthio)pentanoate (CPADB), N,N'-Dicyclohexylcarbodiimide (DCC), 4-(Dimethylamino)pyridine (DMAP), DL-Dithiothreitol (DTT), 4,4'-azobis(4-Cyanovaleric acid) (V501), dichloromethane, 1,4-dioxane, and poly(ethylene glycol) methyl ether ($M_n = 5,000$ Da) were purchased from Sigma-Aldrich. 2-(Diethylamino)ethyl methacrylate (DEAEMA) was procured from TCI Chemicals, and 2,2'-Azobis(4-methoxy-2,4-dimethylvaleronitrile) (V70) was purchased from Wako Chemicals. Pyridyl disulfide ethyl methacrylate (PDSMA) was synthesized according to a previously reported

procedure (**Appendix A.2**).⁹⁷ BHT inhibitor was removed from methacrylate monomers before further use by gravity chromatography using basic alumina (Sigma).

For synthesis of PEG-b-DB polymers, the appropriate PEG-CPADB macroRAFT chain transfer agent (mCTA) was dissolved in anhydrous dioxane with purified BMA, DEAEMA, and V501 at a 60:40 molar ratio of BMA:DEAEMA, sealed with septa, purged with N₂ for 20 minutes, and polymerized at 70°C for 18 h (**Appendix A.3**). An initiator to mCTA (I:mCTA) ratio of 0.2:1 was used with a combined monomer and mCTA to dioxane weight ratio of 0.4. Polymers were precipitated 2x in cold pentane and vacuum dried. Polymer composition were characterized via ¹H-NMR in CDCl₃ on a Bruker AV400 spectrometer (**Appendix A.4**). Molecular weight and polydispersity index were quantified using gel permeation chromatography (Agilent) with DMF containing 0.1M LiBr as the mobile phase and in line light scattering (Wyatt) and refractive index (Agilent) detectors. PEG_{5k}-CPADB or PEG_{10k}-CPADB mCTAs were synthesized as previously described (**Appendix A.5**).⁹⁸ PEG_{2k}-DBP_{4.5k} was synthesized with similar conditions, substituting V70 for V501 and a reaction temperature of 30°C for 24h.

Synthesis of 2'3'-cGAMP. 2'3'-cGAMP was synthesized using a method adapted from Gaffney *et al* (**Appendix A.6**).⁹⁹ Adenosine phosphoramidite, (1 g, 1 mmol) was dissolved in 7 mL of acetonitrile (ACN) and water (0.036 mL, 2 mmol). Pyridinium trifluoroacetate (0.231 g, 1.2 mmol) was added and the reaction mixture was stirred for 1 min. tert-butylamine (8 mL) was added and the reaction mixture was stirred for 10 min at room temperature. Solvent was removed by rotary evaporation to yield a gummy residue that was dissolved in 15 mL of dichloromethane (DCM). Sequentially, water (0.18 mL, 10 mmol,) and dichloroacetic acid (DCA, 27 mL, 3% in DCM, 10 mmol) were added and the reaction mixture was stirred at room temperature for 10 min. Pyridine

(1.6 mL, 20 mmol) was added and solvent was removed by rotary evaporation. The residue was dissolved in 10 mL of ACN and concentrated. This process was repeated three times. The oily product was dissolved in anhydrous ACN (3 mL) and a solution of guanosine phosphoramidite (1.27 g, 1.2 mmol, dissolved in 3 mL of anhydrous ACN) was added. The guanosine phosphoramidite was co-evaporated with anhydrous ACN (3 x 20 mL) and vacuum dried overnight. After stirring for 2 min, anhydrous tert-butyl hydroperoxide (5.5 M in decane, 0.55 mL, 3 mmol) was added and the reaction mixture was additionally stirred for 30 min at room temperature. NaHSO₃ (0.3 g, dissolved in 0.8 mL H₂O) was added and the mixture was stirred for 5 min. Solvent was removed by rotary evaporation. The oily product was dissolved in DCM (18 mL), and water (0.18 mL, 10 mmol) and dichloroacetic acid (DCA, 27 mL, 3% in DCM, 10 mmol). The reaction mixture was stirred for 10 min at room temperature and quenched with pyridine (10 mL). Solvent was removed by rotary evaporation and the residue was co-evaporated with anhydrous pyridine (2 x 10 mL). The oily residue was dissolved in anhydrous pyridine (17 mL) and 5,5-dimethyl-2-oxo-2-chloro-1,3,2-dioxaphosphinane (0.65 g, 3.5 mmol) was added. The reaction mixture was stirred at room temperature for 10 min and then water (0.63 mL, 35 mmol) and iodine (0.330 g, 1.3 mmol) were added sequentially. After stirring for 5 min, the reaction mixture was poured into solution of NaHSO₃ (0.2 g, in 150 mL of water). Solid NaHCO₃ (4 g) was slowly added after 5 min and the stirring was continued for 5 min. The water was transferred into a separatory funnel and a mixture of ethyl acetate and diethyl ether was added (150 mL, 1:1). The organic layer was separated and the aqueous layer was extracted with an additional mixture of ethyl acetate and diethyl ether (80 mL, 1:1). The organic layers were combined and concentrated to an oil. The residue was purified by flash chromatography (Combi-flash Rf, DCM/methanol = 0-25% for 20 min) to give a solid. The solid was dissolved in CH₃NH₂ in

anhydrous EtOH (33% by weight, 24 mL, 212 mmol). The reaction mixture was stirred at room temperature for 4 hr. The solvent was removed by rotary evaporation to give a solid. The solid was co-evaporated with a mixture of anhydrous pyridine and triethyl amine (4 times, 5 mL, 4:1) to give an oily product. The oily product was dissolved in anhydrous pyridine (2 mL) and triethyl amine (8 mL) and Et₃Nx3HF (3.3 mL, 60 mmol F⁻, 30 eq. rel to each TBS) were added simultaneously. The reaction mixture was stirred at 55°C for 3h. After the reaction mixture was cooled down, acetone (HPLC grade, 80 mL) was slowly added. The precipitate was filtered off and washed with acetone (5 x 5 mL). The final compound was purified on a Gemini–NX C18 column (250 mm × 10 mm, flow rate 5 mL/min with UV detection at 254 nm) using a gradient of 1 to 5% for 20 min (CH₃CN in 0.1 M NH₄HCO₃). ¹H-NMR spectra (**Appendix A.7**) and LC-MS data (**Appendix A.8**) of purified 2'3'-cGAMP are provided in the Supplementary Information. The biological activity of synthesized 2'3'-cGAMP, both free and incorporated into STING-NPs, was validated by comparison to a commercial source (2'3'-cGAMP VacciGrade™, Invivogen: **Appendix A.9**).

Polymer self-assembly and particle characterization. Block copolymers were mixed with ethanol to a concentration of 1250 mg/mL and allowed to equilibrate for at least 20 minutes in a 2 mL microfuge tube at 37°C. 1x volume equivalent of DI H₂O containing the encapsulant (50 mg/mL cGAMP) was added to the polymer mixture, followed by centrifugation at 2000xg for 2 minutes. The mixture was allowed to equilibrate for 20 minutes before 3x volume of 25% EtOH in H₂O was added to the mixture and centrifuged again for 2 minutes. 7.5x volume equivalents of H₂O was added to the mixture, which was briefly vortexed and sonicated at 40°C until the polymer was completely dispersed into colloidal suspension. For crosslinked PEG-b-DBP particles, the particle suspension was diluted to 1 mL and crosslinked through addition of aqueous DTT. To

purify and concentrate the particles, the sample was diluted to 15 mL in DI H₂O followed by centrifugal dialysis, twice (Amicon, 10kDa MWCO). For cGAMP loaded particles, an aliquot was removed, added to 9 volumes of pH 5.8 PBS, and analyzed by HPLC with an isocratic mobile phase of H₂O with 0.1% trifluoroacetic acid to determine cGAMP concentration.

To measure particle size distribution and zeta potential, particles were diluted into 10 mM PBS of the appropriate pH and characterized using a Malvern Nano ZS. For transmission electron microscopy, particles were drop cast onto an ultrathin carbon / lacey support grid (TedPella), stained with a 2% solution of methylamine tungstate for 30 seconds, and imaged on a 200 kV Osiris Transmission Electron Microscope.

CryoTEM samples were prepared on a Gatan Cryo Plunge III (Cp3). 3 μ L of sample (at 1 mg/mL) was dropped on a lacey copper grid coated with a continuous carbon film. The Cp3 blotter was used to remove excess sample without damaging the carbon layer prior to plunge freezing. The frozen grid was mounted on a Gatan 626 single tilt cryo-holder and a transfer workstation with liquid nitrogen was used to maintain the specimen and holder under frozen conditions prior to imaging. The sample was imaged on a JEOL 2100 FEG. The microscope was operated at 200 kV. All images were recorded on a Gatan UltraScan CCD camera.

Red blood hemolysis assay. Whole blood from de-identified patients was acquired from the Vanderbilt Technologies for Advanced Genomics (VANTAGE) core. Blood was centrifuged at 500 rcf to pellet erythrocytes, and plasma was aspirated before resuspending erythrocytes in pH 7.4 PBS. This process was repeated 3x to isolate erythrocytes which were resuspended in PBS of the appropriate pH for the hemolysis assay. Self-assembled nanoparticles were mixed with suspended erythrocytes to a concentration of 10 μ g/mL in a 96 well V-bottom plate. The plates

were incubated for 1 hour at 37°C, then centrifuged at 700 rcf to pellet erythrocytes. The supernatant was then transferred to a 96 well flat bottom plate and hemoglobin leakage was quantified by measuring absorbance at $\lambda = 575$ nm.

Cell Culture. The mouse dendritic cell line DC2.4 (H-2K^b-positive) was provided by K. Rock (University of Massachusetts Medical School) and cultured in RPMI 1640 (Gibco) supplemented with 10% fetal bovine serum (FBS; Gibco), 2 mM L-glutamine, 100 U/mL penicillin/100 μ g/mL streptomycin (Gibco), 50 μ M 2-mercaptoethanol (Gibco), 1 \times nonessential amino acids (Cellgro), and 10 mM HEPES (Invitrogen). B16-Blue ISG, THP-1-Blue ISG, and RAW-Blue ISG cells were purchased from Invivogen, and cultured according to manufacturer specifications. No authentication of the cell lines were performed by the authors. All cells lines were tested for mycoplasma contamination. All cell types were grown in a humidified atmosphere with 5% CO₂ at 37°C.

In vitro evaluation of CDN activity and cellular uptake. THP-1 ISG, DC2.4, B16 ISG and RAW Blue ISG cell lines were plated at a density of 10,000, 10,000, 50,000, and 50,000 cells/well, respectively, in a 96 well plate. Cells were treated with indicated formulations for 24 hours. For ISG reporter cell lines, the relative expression of IFN-stimulated response element (ISRE) genes was examined using the QUANTI-Blue reagent (Invivogen). For dendritic cells, secreted IFN- β was quantified with the LumiKineTM Xpress mIFN- β ELISA kit (Invivogen).

To quantify relative cellular CDN uptake, THP-1 ISG and RAW ISG cells were seeded at 100,000 cells/well in 12 well plates and treated with co-formulations of cdGMP-Dy547 (Axxora) and cGAMP for 2 hrs at concentrations of 2 ng/mL and 100 ng/mL, respectively. After incubation

for 2 hours, cells were suspended in a 2% BSA in PBS solution and analyzed *via* flow cytometry using a 561 nm excitation laser and 582/15 filter configuration on a BD LSRFortessa™.

Statistical Analysis. All statistical analyses were performed by using GraphPad Prism software, version 7.0.

Chapter 3. Evaluation of STING-NPs in Murine Tumor Models.

Section 3.1. Introduction.

Having optimized the STING-NP formulation using several *in vitro* techniques in chapter 2, the following will focus on extension of the STING-NP platform to *in vivo* applications. The vast majority of experimentation is performed in murine tumors established from the B16.F10 melanoma cell line, an immunologically cold and aggressive cell line that is both difficult to treat and prone to metastasis.¹⁰⁰ We confirm that STING-NPs are significantly more potent than equivalent doses of free cGAMP in eliciting pro-inflammatory responses in subcutaneous tumors and demonstrate that STING-NP activation in tumors triggers a broad and multifaceted phenotypic in the TME as observed through changes in magnitude of transcription of roughly 100 immunologically relevant genes. We further demonstrate that induction of pro-inflammatory gene expression extends to the TDLN, aided by rapid lymphatic trafficking of IT administered STING-NPs. This was accompanied by increased surface expression of DC maturation markers in the TME. These data suggest that STING-NPs aid in T cell priming that may normally be arrested by immunosuppressive elements in tumor bearing hosts.

Flow cytometric characterization of the TME demonstrates that tumors treated with STING-NPs experience an influx of myeloid cells and lymphocytes, which most critically include activated CD4⁺ T helper cells and CD8⁺ cytotoxic T cells. Cellular analysis of tumors treated with a fluorescent CDN analog indicate that STING-NPs are most endocytosed by macrophages, dendritic cells, and NKs, which play a critical role in initiating a subsequent *Ifnb1* driven pro-inflammatory cascade.

We demonstrate that monotherapy with STING-NPs is capable of eliciting complete rejection of large, established B16.F10 melanoma tumors. Critically, local treatment is shown to

induce a long-lived, systemic antitumor immune response through an *in situ* vaccination mechanism, highlighting the potential of this technology to combat metastases and recurrence. The treatment is shown to synergize well with ICB in mice bearing multiple tumors as well as in a model of IV STING-NP administration. Finally, we confirm that STING-NP treatment is similarly active in an *ex vivo* model of IT administration using freshly resected human metastatic melanoma tissue from two individual patients. Collectively, these experiments demonstrate that STING-NP are a powerful antitumor immunotherapeutic with translational potential.

Section 3.2. STING-NP Treatment Induces Pro-Inflammatory Gene Expression in the TME.

Subcutaneous B16.F10 melanoma tumors (~100 mm³) grown in immunocompetent mice were treated via IT injection with STING-NP, free cGAMP, or vehicle (PBS) and harvested 4h later for qPCR gene expression analysis. Compared to free cGAMP and vehicle, STING-NPs increased expression of *Ifnb1* (6.3-fold over free cGAMP), *Cxcl9* (6.6 fold) and *Cxcl10* (4.9 fold), critical mediators of antitumor T cell activation and recruitment (**Figure 3.1a**).^{101,102} Similar to previous reports, *Ifnb1* expression was highly variable at 4h,⁴⁷ likely due to tumor heterogeneity and tight temporal regulation of gene expression levels. There was a positive linear correlation between *Ifnb1* and *Cxcl9* and *Ifnb1* and *Cxcl10* levels in treated mice (**Figure 3.1b**), consistent with a STING-driven multifaceted inflammatory response.

To further investigate the kinetics of the STING driven pro-inflammatory response, interferon-mediated inflammation was further monitored through optical imaging using tumors expressing an interferon stimulated response element (ISRE) luciferase reporter that allowed for longitudinal analysis of IFN production in the TME. A single STING-NP treatment resulted in an

elevated interferon response in the tumor that persisted until at least 96h after treatment. By contrast, treatment with free cGAMP did not elicit a response above baseline (Figure 3.2).

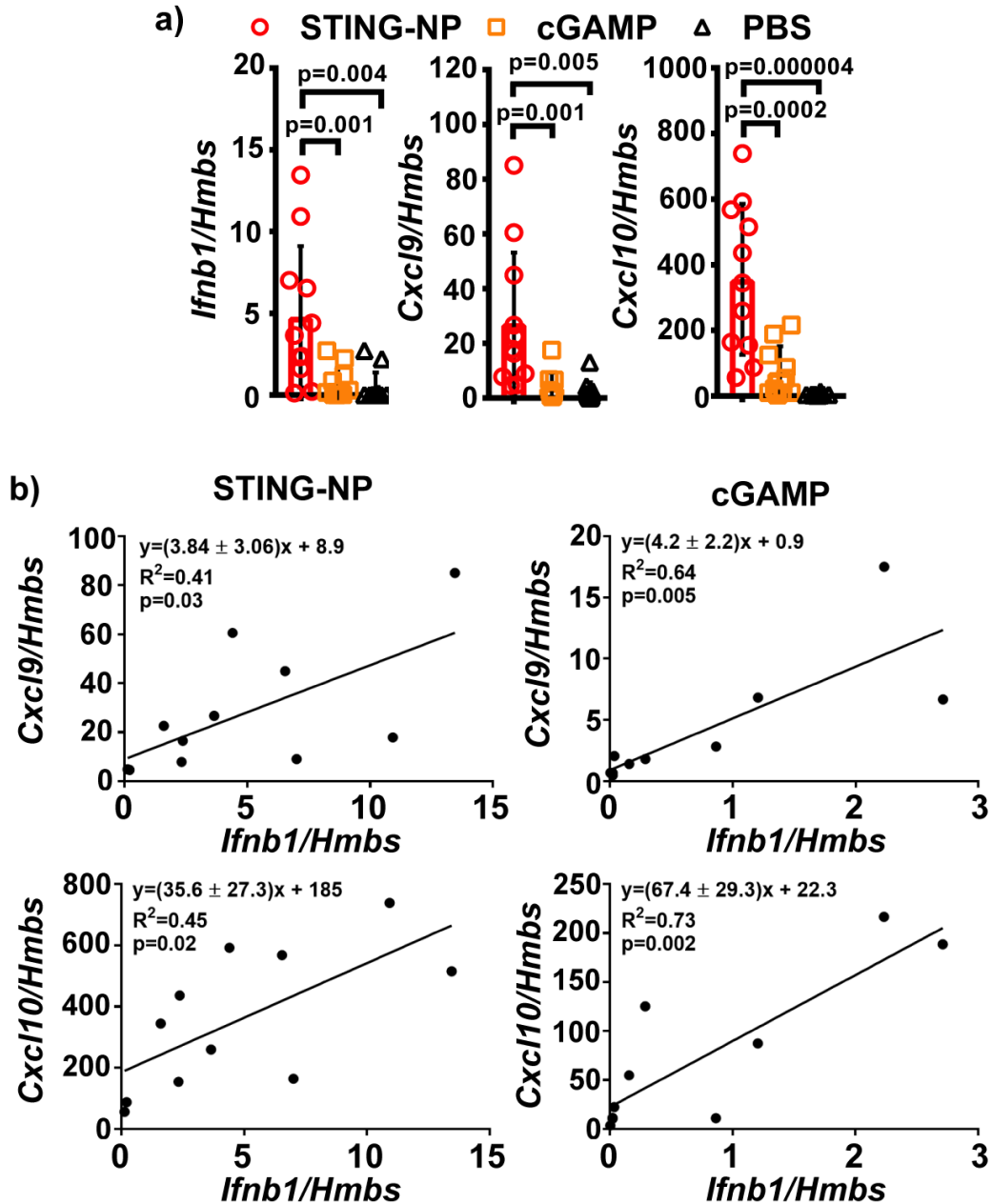


Figure 3.1 – IT STING-NP induces a pro-inflammatory and T cell recruiting gene expression profile. a) qPCR analysis of mRNA isolated from STING-NP treated B16.F10 melanoma tumors 4h after injection reveals increased IFN-I expression and increased *Cxcl9*, *Cxcl10*: T cell chemokines. b) *Cxcl9* and *cxcl10* upregulation in tumors are positively correlated with *Ifnb1* expression. p value describes the probability that the data are consistent with a non-zero fitted slope (two-tailed F test).

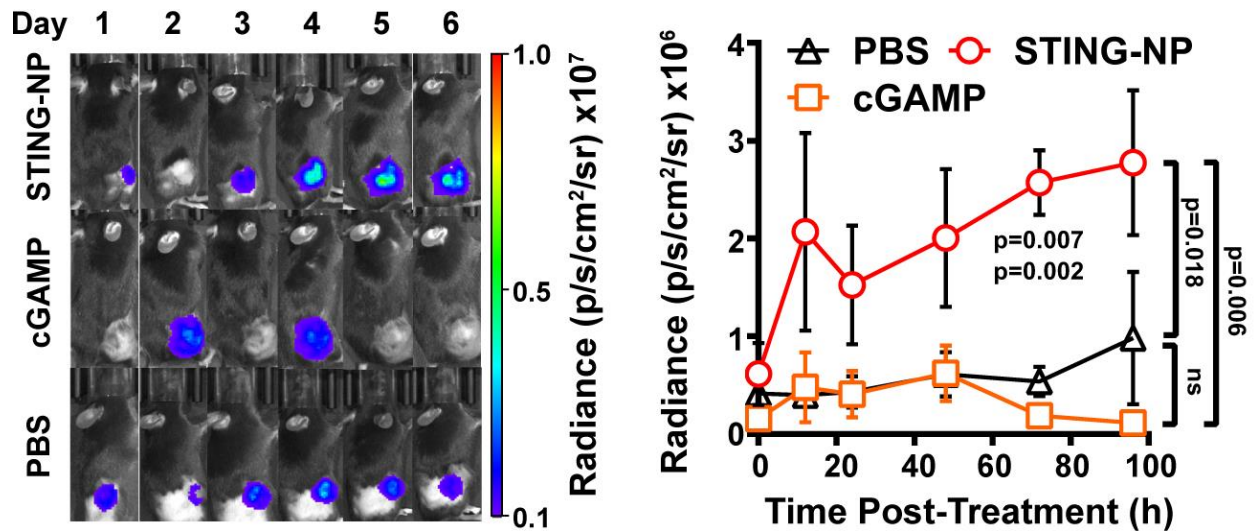


Figure 3.2 – STING-NP treatment generates sustained expression of IFN in the TME. IVIS quantification of luminescence in established B16.F10 ISRE-luc reporter cell lines. One treatment with STING-NPs increases luminescence, which is sustained until at least 96 hours after treatment. No reversion to baseline levels was seen in the examined time frame for STING-NP treated tumors. By contrast, cGAMP failed to elicit an IFN response above PBS treated controls. Data presented as mean \pm SD. Statistical test: two-way ANOVA, post-hoc Tukey Test.

For a more comprehensive view on the effects of IT STING-NP and cGAMP treatment, we harvested tumors and characterized gene expression with the nanoString Pan Cancer Immune Profiling Panel, a high throughput mRNA quantification assay that analyzes over 700 genes related to cancer immunity (**Appendix B.1**). Of analyzed genes, expression levels of *Il6* and *Ifnb1* were most significantly upregulated (~1000-fold in STING-NP treated mice) relative to vehicle controls, consistent with STING-mediated IRF3 and NF- κ B signaling. More generally, STING-NPs triggered a multifaceted shift to an inflamed and tumoricidal microenvironment, with significant upregulation of interferon-stimulated genes, pro-inflammatory cytokines, leukocyte-recruiting chemokines, pro-apoptotic mediators, genes associated with DC maturation and T-cell priming, and markers of NK and T cell activation (**Figure 3.3a**). Several immunosuppressive mediators were also upregulated, which likely act as endogenous negative regulators of STING activation.¹⁰³ Some of these genes are the targets of pharmaceuticals that are either clinically

advanced (e.g., PD-L1, IDO-1) or in development (e.g., IL-10, arg-2) and are potential candidates for combination therapy with STING-NPs. While not explored herein, an attractive feature of STING-NPs is the ability to efficiently encapsulate a diversity of cargo, offering opportunities for co-delivery of CDNs with other intracellularly active immunomodulators, which could significantly improve the therapeutic efficacy of STING-NPs in next-generation formulations.

To elucidate differences between STING-NP and cGAMP treatment, the most differentially expressed genes were ranked by the fold-change expression level between STING-NP and cGAMP treated tumors (**Figure 3.3b**). In ranked genes we observed a consistent 5-10-fold increase in gene expression in mice treated with STING-NP versus cGAMP, with the exception of *Cxcl1*, a neutrophil chemokine, (35-fold) and *Ifna2* (20-fold). In general, treatment with STING-NPs and free cGAMP elicited directionally similar changes in transcriptional profiles, suggesting a similar mechanism of action between STING-NPs and cGAMP. As such, we expect minimal off-target effects associated with administration of STING-NPs, and infer that the polymersomes are largely immunologically inert, primarily acting to enhance efficiency of cGAMP delivery. This was further corroborated by unsupervised hierarchical clustering of genes with significantly different expression levels relative to vehicle control, which revealed similar gene clusters between cGAMP and STING-NP treated tumors (**Figure 3.3c**). These data indicate that cGAMP and STING-NP induce similar phenotypic shifts in the TME, although the magnitude of change in gene expression clearly indicates that the STING-NP formulation is a far more potent stimulator of pro-inflammatory signaling than is free cGAMP.

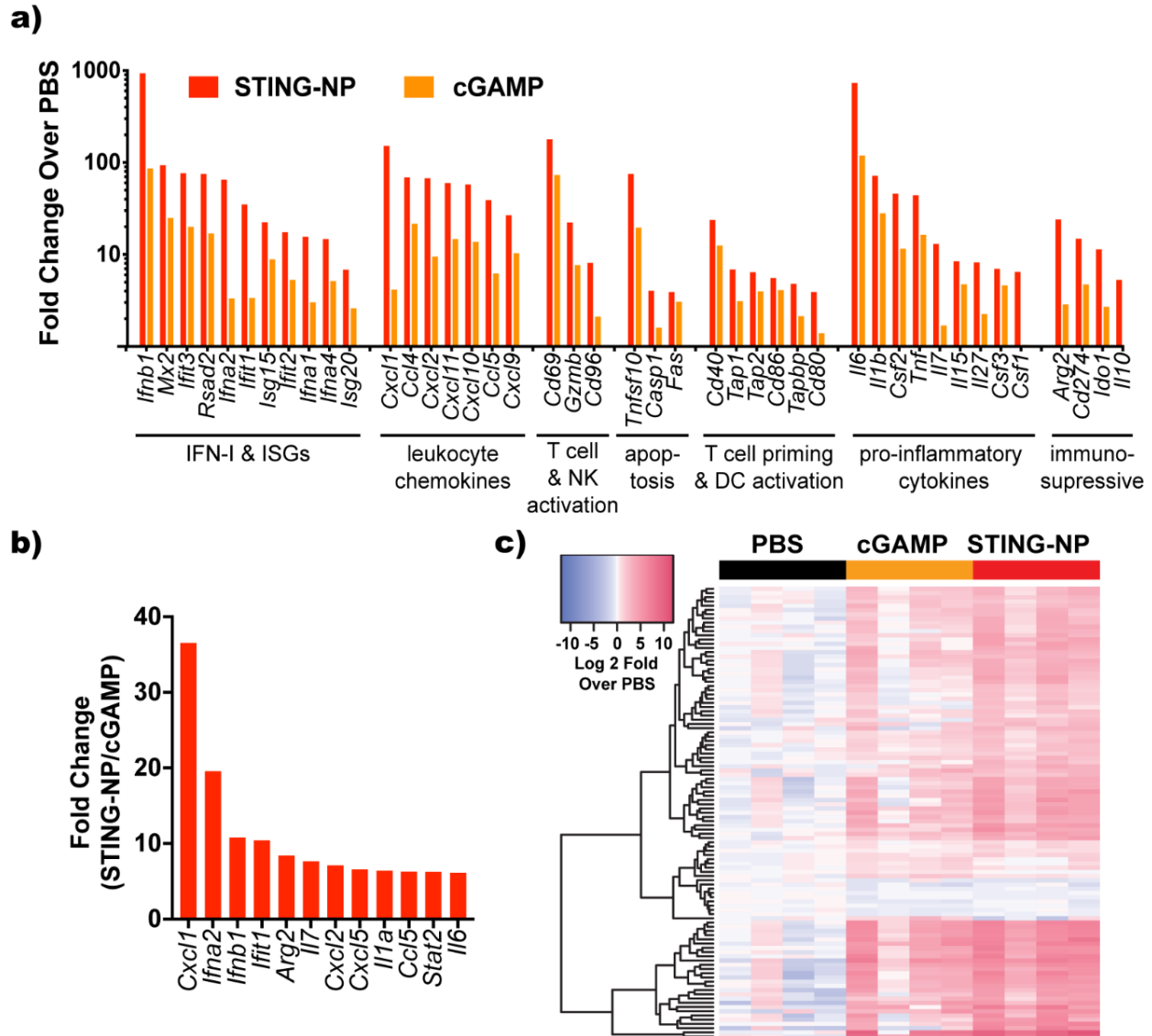


Figure 3.3 – NanoString multiplexed gene expression analysis of B16.F10 melanoma tumors. a) Selected significantly upregulated genes in cGAMP or STING-NP treated tumors as compared to PBS treated controls. b) Comparison of gene expression levels between STING-NP and cGAMP treated tumors. The 10 most differentially upregulated genes between the two are presented c) Unsupervised hierarchical clustering of significantly different gene expression profiles in cGAMP and STING-NP treated tumors relative to PBS treated controls. Data are presented as mean. Statistical test: one way ANOVA.

Section 3.3. Nanoparticle Formulation Increases Cellular Uptake of CDNs.

We next wished to interrogate the mechanism through which treatment initiates the pro-inflammatory signaling cascade, focusing in particular on identifying the primary cellular targets

of STING-NPs. B16.F10 melanoma tumors were injected with STING-NPs co-loaded with cGAMP and cyclic di-guanosine monophosphate-Dylight 547 (cdGMP-Dy547), a fluorescent CDN analog, or a mixture of soluble cGAMP and cdGMP-Dy547, and flow cytometry was used to quantify cellular uptake of cdGMP-Dy547 (**Figure 3.4a**).

cdGMP-Dy547 was most commonly localized in DCs (CD11c+MHC-II+), natural killer (NK) cells (CD45+NK1.1+), and macrophages (CD11b+F4/80+), with STING-NPs increasing the degree of CDN uptake in NK cells, DCs, and CD45- cells, with less significant increases observed in macrophages (CD11b+F4/80+) and myeloid derived suppressor cells (MDSC) (CD11b+Gr-1+), and negligible uptake of both free and encapsulated CDN by T-cells (CD3+). Amongst these cells, the highest levels of cdGMP-Dy547 were detected in NK cells, DCs, and macrophages, which we deemed to be the most active consumers of STING-NPs in the TME. (**Figure 3.4b**)

We next identified which of these cells were able to produce large quantities of IFN- β and were thus most likely to initiate the STING mediated signaling cascade in the TME. DCs (DC2.4), macrophages (RAW264.7), splenic NK cells, and B16.F10 melanoma cells were cultured *in vitro* and incubated with STING-NPs for 4 hours. qPCR analysis on RNA isolated from these cells indicated that macrophages and DCs expressed the highest levels of *Ifnb1* in response to STING-NPs, whereas lower magnitudes of gene expression were observed in B16.F10 tumor cells or NK cells (**Figure 3.4c**). Collectively, these data indicate that macrophages and DCs are the primary immunocellular targets of STING-NPs.

This finding has exciting implications relating to the translational potential of STING-NPs for use in a broad set of cancer types. It is well known that mutations in the cancer genome often lead to suppression of STING in malignant cells,¹⁰⁴ likely due to selective pressures that allow STING-suppressed cancer cells to escape immune surveillance and proliferate. Indeed, B16.F10

cells appear to only weakly express *Ifnb1* when exposed to concentrations of STING-NPs that are potent and active in other cell types. Because STING-NPs appear to induce pro-inflammatory signaling largely through host DCs and macrophages however, we expect that STING-NP treatment can be effective in a variety of tumors, rather than just the subset in which STING expression is preserved. Notably, this finding is corroborated by similar reports in the literature, which consistently find host myeloid cells and stromal cells to be the primary responders to CDN treatment.^{47,96}

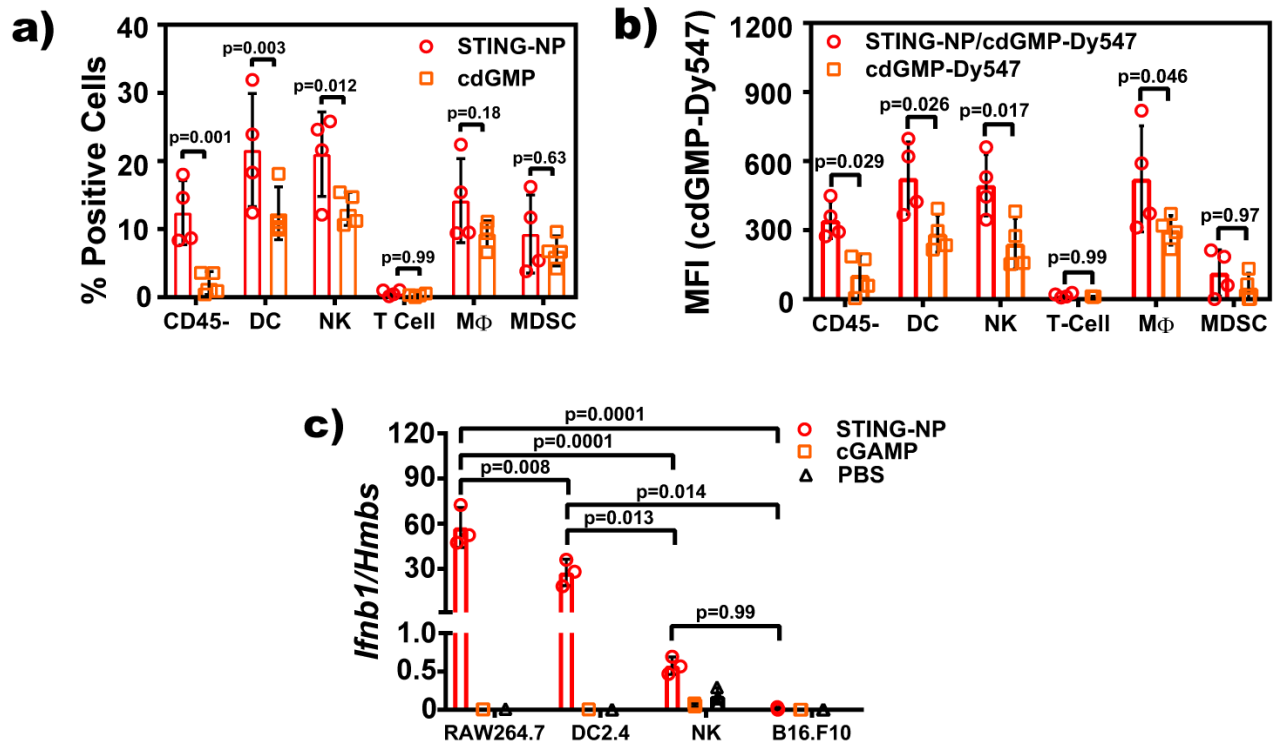


Figure 3.4 – Macrophages and DCs are the primary initiators of the immune response following STING-NP treatment. **a)** Flow cytometric quantification of cellular uptake in the TME 2h following IT injection of STING-NPs co-loaded with cdGMP-Dy547, a fluorescent CDN analog. Cells were denoted % positive if they fluoresce more brightly than analogous cells isolated from PBS treated controls. **b)** Median fluorescent intensity of cdGMP-Dy547 in analyzed cells. **c)** In vitro analysis of *Ifnb1* expression of cultured macrophages (RAW264.7), DCs, splenic NKs, and B16.F10 cells 4h after treatment with STING-NPs.

Another interesting finding in this data set relates to the relative shift in cellular uptake profiles between CDNs administered in a free or encapsulated format. While encapsulation of

cdGMP-Dy547 increased uptake in all investigated cell types except T cells, when considering the proportion of cells in which CDNs could be detected, the largest percent increase in magnitude was detected in CD45⁻ cells (~5 fold), which are largely expected to be tumor cells, as compared to roughly 1.5 to 2 fold increases for other cell types. Importantly, this did not lead to detection of high levels of CDN associated fluorescence or *Ifnb1* expression in tumor cells, indicating respectively that any individual tumor cell is likely to have taken up only a small quantity of STING-NPs and that the tumor compartment is likely relatively unimportant in contributing the the *Ifnb1* signaling cascade. Nevertheless, these data suggest that a significant portion of CDNs is likely consumed, although in low quantities on a cellular basis, by tumor cells following IT STING-NP administration.

The importance of this finding is currently unclear. Recent reports have detailed that STING dependent adjuvants appear to be capable of inducing tumor rejection in STING-deficient tumors, but have almost completely abrogated effects in models in which STING expression is knocked out in the host.⁴⁸ While this clearly demonstrates a dominant role of STING expression by the host, there remains the possibility that STING signaling in the tumor compartment may play a supportive role in the development of antitumor immunity, in which case STING-NPs could provide a critical comparative advantage over small molecule CDN drugs. For instance, STING activation in tumor cells may induce immunogenic cell death (ICD) which can aid in the T cell priming process by releasing TAAs for DC uptake or by marking tumor cells for DC uptake and cross presentation through surface of danger signals such as CRT or HMGB1.¹⁰⁵ Recently, Ahn *et al.* have reported STING and cGAS agonists located within cancerous cells can participate in *trans* activation of phagocytic cells,¹⁰⁶ providing further evidence that tumor intrinsic STING signaling may participate in the development of antitumor immunity. Notably though, ICD and

inflammatory signaling arising from direct STING activation in tumor cells is notoriously difficult to decouple from similar effects caused by stimulation of interferon- α/β receptor (IFNAR) by IFN-I originating from bystander myeloid cells in the TME. As such, the importance of increased STING-NP uptake by tumor cells is still unknown and may vary between models, although at least one study has demonstrated *in vitro* that direct STING activation induces a magnitude of ICD in B-cell lymphoma that cannot be reproduced IFN-I stimulation.¹⁰⁷ This hints that the altered cellular uptake profile by nanoparticulate CDN formulation may potentially be valuable in the development of antitumor immunity. Future work will be required to confirm this hypothesis, as well as its applicability to a broader array of cancer types.

Section 3.4. STING-NPs Traffic to the Tumor Draining Lymph Node, Facilitating Priming of T Cells.

We next sought to evaluate the effect of STING-NP treatment on the TDLN, which as discussed previously is a natural site for priming of adaptive antitumor immunity due to its proximity to the tumor, and thus, to TAAs. IT administered STING-NPs co-loaded with cdGMP-Dy547 trafficked to the inguinal TDLN, and roughly 1% of injected cdGMP-Dy547 could be detected within the TDLN 1h after injection (**Figure 3.5a**) By contrast, no Dy547 associated fluorescence could be detected in mice treated with free CDN, which was likely rapidly cleared through the vasculature following injection. While a longitudinal analysis of CDN accumulation in the TDLN was not performed, we note that TDLNs were harvested at a relatively early time point following STING-NP administration, and any observed CDN likely originates only from direct particle drainage through the lymphatics. At later time points, it is both possible and likely

that CDN will continue to traffic to the LN as STING-NP exposed DCs mature and begin the migration process, which can take days to complete (**Figure 3.5b**).¹⁰⁸

TDLNs were harvested 2h after injection for qPCR analysis, which indicated that increased lymphatic trafficking of STING-NPs was associated with increased expression of *Ifnb1* as expected. Similarly, IT administration of free cGAMP failed to stimulate *Ifnb1* above baseline expression levels. Effects of STING-NP treatment could be seen in the TDLN as far as 48h from the time of injection, as flow cytometric analysis of DCs harvested from the TDLN showed significantly more surface expression of the costimulatory marker CD86, which is both critical to T cell priming and a marker of a mature DC phenotype in what is typically an immunosuppressed environment (**Figure 3.5c**). Therefore, in addition to their capacity for potent STING activation, another important advantage of STING-NPs, and a key distinction from small molecule STING agonists, is their ability to enhance CDN uptake and STING signaling in the sentinel LN.

Section 3.5. Intratumoral Administration of STING-NP is not Associated with Onset of Long-Term Toxicological Side Effects.

While the induction of a STING driven IFN-I response may prove valuable in cancer treatment, induction of a powerful and systemic inflammatory response is not desirable. IFN-I in particular is well documented to play roles in chronic autoimmune diseases,¹⁰⁹ and may in extreme cases cause fatal septic shock like syndromes.¹¹⁰ With any immunostimulatory strategy, it is critical to establish a treatment regimen that does not induce drastic or long-lived adverse side effects. The experiments detailed in this section evaluate potential toxicological effects that may be caused by IT administration of free cGAMP or STING-NPs.

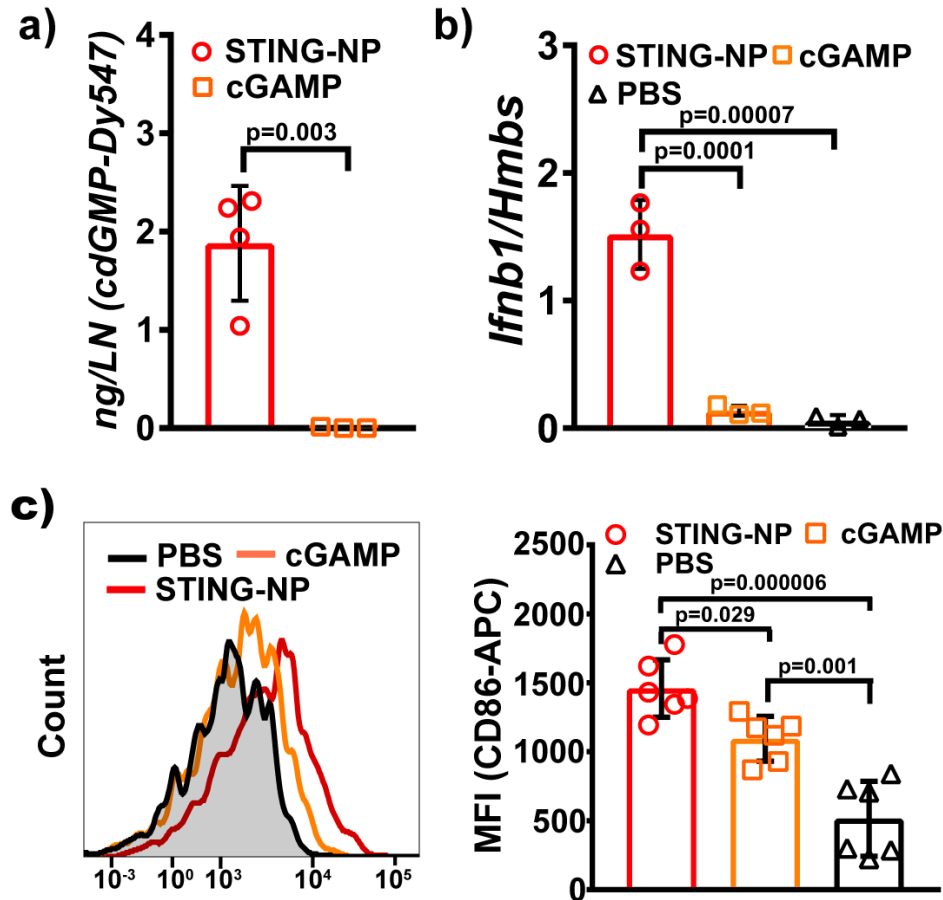


Figure 3.5. STING-NPs drain to the TDLN and induce a gene expression profile supportive for T cell priming. a) Fluorescent quantification of cd-GMP-Dy547 in the TDLN 1h following IT administration of cdGMP-dy547 either free or co-loaded in a STING-NP formulation. No cdGMP-Dy547 fluorescence could be detected above baseline in mice treated with free cdGMP. b) *Ifnb1* expression in the TDLN following IT treatment with STING-NPs or free cGAMP 4h after IT injection. c) IFN-I expression is accompanied by increased surface expression of CD86 by DCs in the TDLN 2d after IT treatment. All data are presented as mean \pm SD. Statistical test: one-way ANOVA with post-hoc Tukey test.

IT administration of STING-NPs was well tolerated with mice. Although treated mice did minor (<5% of initial state) weight loss, the effect was transient, and any weight loss was recovered within 10 days of initiation of treatment (Figure 3.6a). Potential long-term toxicological effects of STING-NPs were further examined through blood chemistry and histological analysis that focused in particular on pathology of the liver, the organ through which the majority of STING-NP clearance is expected to occur. Analysis was performed on serum proteins isolated from mice

sacrificed upon reaching tumor size endpoints. Levels of alanine aminotransferase (ALT) and bilirubin, two common indicators of liver stress, were not found to be different in a statistically significant way between any of the treated or control cohorts. While mean serum protein concentrations were within normal ranges for total bilirubin (< 1.0 mg/dL), ALT levels were found to be somewhat elevated (normal range: <30 U/L) for all treated samples, suggesting that some degree of liver stress arises in this model independently from treatment, potentially as a consequence of high tumor burden at the time of blood draw. Nevertheless, these data again reveal no clear evidence of STING-NP driven liver toxicity (**Figure 3.6b**). Additionally, serum levels of creatinine for all tested mice were found to be within <0.5 mg/dL (data not shown), well within normal ranges. While we note that these experiments are far from comprehensive, we expect from these preliminary results that STING-NPs are not likely to induce long lived kidney related toxic events.

Hematoxylin and eosin (H&E) stained liver sections revealed in mice treated IT with STING-NPs signs of hepatocellular vacuolation, a symptom associated with reversible cellular injury arising from accumulation of water, fat, or glycogen in the cell cytoplasm. All liver sections was evaluated and scored by a board certified pathologist who deemed the severity of vacuolation to be minor, though slightly above baseline, in all STING-NP treated mice. Notably, hepatocellular vacuolation was also observed in cGAMP treated mice, indicating that induction of liver pathology was not a unique consequence of STING-NP treatment. (**Figure 3.6d-f**). Taking into account the reversible nature of this pathology, these data were interpreted to reveal no clear evidence of concerning long term liver pathology following IT treatment with either STING-NPs or free cGAMP.

Section 3.6 STING-NPs Treatment Drives an Influx of Activated T-cells and Myeloid Cells into the TME.

While mRNA the quantification techniques detailed above facilitate a high throughput and holistic evaluation of gene expression in the tumor, they provide minimal insight on shifts cellular composition of the TME that may arise from STING-NP treatment. We therefore characterized the TME of treated tumors *via* flow cytometry, to attain a detailed quantification and phenotype analysis of tumor infiltrating immune cells.

A single IT treatment with STING-NPs dramatically increased the number of tumor infiltrating CD11b+Ly6c+Ly6g+SSC^{lo} activated neutrophils within two days of injection (**Figure 3.7a**). This is consistent with the substantial increase in STING-NP treated tumors of the neutrophil chemokine Cxcl1 revealed by the nanoString analysis of section 3.3. The role of these cells is somewhat unclear; while these cells have mixed legacy in analysis of tumor cell composition and have typically been associated with negative prognosis, recent and more nuanced investigations have revealed that like macrophages, neutrophils demonstrate phenotypic plasticity and may exhibit tumoricidal or protumoral effects in the TME based on immune context.^{111,112} In particular, a recent report by Lizotte *et al.* employing a conceptually similar *in situ* vaccination strategy with virus like particles implicated activated neutrophils as critical mediators of tumor rejection and development of systemic antitumor immunity here.¹¹³ A similar phenomenon may be present in STING-NP treated mice. Additionally, surface expression of CD206, a canonical marker of M2-polarized macrophages, was decreased on macrophages in STING-NP treated tumors (**Figure 3.7b**), which is suggestive repolarization or recruitment of macrophages with reduced immunosuppressive capacity. This is again consistent with *in vitro* experiments on BMDMs, demonstrating an onset of pro-inflammatory gene expression following STING engagement.

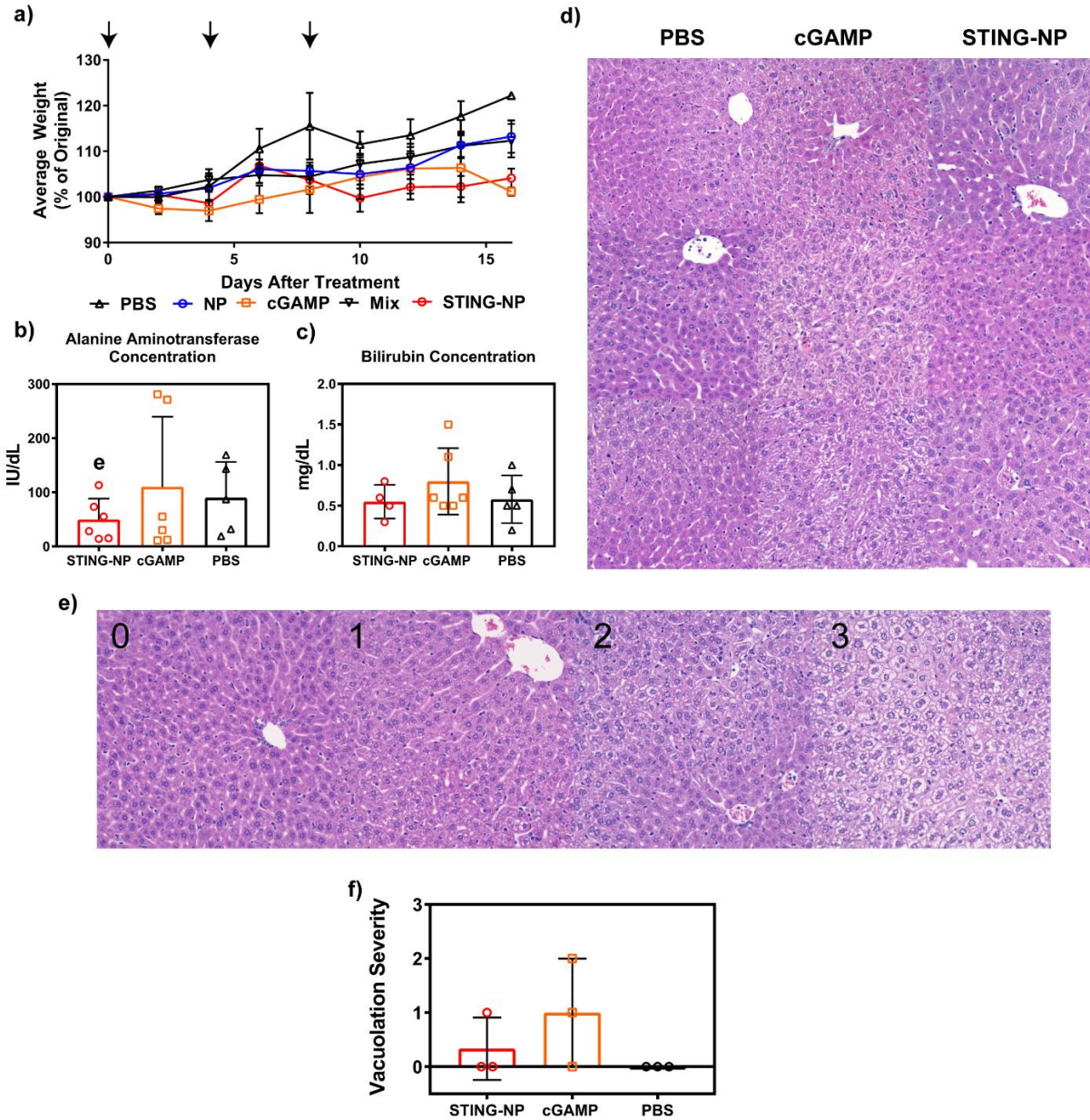


Figure 3.6. Evaluation of IT administered STING-NP and cGAMP toxicity. **a)** Longitudinal measurement of mouse body weight following IT administration of three doses of indicated formulation including 10 μ g cGAMP per dose. Arrows denote treatment dates. STING-NP treatment was associated with transient, but minor (>10% weight loss) in mice that was recovered by day 10 of the treatment regimen. **b-c)** Blood levels of alanine aminotransferase and total bilirubin. Blood was harvested when mice reached tumor size endpoints. Creatinine levels of all tested mice were below 0.5 mg/dL (not shown). **d)** Representative images H&E stained liver sections harvested at sacrificial endpoints. The most commonly observed pathology was vacuolar degeneration, a sign of reversible cell injury. The severity of vacuolation was scored from 0-3 in a masked fashion by a board-certified veterinary pathologist, guided by INHAND criteria for evaluation of the mouse hepatobiliary system and Haschek and Rousseaux's Handbook of Toxicologic Pathology, 3rd ed. This experiment was performed once and is representative of 3 biologically independent samples. **e)** Representative images demonstrating the 0-3 scaling system used for evaluation of vacuolation. **f)** Scoring of vacuolation severity for mice treated with STING-NP, cGAMP.

Both free cGAMP and STING-NPs promoted infiltration of similar numbers monocytic MDSCs (m-MDSCs, CD11b⁺Ly6C⁺) with immunosuppressive potential, likely a regulatory response to restrict STING-mediated inflammation. By contrast, only STING-NPs induced an influx of the granulocytic MDSC (g-MDSC, CD11b⁺Ly6G⁺SSC^{lo}). While these cell types are typically associated with a poor prognosis in cancer patients, we note that therapeutic studies performed in the following sections rely only on STING-NP monotherapy or combination with ICB. As such, this observation provides motivation for further combination of STING-NPs with therapeutics to block MDSC signaling that may deepen therapeutic efficacy. This strategy is well founded in the literature, in which a recent report can be found detailing synergistic activity between an antibody blocking the MDSC chemokine receptor CCR2 and STING-activating radiotherapy.¹¹⁴

Consistent of increased *Cxcl9* and *Cxcl10* expression in treated tumors, STING-NPs also significantly increased the number of infiltrating CD8⁺ and CD4⁺ T cells (**Figure 3.8a-b**). Interestingly, the recruited T-cells appeared to preferentially skew towards CD8⁺ cells, as revealed through quantification of the CD8⁺/CD4⁺ T cell ratio in the TME (**Figure 3.8c**), a commonly reported prognostic indicator of response to immunotherapy and clinical outcome.¹¹⁵⁻¹¹⁷ Additionally, intracellular antibody staining of CD4⁺ T cells indicated negligible expression of forkhead box P3 transcription factor (FoxP3), a master regulator found in the regulatory T cell phenotype.¹¹⁸ As such, we believe that CD4⁺ T cells recruited by STING-NP treatment are largely of the conventional phenotype, and are therefore expected to contribute to tumor rejection (**Figure 3.9**).

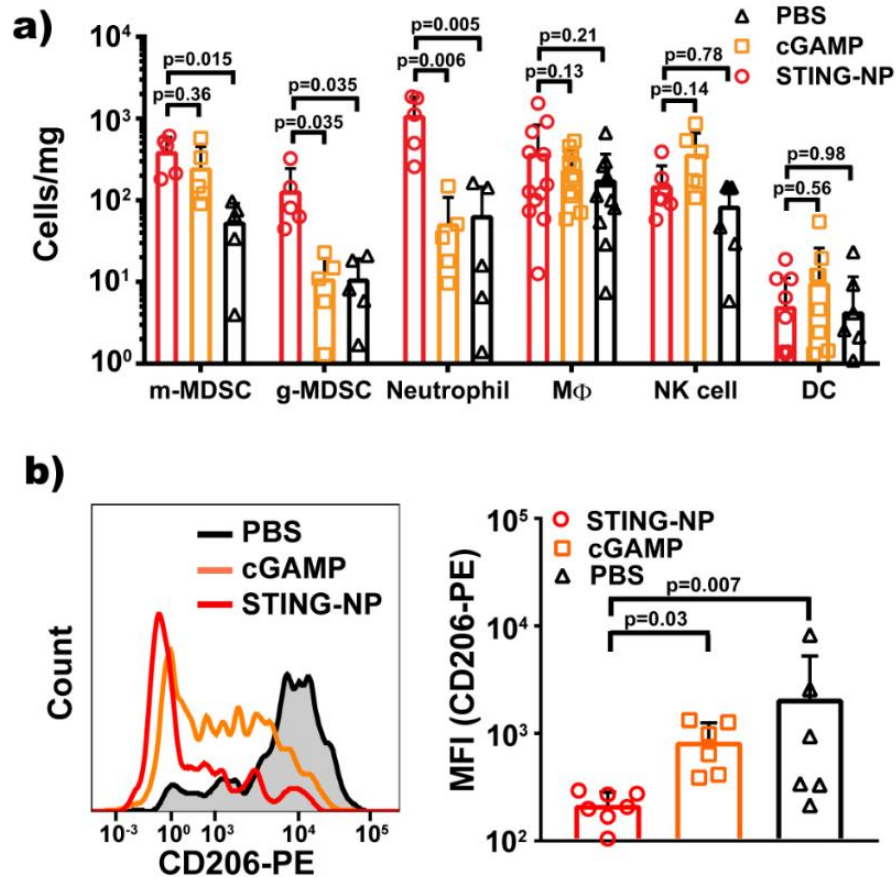


Figure 3.7. STING-NP treatment alters the myeloid cell profile in the TME. Tumors were isolated and characterized via flow cytometry 2 days after treatment. **a)** STING-NP treatment most notably induces high magnitudes of neutrophil infiltration into the TME following IT treatment. Higher numbers of m-MDSCs and g-MDSCs are also found in the TME following treatment, to a lesser extent. Macrophages, NKs, and DCs numbers are relatively unchanged. **b)** Surface expression of the M2 marker CD206 on macrophages in the TME is decreased following STING-NP treatment.

T-cell function was further evaluated using intracellular cytokine staining (ICCS). Specifically, isolated T-cells were plated *ex vivo* and stimulated with PMA and ionomycin, a drug combination that is commonly used to stimulate cytokine production through activation of intracellular protein kinases. STING-NPs significantly increased the percentage of IFN- γ and TNF- α secreting CD4⁺ T cells and TNF- α +CD8⁺ T cells in the TME relative to cGAMP, suggesting that both T cell subsets demonstrated increased cytotoxic function over those isolated from cGAMP and PBS treated controls (**Figure 3.10**). By contrast, no increased production of the

immunosuppressive cytokines IL-4 and IL-10 was observed (**Figure 3.11**), demonstrating that STING-NP treatment skews T cell phenotype in the TME towards Th1 and activated CD8+ phenotypes, rather than acting as a pan-cellular recruiter of both regulatory and conventional T cells.

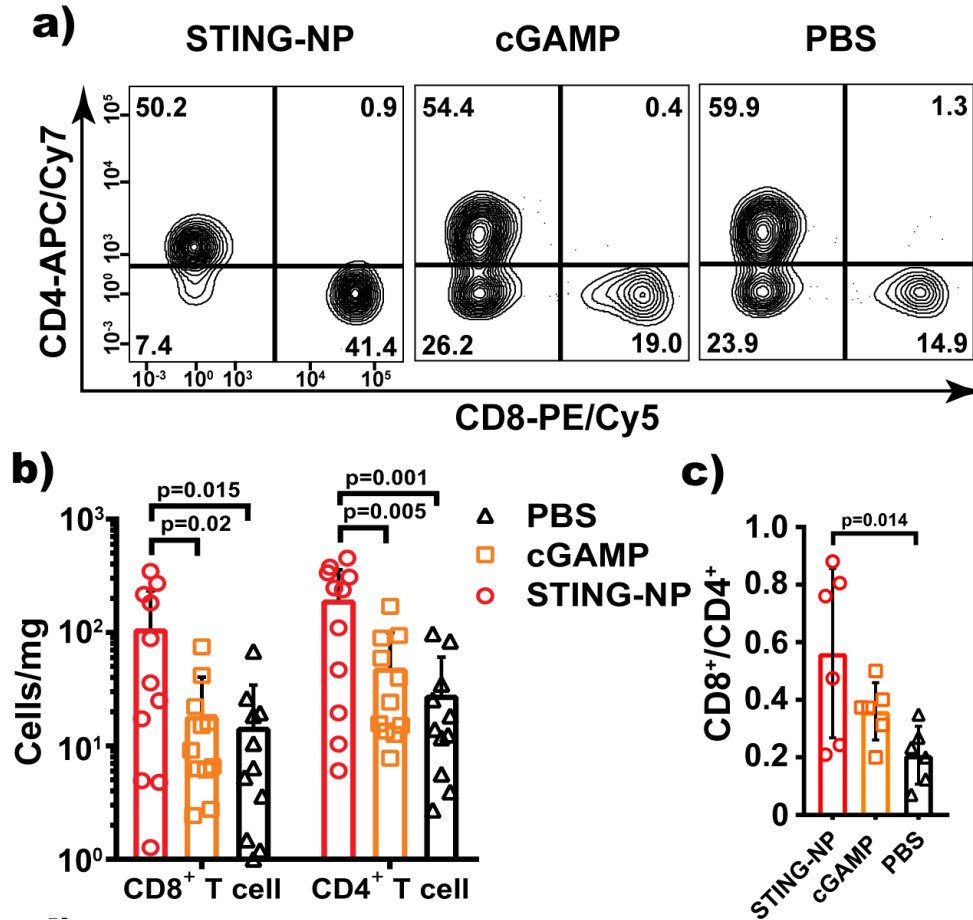


Figure 3.8. STING-NP treatment recruits cytotoxic T cells to the TME. Tumors were harvested 48h after IT injection and characterized *via* flow cytometry. **a)** Representative contour plots of cells gated on CD3⁺ T cells. STING-NP treated tumors show a skew towards CD8⁺ cytotoxic T cells relative to cGAMP and PBS treated controls. **b)** Cell counts per milligram of tumor of CD8⁺ T cells and CD4⁺ T cells are higher in STING-NP treated tumors. **c)** Consistent with **a)**, CD8/CD4, a commonly used positive prognostic indicator, ratio is higher in STING-NP treated mice, indicating that STING-NPs are strong recruiters of cytotoxic CD8⁺ T-cells.

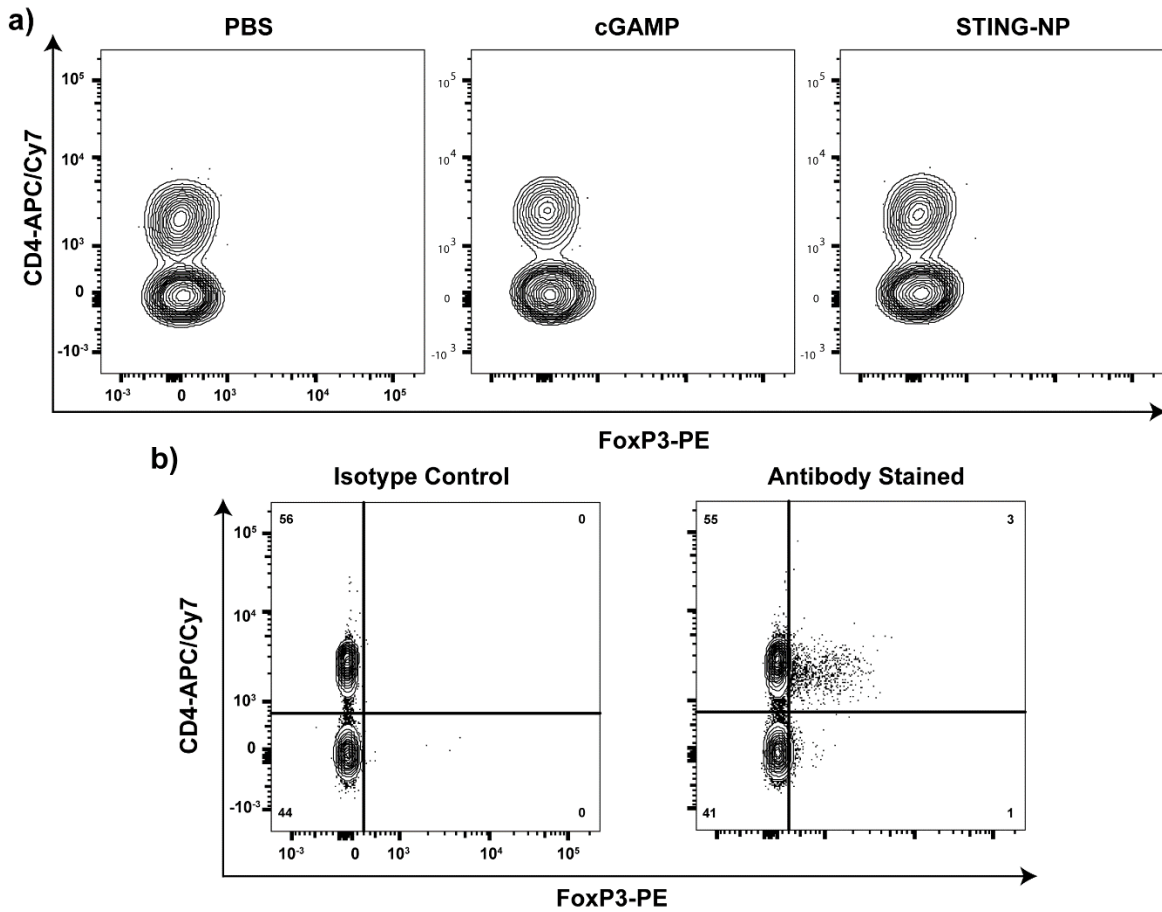


Figure 3.9. T cells recruited to the TME are not regulatory T cells. Cells were isolated 2d after STING-NP injection. All plots are gated on CD3⁺ T cells. **a)** Flow cytometric analysis of tumor infiltrating T cells. Intracellular α FoxP3 antibody revealed no regulatory T cells in any populations. **b)** Positive control: Intracellular FoxP3 staining of CD3⁺ T cells isolated from the spleen.

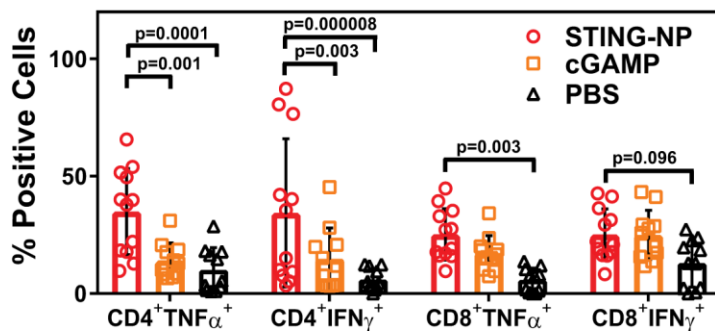


Figure 3.10. T cells in STING-NP treated tumors are of an activated, tumoricidal phenotype. Cells isolated 2d after IT treatment were plated and stimulated *ex vivo* for 4h with PMA/ionomycin and brefeldin A before analysis by flow cytometry. Both CD4⁺ and CD8⁺ T cells are capable of producing more TNF- α and IFN- γ following STING-NP treatment.

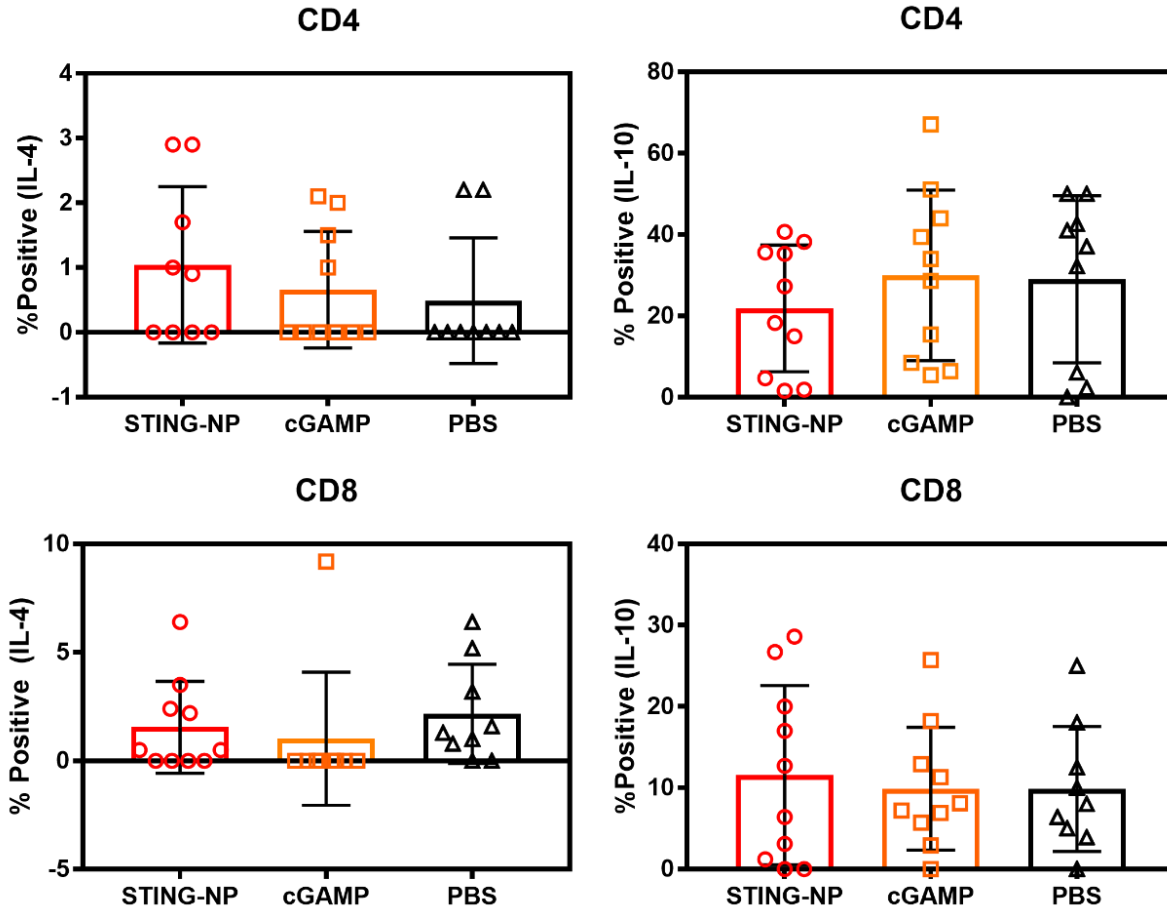


Figure 3.11 – Increased secretion of cytotoxic cytokines by T cells in the TME is not accompanied by secretion of immunosuppressive cytokines. Subcutaneous B16.F10 tumors were injected IT STING-NPs or cGAMP at doses equivalent to 10 μ g of cGAMP or PBS. Two days following treatment, tumors were harvested and prepared into single cell suspensions. Samples were stimulated with PMA/ionomycin and brefeldin A for 4h followed by ICCS for IL-10 and IL-4 and analysis by flow cytometry.

Section 3.7. *In Situ* Vaccination with STING-NPs Generates Sustained and Systemic Immune Rejection of Cancer Cells.

We first evaluated therapeutic efficacy using an IT administration route explored clinically (Figure 3.12a-e).¹¹⁹ Using a poorly immunogenic subcutaneous B16.F10 melanoma model, we initiated treatment in mice with established (~14 day) and relatively large (111 ± 16 mm³) subcutaneous tumors, which are more challenging to treat with immunotherapy than are smaller tumors, likely due to increased recruitment of immunosuppressive cell subsets by further

progressed tumors.^{120,121} Treatment with STING-NPs resulted in an eleven-fold decrease in tumor growth rate (doubling time (DT)STING-NP ~ 22.7d) and significant increase in survival time relative to cGAMP, which resulted in only a modest suppression of tumor growth (DT_{cGAMP} ~ 3.5d, DT_{PBS} ~ 2.2d) that did not confer significant survival benefit (median survival (MS)PBS = 11d, MS = 12d, MS_{STING-NP} = 29d).

Treatment with empty particles did not significantly affect tumor growth. Importantly, a physical mixture of cGAMP with pre-formulated empty vesicles yielded a nearly identical response as cGAMP, further corroborating *in vitro* data demonstrating the importance of encapsulating cGAMP into vesicles for achieving potent STING activation. Furthermore, these data further suggest that PEG_{2k}-DBP_{4.5k} polymers are largely biologically inactive in the STING-NP formulation and that therapeutic efficacy is primarily an effect of improved cGAMP delivery efficiency in the STING-NP formulation. Encapsulation of the cGAMP in STING-NPs is seen to be critical to achieving tumor rejection, consistent with previously described IFN-I quantification experiments *in vitro*.

Approximately one-third of mice treated IT with STING-NPs completely rejected tumors, without evidence of residual burden up to 65 days after tumor inoculation (Figure 4e). We rechallenged these complete responders with B16.F10 tumor cells on the opposite flank and monitored tumor volume. Without any additional treatment, 5/7 (~70%) rechallenged mice completely resisted tumor growth through at least 150 days. Tumor growth in the remaining two mice was also significantly slower relative to age-matched, treatment-naïve controls (**Figure 3.12f-g**). We therefore infer from these data that local treatment of a cancerous lesion can generate long-lasting and systemic antitumor immunity through an *in situ* vaccination mechanism,

highlighting the potential of the STING-NP formulation to improve patient responses by combating both local and metastatic recurrence after frontline treatment.

Given these exciting results, we next sought to evaluate the systemic antitumor immune response in a contralateral tumor model in which one of two subcutaneous tumors established in mice is treated locally with immunotherapy (**Figure 3.13a-c**). This experiment is complementary to rechallenge models and similarly attempts to qualify the efficacy of systemic antitumor immunity following *in situ* vaccination. Where a rechallenge model examines how long the antitumor response lived is however, the contralateral therapeutic model evaluates whether or not the primed immune response is capable of eliminating pre-established distal tumors. This constitutes a rigorous and difficult therapeutic model, as therapeutic efficacy requires generation of a T cell response than can overcome immunosuppression in the distal TME without the assistance of local STING activation.

STING-NP treatment significantly slowed the growth of non-treated, contralateral tumors relative to PBS (DT_{PBS} , ~1.9d, $DT_{\text{STING-NP}}$ ~3.0d) though to a lesser extent than the treated tumor (DT_{PBS} ~1.7d, $DT_{\text{STING-NP}}$ ~ 5.3d). These data are consistent with priming of circulating antitumor T cells by IT administration of STING-NPs, although the induced immune response appears to be incapable of rejecting preformed distal tumors without the local STING-NP administration. Tumor suppression in the distal tumor was improved through combination therapy with α PD-1 and α CTLA-4 ICB, ($DT_{\text{STING-NP+ICB}}$ ~ 5.9d), further implicating antigen specific T cells in rejection of the distal rejection. Critically, ICB, alone or in combination with free cGAMP, had no significant effect on growth of either tumor, demonstrating that potent STING engagement and subsequent T cell priming can dramatically improve responsiveness to ICB in immunologically cold tumors.

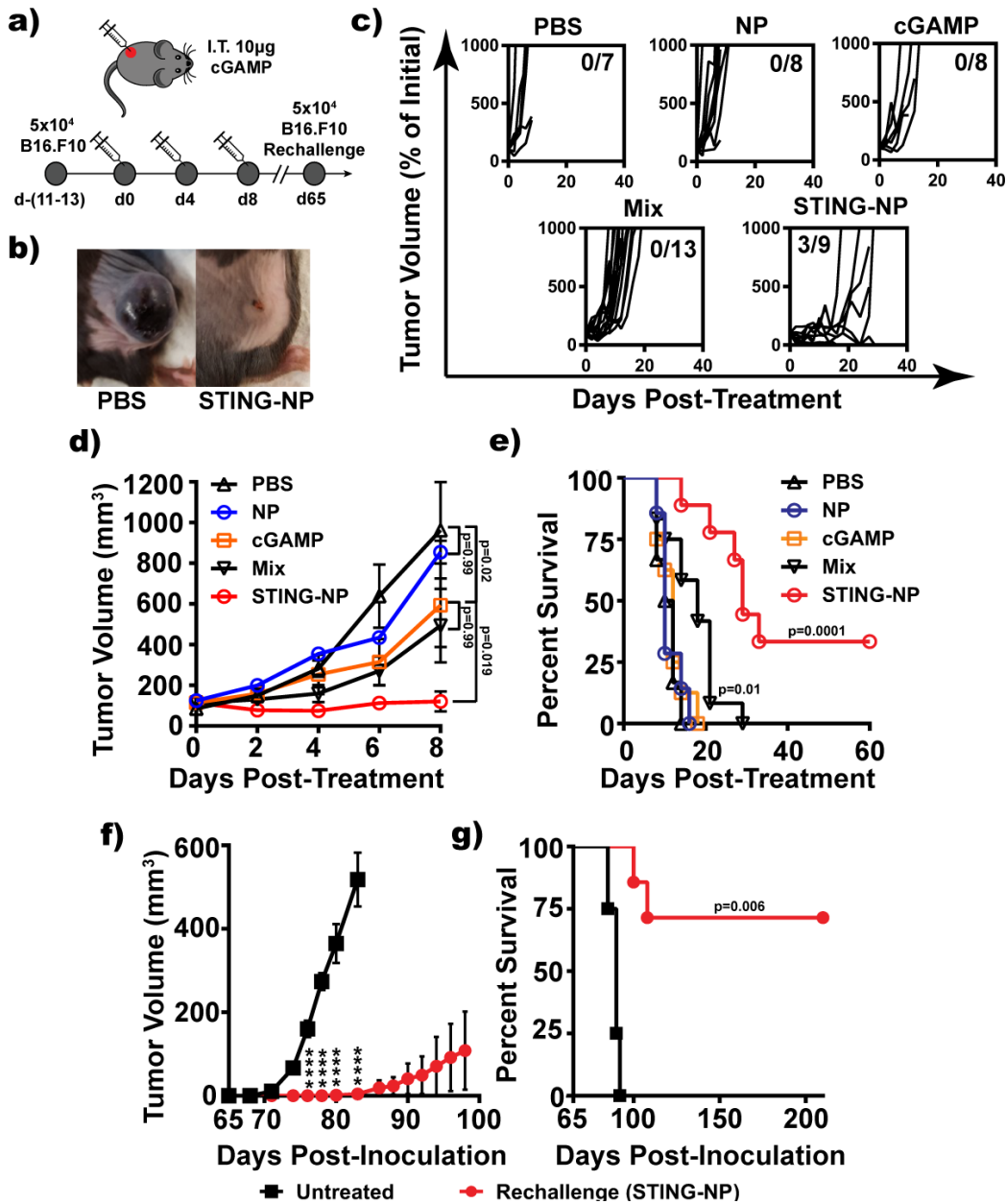


Figure 3.12. STING-NP enhance the immunotherapeutic efficacy of cGAMP and generate long-lived, systemic antitumor immunity. **a)** *In situ* vaccination and tumor rechallenge scheme for mice with a single established B16.F10 tumor. Mice with 100 mm^3 subcutaneous (SC) tumors were administered STING-NPs, free cGAMP, empty nanoparticles (NP), a physical mixture of empty NPs and cGAMP (Mix), or PBS intratumorally. **b)** Photographs of tumors 8 days after initiation of treatment. **c)** Spider plots of individual tumor growth curves with number of complete responses (CRs) denoted. **(d)** Mean tumor volume, with SEM shown. **(e)** Kaplan-Meier survival curves of mice treated with indicated formulation using 1500 mm^3 tumor volume as endpoint criteria. **f)** Mice demonstrating CRs to STING-NP treatment were rechallenged with B16.F10 cells on the contralateral flank 65 days after inoculation without any further treatment. **g)** Kaplan-Meier survival curves for treatment naïve and STING-NP treated CRs.

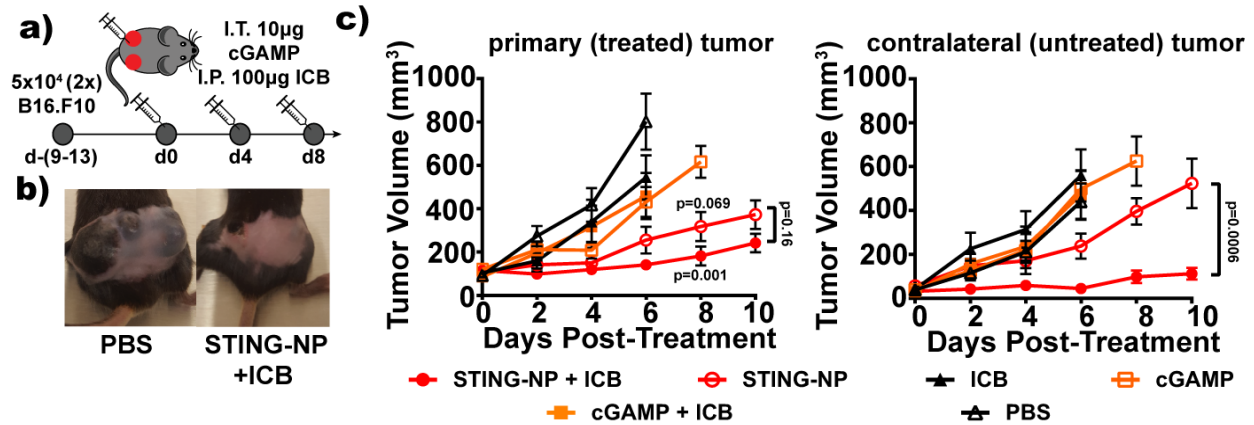


Figure 3.13. *In situ* vaccination with STING-NPs suppresses established contralateral tumor and synergizes with immune checkpoint blockade. **a)** Contralateral treatment scheme. Two tumors were established on the contralateral flanks of mice, and the larger was injected intratumorally with 10µg cGAMP formulations when combined tumor burden reached roughly 100 mm³. ICB (100µg αCTLA-4 + 100µg αPD-1) was administered intraperitoneally (IP) every four days for 3 total treatments. **b)** Representative photographs of PBS and STING-NP+ICB treated mice 8 days following initiation of treatment. **c)** Primary and contralateral tumors mean tumor growth curves. P=0.069 and p=0.001 describe STING-NP and STING-NP+ICB groups relative to cGAMP treated cohorts.

Section 3.8. STING-NPs are Effective Antitumor Immunotherapeutics when Administered Intravenously.

While localized IT delivery of STING agonists and other immunomodulators is emerging as a clinically viable treatment modality, IT this administration route may not always be feasible for many patients and/or cancer types, particularly in the setting of advanced, metastatic disease. We therefore evaluated the therapeutic efficacy of STING-NPs administered systemically via an IV route in a SC B16.F10 melanoma model (**Figure 3.14**). Systemically administered STING-NP slowed subcutaneous tumor growth relative to free cGAMP, which demonstrated no therapeutic benefit ($DT_{\text{PBS}} \sim 1.9\text{d}$, $DT_{\text{cGAMP}} \sim 1.9\text{d}$, $DT_{\text{STING-NP}} \sim 3.8\text{d}$) even when combined with ICB ($DT_{\text{cGAMP+ICB}} \sim 2.8\text{d}$). Once again, STING-NP significantly improved response to αPD-1/αCTLA-4 ICB ($DT_{\text{STING-NP+ICB}} \sim 5.0\text{d}$), presumably due to effects similar to those present in contralateral tumor models. Notably, improved responses to ICB were not observed using a mixture of empty

NPs and free cGAMP, again reinforcing the importance of efficient cGAMP encapsulation in the design of STING-NPs.

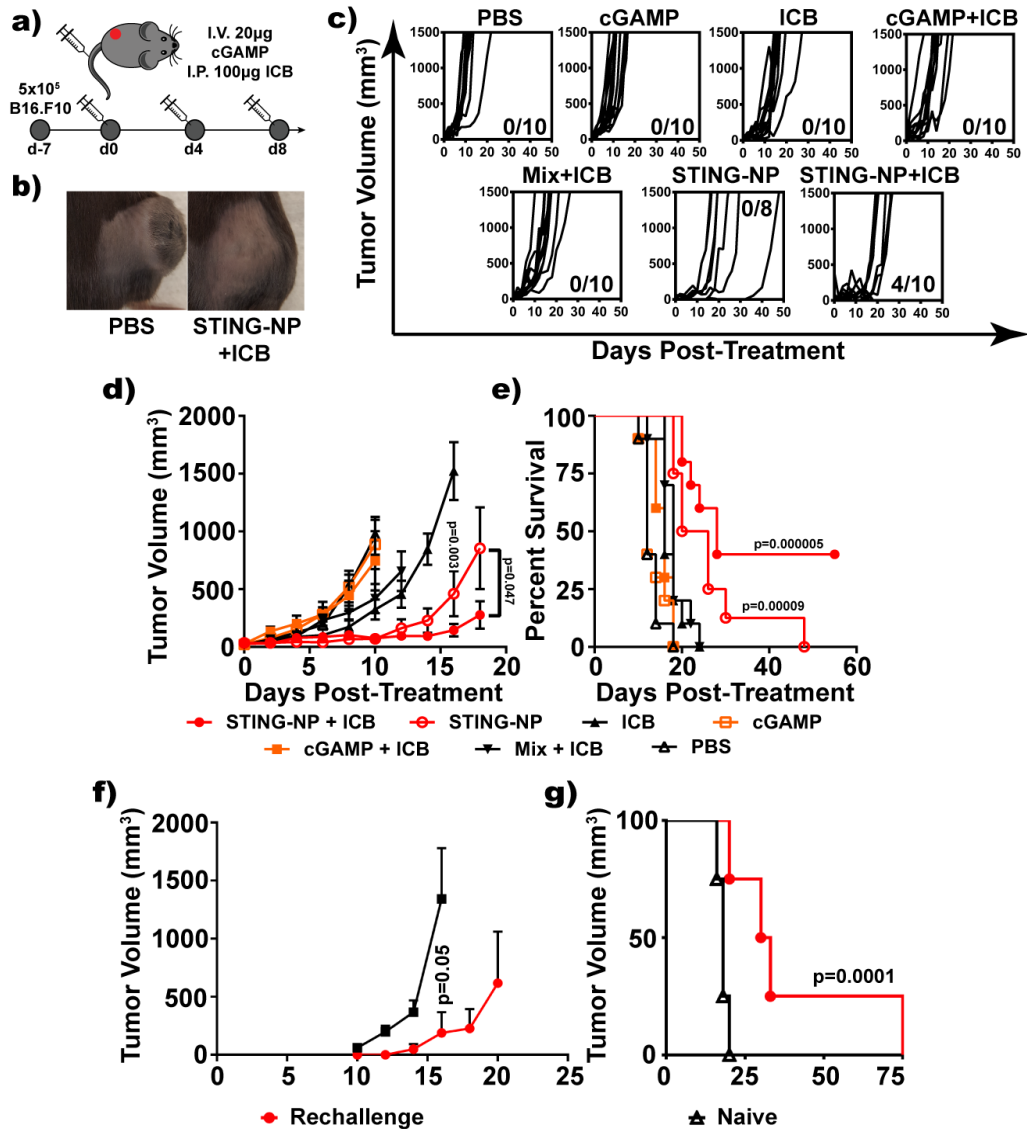


Figure 3.14. Intravenous STING-NP administration suppresses tumor growth and increases the effectiveness of ICB. **a)** Systemic treatment scheme. A subcutaneous B16.F10 tumor was established on the flank of mice. On day 7 after inoculation, mice were injected in the tail vein with 20µg cGAMP formulations. ICB (100µg αCTLA-4 + 100µg αPD-1) was administered concurrently and intraperitoneally (IP) every four days for 3 total treatments. **b)** Representative photographs of PBS and STING-NP+ICB treated mice 8 days following initiation of treatment. **c)** Spider plots of tumor growth in treated cohorts. The number of complete responders is denoted in each plot. **d)** Mean tumor growth curves. $p=0.003$ compares STING-NP and ICB treated groups. **e)** Mouse survival curves of each cohort (Mantel-Cox test). **f)** Complete responders from STING-NP+ICB treated groups were rechallenged among age matched controls, and mean tumor growth curves are shown. **g)** Survival curves of rechallenged mice and naïve controls (Mantel-Cox test).

Strikingly, 40% (4/10) of mice administered STING-NPs systemically in combination with ICB exhibited complete responses, with no evidence of tumor burden for at least 55 days after cessation of therapy. This is the first demonstration that IV administered CDN STING agonists can confer significant survival benefit while synergizing with ICB to yield complete and durable responses. However, re-challenging complete responders revealed less promising results than those achieved through local *in situ* vaccination; while all mice in the test cohort demonstrated vastly delayed tumor growth profiles to age-matched naïve controls, ultimately none of four CRs were able to completely resist tumor rechallenge. This may be due to subtle differences in magnitude of STING activation in the TME and TDLN between local and IV administration routes, but may also be due to an earlier initiation of treatment regimen in the systemic models (day 7 vs. Day 11-12). With a lower tumor burden upon initiation of treatment, T cell priming may have been relatively stunted due to a lower availability of TAA. Further investigation into this matter is merited. Nevertheless, these are promising results that highlight the potential of STING-NPs to treat tumor cells that survive standard-of-care treatment as well as unresectable metastases.

Similar to IT treatment, IV administration of STING-NPs elicited a mild acute decrease in body weight, followed by full weight recovery. Once again, no unique elevation in serum levels of ALT, bilirubin, or creatinine in mice treated with STING-NPs. Some degree of hepatocellular vacuolation was observed in all cohorts, suggesting that any observed liver stress may be inherent to the tumor model, but is not associated with STING-NP administration, either in isolation or in combination with ICB (**Figure 3.15, Figure 3.16**). Unique to the IV administration route however, was the appearance of neutrophilic infiltration in the liver following STING-NP treatment. Although this is sometimes interpreted to be symptomatic of hepatocellular damage, due to the established ability of STING-NP exposed cells to produce the neutrophil chemokine Cxcl1 in large

quantities, the significance of this phenomenon is not clear. Ultimately, all observed symptoms were generally low in severity when observed, and as such we expect IV administration of STING-NPs to be relatively well tolerated *in vivo*.

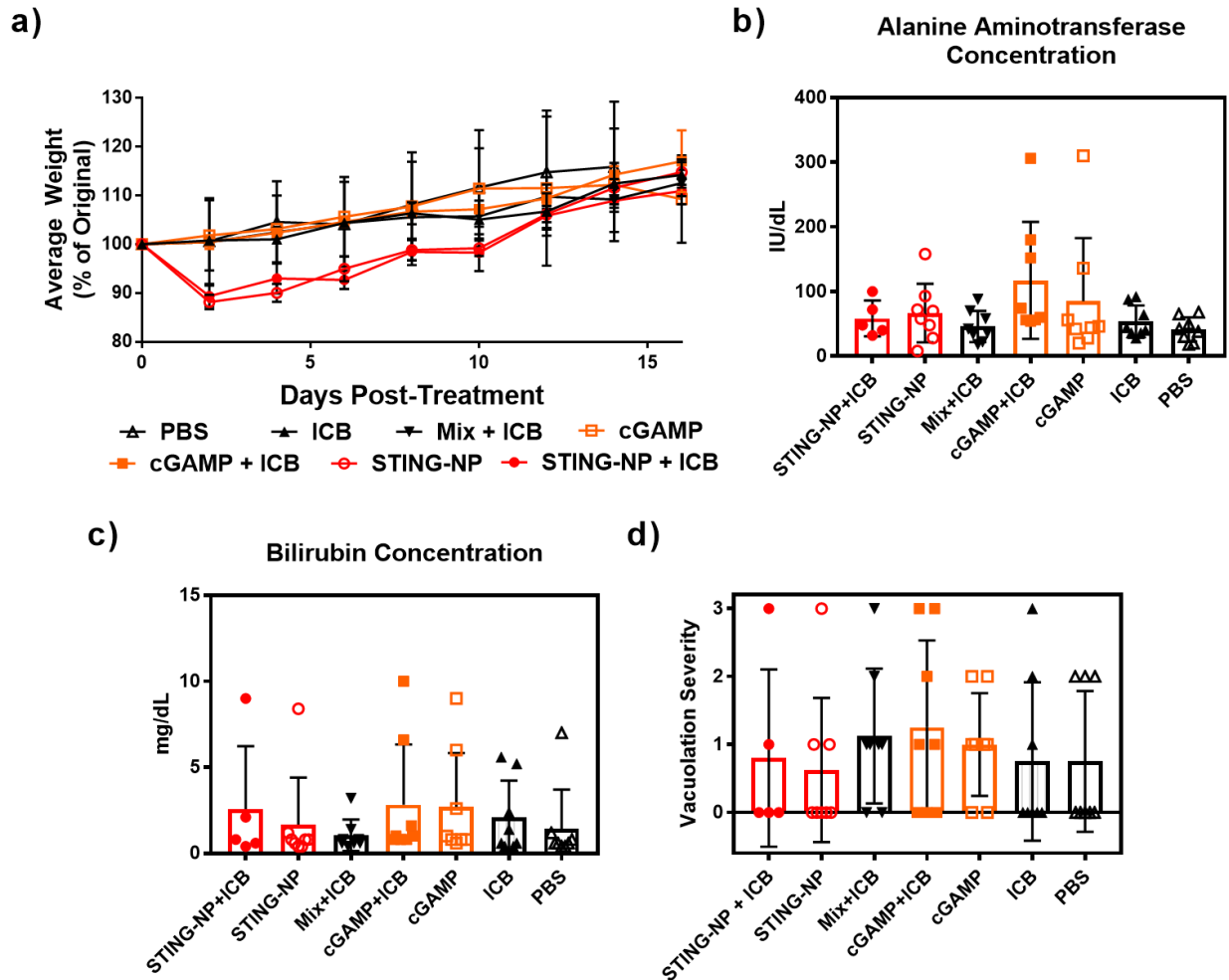


Figure 3.15. Toxicological evaluation of IV administered STING-NP and cGAMP. a) Longitudinal measurement of mouse body weight following IV administration of three doses of indicated formulation including 20 μ g cGAMP per dose. Arrows denote treatment times b-c) Blood levels of alanine aminotransferase and total bilirubin of mice. Blood was harvested when mice reached tumor size endpoints. Creatinine levels of all tested mice were below 0.5 mg/dL. For STING-NP + ICB, STING-NP, mix+ICB, cGAMP+ICB, cGAMP, ICB, and PBS. d) The severity of liver vacuolation was scored from 0-3 in a masked fashion by a board-certified veterinary pathologist as described in Figure 3.5. For STING-NP + ICB, STING-NP, mix+ICB, cGAMP+ICB, cGAMP, ICB, and PBS.

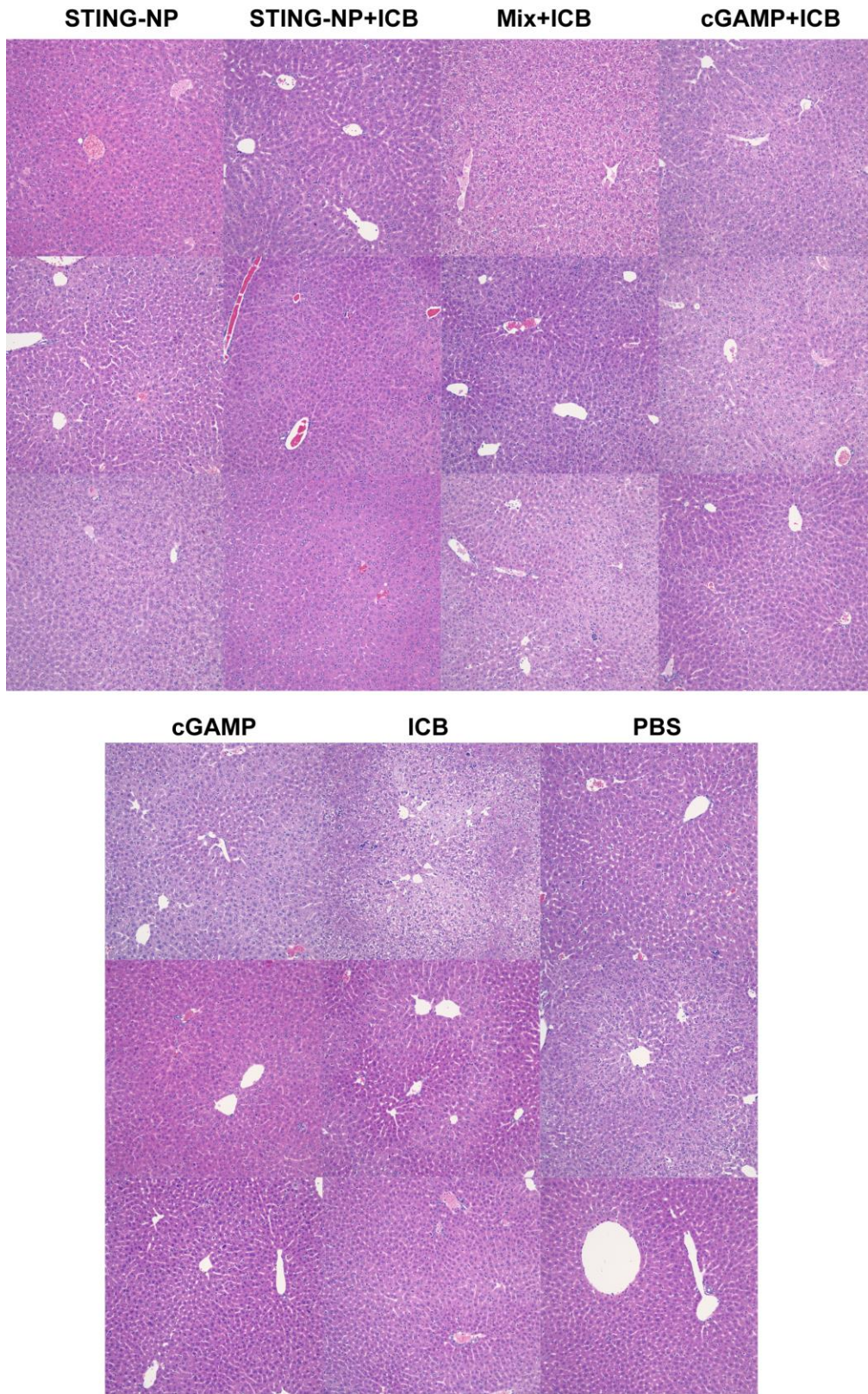


Figure 3.16. Randomly Selected H&E Stained Liver Sections. Sections were prepared from mice at tumor size determined sacrificial endpoints.

Section 3.9. Evaluation of biodistribution following systemic STING-NP administration and qPCR

While IT and IV injection of STING-NPs both demonstrate antitumor efficacy, they may effect therapeutic benefit through different mechanisms due to different pharmacokinetic profiles of STING-NPs. In particular, STING-NPs are likely primarily taken up by cells within the TME following IT administration, inducing a local pro-inflammatory program resulting in tumor cell destruction. For IV administration, STING-NPs were designed to partially comprise a PEG-shielded corona, which we expect to impart stealth properties that allow the nanoparticle to accumulate in the TME through the EPR effect. Nevertheless, the EPR effect is well known to be relatively weak,¹²² and thus nanoparticles administered IV are likely to largely accumulate elsewhere. Here we evaluate the biodistribution of STING-NPs as a first step to understanding how they affect antitumor immunity.

PEG_{2k}-DBP_{4.5k} was labeled with a near-infrared (NIR) fluorescent tag by reduction of PDS moieties to free thiols for use in thiol-maleimide click chemistry (**Appendix B.2**). Labeled polymers were then dried and blended in a 1:9 ratio with unlabeled polymer and used to formulate STING-NPs for injection and subsequent quantification of organ level biodistribution (**Figure 3.17**). Despite PEG shielding, the majority of STING-NPs accumulates in the liver, with lower quantities found in the TDLN, spleen, and kidney. This method of nanoparticle quantification showed no observable nanoparticle uptake in either the lungs, or critically, the tumor, suggesting that direct activation of STING within the TME may be less of a contributing factor to tumor suppression with the IV administration route. Of the evaluated organs, the TDLN is perhaps the most interesting of the observed organs due to its potential role as a site of antigen specific T cell priming. Given the detection of relatively high quantities of STING-NPs in the TDLN, IV STING-

NP administration is likely induce APC maturation and facilitate T-cell priming in a mechanism that is similar to analogous effects associated with IT therapy. The spleen, as a lymphoid organ, is also of interest for similar reasons. Interestingly, the spleen in particular has been implicated as a site of tumor cell tolerogenesis. Ugel *et al.* have reported that splenic MDSCs, a subset of which are likely DC progenitors, may cross-present TAA to CD8⁺ T cells.¹²³ Without proper co-stimulation and pro-inflammatory context, these exposed T cells differentiate into a tolerogenic phenotype, abrogating their cytotoxic function. Furthermore, Wu *et al.* have recently demonstrated that the spleen houses progenitor cells that are often primed for differentiation into immunosuppressive MDSCs in TMEs in tumor bearing mice.¹²⁴ Given the well-documented effect of pro-inflammatory signaling to induce MDSC differentiation and maturation, these data suggest that activation of STING in the spleen and associated pro-inflammatory signaling may be a critical facet of IV STING-NP administration.

STING-NP accumulation in the hepatic and renal compartments are likely a simple consequence of particle uptake and clearance. As expected for nanoparticles of this size, the majority of particles appear to be cleared by the liver associated RES system. Renal ultrafiltration of nanoparticles appears to be a significantly weaker effect, as expected, due to small pore size cutoff in in the vascular endothelium. The magnitude of STING-NP accumulation in the liver however, is ultimately quite striking, and suggests that the vast majority of administered STING-NPs may be eliminated without contributing to antitumor immunity. While not explored herein, the efficacy of STING-NPs may benefit from further particle optimization to minimize phagocytic particle clearance.

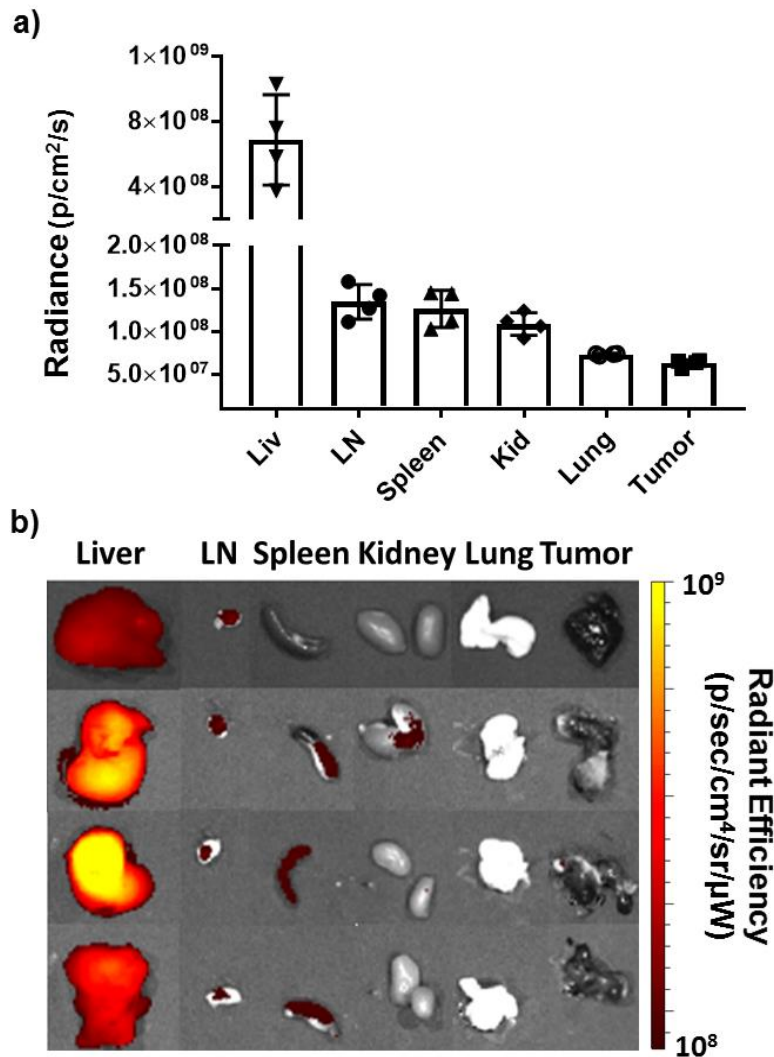


Figure 3.17. STING-NPs largely accumulate in the liver with lesser but significant accumulation in lymphoid organs. 20 μg of VivoTag-750 labeled STING-NPs were injected into the tail vein of mouse. 24h later, organs were harvested for IVIS fluorescent imaging. **a)** Mean fluorescent radiance of each characterized organ. LN denotes the tumor draining lymph node. **b)** Representative overlaid conventional and fluorescent photographs of each organ. Data are presented as mean ± SD.

The apparent lack of particle accumulation in the tumor was suggestive that IV STING-NP administration may not directly activate STING in the TME. To test this, tumor bearing mice were once again treated IV with STING-NPs, and tissues of interest were harvested for characterization via qPCR (**Figure 3.18**).

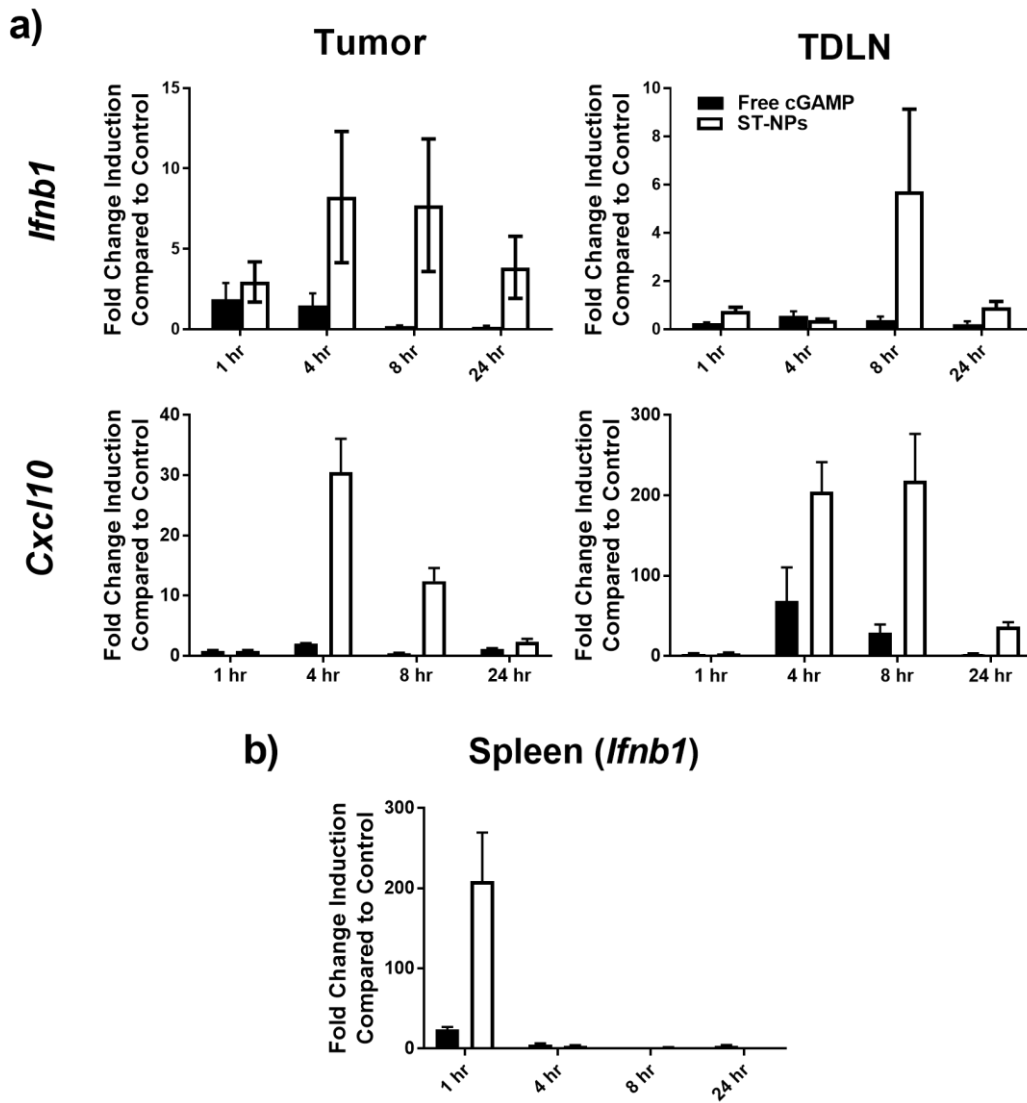


Figure 3.18. Longitudinal analysis of proinflammatory gene expression in the tumor and lymphoid organs in IV treated mice. Tumor bearing mice were treated through the tail vein with 20 μ g of cGAMP, free or formulated into STING-NPs. mRNA was harvested from sacrificed mice at each time point and quantified *via* qPCR. **a)** *Ifnb1* and *Cxcl10* expression normalized to a control cohort treated with PBS. **b)** *Ifnb1* expression in the spleen with the same normalization method. Data are presented as mean \pm SD.

These experiments revealed that pro-inflammatory pathways were indeed upregulated in the TME in STING-NP treated mice, despite lack of evidence of particle uptake as measured by fluorescent measurement of labeled particle trafficking, although to a far lesser intensity than was measured with IT injection of a lower dose (10 μ g) of STING-NPs. This disparity was likely due in part to exposure of cells in the TME to pro-inflammatory cytokines secreted by STING-NP

exposed cells. In particular IFN-I produced by circulating or splenic myeloid cells is likely to have easy access to the tumor vasculature, which would induce *Ifnb1* and associated *Cxcl10* expression through stimulation of the interferon-alpha/beta receptor (IFNAR). A second potential explanation for the observed pro-inflammatory signaling in the TME is simply that IVIS was not well suited for quantification of STING-NPs in the melanin rich tumor, which absorbs light far more strongly than other tested organs. Both of these mechanisms are likely at work here, and will be revisited in the following section.

As expected accumulation of STING-NPs in the TDLN is accompanied by upregulation of *Ifnb1* and *Cxcl10*. Although *Cxcl10* was not quantified in the spleen, *Ifnb1* expression levels suggest that STING is similarly activated in both lymphoid. Interestingly, the kinetics of *Ifnb1* expression appear to be offset by several hours between the spleen and TDLN, which suggests, intuitively, that STING-NPs have immediate access to the spleen following IV administration, but may rely on slower trafficking mechanisms such as cellular uptake and migration to the LN or accumulation in the TME followed by direct draining to the lymphatic system. Regardless, these data demonstrate that IV administration of STING-NPs stimulates the TME, TDLN, and spleen, three sites that we expect to be critical in the modulation of antitumor immunity.

Section 3.10 – Cellular Uptake of STING-NPs in the Tumor and Lymphoid Organs.

We next used flow cytometric analysis on tumors and lymphoid organs to analyze particle uptake on a cellular level (**Figure 3.17**). This strategy is complementary to experiments designed to characterize organ level biodistribution and, similar to analogous experiments performed in the case of IT injection in section 3.4, allows us to find the primary consumers of STING-NPs, implicating those cells in the initiation of the immune response.

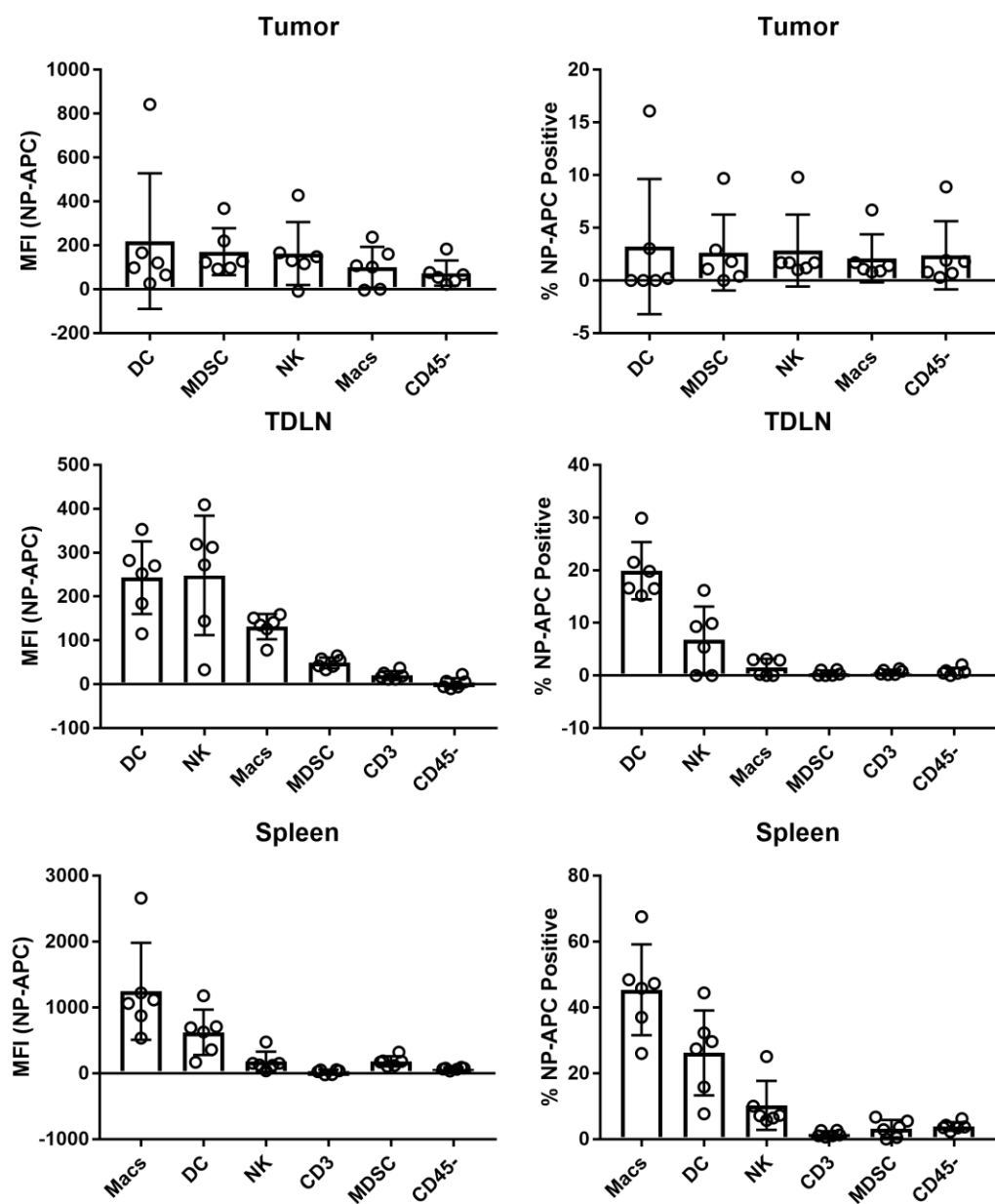


Figure 3.19. Flow cytometric analysis of STING-NP accumulation in cells found in the tumor and lymphoid organs. Mice were treated IV with 20 μ g of cGAMP encapsulated within dye labeled STING-NPs. 24h after injection, tissues were harvested and analyzed *via* flow cytometry. Left column represents geometric mean fluorescent intensity of all gated cells, with baseline fluorescence of a PBS treated control cohort subtracted. Right column represents percentage of gated cells that demonstrated STING-NP associated fluorescence above the control cohort. Data are presented as mean \pm SD.

Cellular uptake profiles were in general, largely consistent with IT experiments, with DCs, NKs, and macrophages taking up the largest amount of particles in lymphoid organs, with minimal

uptake in non-myeloid cells. Interestingly, STING-NPs could indeed be found within the tumor, in seeming contrast to IVIS measured fluorescence data. This suggests high optical density of the tumor tissue may indeed have blocked measurement of accumulating polymer, an effect that may have been exacerbated by the comparatively low levels of cellular uptake in the tumor versus in lymphoid organs that are revealed by flow cytometry. This effect is mitigated following preparation of the sample for cytometric analysis, which involves digesting the tissue for preparation of a single cell suspension and may explain the discrepancy between the two data sets.

An intriguing discrepancy between the cases of IV and IT administration arises however when examining the cellular uptake profile in the tumor compartment, which reveals a relatively flat uptake profile in myeloid cells, including MDSCs. By contrast, IT administration resulted in large amounts of uptake by DCs, macrophages, and NK cells, while MDSCs appeared to be somewhat passive bystanders in reacting to STING-NPs. One possible explanation for this flattened uptake profile could be weaker STING activation in the TME in the case of IV administration. A strongly stimulated, inflamed TME may be sufficient to cause differentiation of STING-NP exposed MDSCs into mature cells, causing a downward bias of CDN associated fluorescence in MDSCs for tumors treated IT with STING-NPs. Analogous signaling may be insufficient without accumulation of higher quantities of STING-NPs in the TME for the case of IV administration. Alternatively, increased relative MDSC uptake is also consistent with a myeloid cell migration mechanism in which MDSCs from the vasculature or spleen come into contact with STING-NPs and then subsequently traffic to the TME, which is well known to recruit MDSCs from the periphery.¹²⁵ This would be consistent with a report by Smith *et al.* detailing efficient tumor accumulation of fluorescent nanotubes following their uptake by circulating MDSCs that are gradually recruited to the TME.¹²⁶ Ultimately, STING-NP accumulation in the TME is likely

due to a combination of active (cell migration) and passive (EPR) mechanisms, and as such it is likely that some amount of the observed *Ifnb1* and *Cxcl10* upregulation in the TME is due to direct STING activation in the TME.

Comparison of the lymphoid organs yields a second interesting data set; splenic macrophages, and to a lesser extent DCs, play a dominant role in particle uptake in the splenic environment. In the TDLN, the roles are reversed, with a very small percentage of macrophages (0-3%) showing any STING-NP associated fluorescence at all. This is once again consistent with a model of active targeting *via* cell migration; IV administered STING-NPs have direct access to the spleen through the vasculature, and are thus taken up in large part by highly phagocytic splenic macrophages. In stark contrast, IV administered STING-NPs do not have a clear line of site to the TDLN; given their size, they are unlikely to escape from the vasculature without first being subject to cellular uptake or by exploiting vascular defects in the tumor vicinity. For passive targeting of the TDLN, STING-NPs would most likely first have to accumulate within the TME, and then drain through the lymphatic system, which seems unlikely due to the relatively low amount of STING-NPs observed in the tumor through both IVIS and flow cytometric methods. Instead, the majority of STING-NPs in the TDLN may accumulate through uptake by circulating DC and DC precursors, which then migrate to the TDLN following STING induced maturation. This mechanism would be consistent with both the high relative uptake in the TDLN versus the tumor, as well as the relative dominance of potentially migratory DCs in the TDLN in uptake of STING-NPs.

In summary, analysis of STING-NPs reveals a likely suboptimal biodistribution for therapeutic efficacy. In particular, the majority of administered treatment appears to accumulate in the liver, which is not expected to contribute in a meaningful way to tumor rejection. More

excitingly, STING-NPs accumulate well in lymphoid organs, where they likely play a role in overcoming tumor induced immunosuppression to improve T-cell priming. Accumulation in the TME was observed, although in limited quantities, likely leading to much lower magnitudes of *Ifnb1* and *Cxcl10* expression than was induced in the case of IT STING-NP administration. Nevertheless, this should not overshadow the topline result that IV STING-NP treatment, administered in combination with ICB, was capable mediating complete rejection of B16.F10 melanoma in 4/10 of treated mice. Currently observed STING-NP biodistribution profiles are clearly capable of inducing effective antitumor immunity, demonstrating the promise of this therapeutic platform. These data furthermore suggest that therapeutic efficacy may be greatly improved through additional particle engineering for more controlled targeting of the STING-NP particle.

Section 3.11. STING-NPs Stimulate Pro-Inflammatory Signaling in Resected Human Melanoma.

The data reported above clearly demonstrate that STING-NPs have antitumor therapeutic activity in B16.F10 murine melanomas. However, one of the main bottlenecks in translation to the clinic is differential activity of drugs between mouse models and human patients. Roughly 90% of novel drugs fail between in clinical trials despite promising pre-clinical data.¹²⁷ In a particularly relevant case, this was the case for a synthetic STING agonist, 5,6-dimethylxanthene-4-acetic acid (DMXAA), which demonstrated potent antitumor behavior through stimulation of IFN-I and TNF- α to mediate disruption of the tumor vasculature.⁴⁴ Despite generating excitement due to its potency in mouse models, DMXAA ultimately failed in phase III trials, likely due to its inability to stimulate human versus murine STING.¹²⁸

While a similar failure mechanism is not expected for STING-NPs due to its use of endogenous cGAMP as an active drug, we sought to validate the translational potential of STING-NPs through testing on human tumor samples. Freshly resected human metastatic melanoma tissue were injected intratumorally *ex vivo* with STING-NP, cGAMP, or PBS before characterization via qPCR (**Figure 3.20**). Consistent with findings in murine models, STING-NPs demonstrated superior immunostimulatory activity, increasing expression of *Ifnb1* (48-352 fold) and *Tnf* (4-5 fold) as well as *Cxcl10* (15-23 fold), a chemokine that correlates with T cell infiltration in human metastatic melanoma. This effect was consistent in tumors from two different melanoma patients. These data are relatively preliminary, as the *ex vivo* experimental design abrogates any effects of STING-NPs treatment to mediate cell recruitment, whether tumoricidal or pro-inflammatory, and fails to monitor the rate of tumor growth following treatment. Nevertheless these data suggest that STING-NPs has potential to demonstrate similar antitumor efficacy in human melanoma.

Section 3.12. Methods.

Mouse Care and Experimentation. Female C57BL/6 mice (6-8 weeks old) were purchased from The Jackson Laboratory (Bar Harbor, ME) and maintained at the animal facilities of Vanderbilt University Medical Center under conventional conditions. All animal experiments were approved by the Vanderbilt University Institutional Animal Care and Use Committee (IACUC).

IVIS Imaging. B16.F10 melanoma cells were transduced to express luciferase in an ISRE-dependent manner via the Cignal Lenti Reporter construct (Qiagen), per the manufacturer's instructions. Briefly, B16.F10 cells were plated and allowed to adhere before being transduced with the lentiviral particles at a multiplicity of infection (MOI) of 10 in the presence of 2 $\mu\text{g/mL}$

SureENTRY Transduction Reagent (Qiagen) and incubated overnight. Transduced cells were grown and expanded in medium containing the selection agent puromycin at a concentration of 10 $\mu\text{g}/\text{mL}$. Transduction was verified by treating cells with mouse IFN- β and monitoring luciferase production over time.

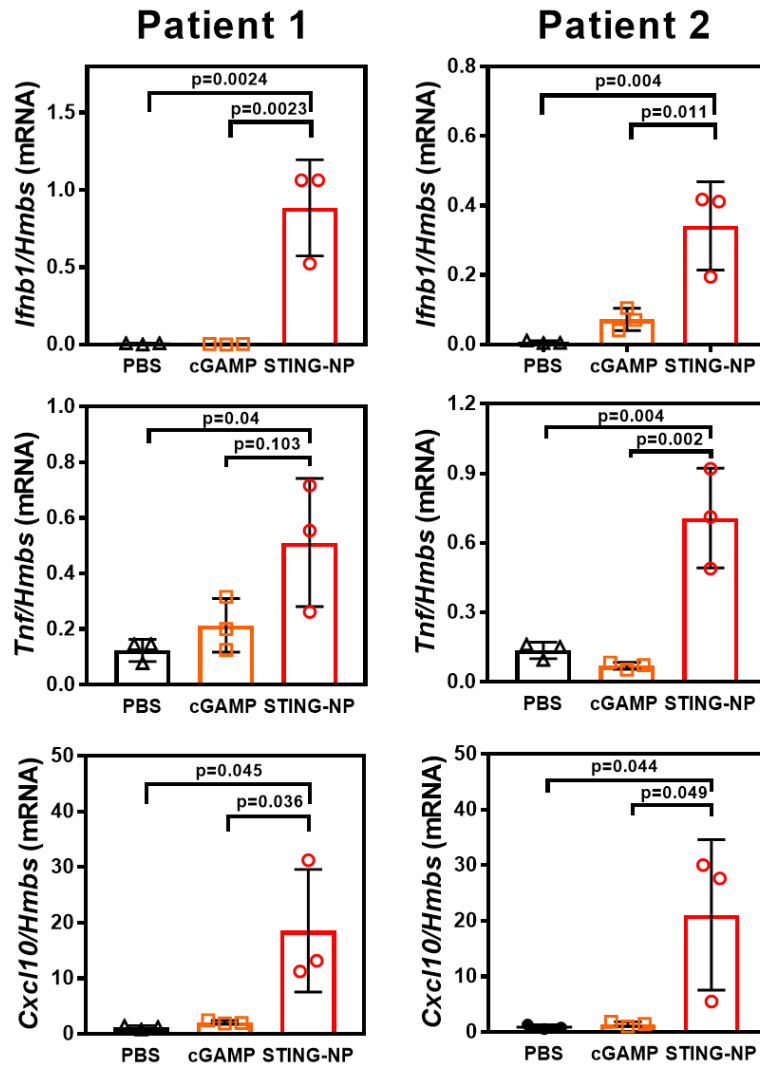


Figure 3.20. STING-NPs enhance cGAMP activity in human metastatic melanoma. Surgically resected melanoma metastases were divided into nine sections (3 per treatment), randomized, and injected intratumorally with STING-NPs or cGAMP at 150 nM and cultured for 24 h. qPCR analysis of *Ifnb1*, *Tnf* and *Cxcl10* gene expression in tissue freshly isolated from two different melanoma patients after indicated treatment.

5x10⁴ B16.F10 cells containing the reporter construct were injected subcutaneously into the flank of 6-8 week old female C57BL/6 (Jackson Labs). Upon reaching ~100 mm³, tumors were injected intratumorally with 100 µL PBS containing 10 µg of cGAMP in the appropriate formulation. At selected time points, mice were injected intraperitoneally with 200 µL of 15mg/mL D-luciferin (ThermoFisher) in PBS. 15 minutes following injection, luminescence was quantified on the IVIS Lumina III (PerkinElmer) using Living Image software (version 4.5).

Mouse Toxicity. Mice bearing subcutaneous tumors were injected intratumorally with PBS, cGAMP or STING-NPs corresponding to a 10µg dose of cGAMP. Upon reaching the tumor size endpoint, blood was harvested via submandibular bleeding, allowed to clot and used to prepare serum by centrifugation at 4000 G. Serum was tested by the Vanderbilt Translational Pathology Shared Resource (TPSR) for levels of alanine aminotransferase, bilirubin, and creatinine. Livers were harvested, fixed in a 10% formalin in PBS solution, paraffin embedded, and sectioned into 5 µm sections for H&E staining. Liver sections were evaluated by a blinded pathologist for signs of hepatotoxicity.

Gene Expression Analysis Following Intratumoral Administration. Female C57BL6/J mice aged 6-8 weeks old were inoculated subcutaneously with 50,000 B16.F10 cells. Upon reaching an average size of ~100 mm³, tumors were treated via IT injection with 100 µL of either PBS, free cGAMP, or STING-NP nanoparticle formulations (10 µg cGAMP per injection). For qPCR analysis, tumors were harvested after four hours, and lysed in RLT lysis buffer (Qiagen) supplemented with 2% β-mercaptoethanol (Sigma) in a gentleMACS M tube with mechanical disruption using an OctoMACS tissue dissociator (Miltenyi). Tumor RNA was isolated with an

RNeasy RNA isolation kit (Qiagen) with the RNase free DNase Set (Qiagen), used according to manufacturer specifications. cDNA was synthesized with the Bio-Rad iScript cDNA kit and analyzed via qPCR using the appropriate TaqMan kits (Thermo Fisher Scientific) or the nCounter PanCancer Immune Profiling Panel (NanoString Technologies). TaqMan™ gene expression kits: Mouse Tnf: Mm00443258_m1. Mouse Ifnb1: Mm00439552_s1. Mouse Cxcl9: Mm00434946_m1. Mouse Cxcl10: Mm00445235_m1. Mouse Hmbs: Mm01143545_m1.

Quantification of CDN accumulation and Ifnb1 expression in the tumor draining lymph node. Subcutaneous B16.F10 tumors of ~100 mm³ were injected with coformulations of cGAMP (10 µg) and cdGMP-Dy547 (0.2 µg). 1 hr after injection, the mice were sacrificed and the inguinal tumor draining lymph node was harvested, placed in RLT tissue lysis buffer (Qiagen), and homogenized using an OctoMACs tissue dissociator. cdGMP-Dy547 was quantified in the resulting lysate on a Synergy H1 plate reader (576/550 Ex/Em). Background fluorescence was removed by subtracting baseline fluorescence values of TDLN lysates from PBS treated tumor bearing mice. For quantification of Ifnb1 expression, subcutaneous B16.F10 tumors were injected with cGAMP formulations (10 µg). 2 hrs after injection, TDLNs were harvested and homogenized in RLT lysis tissue lysis buffer supplemented with 2% β-mercaptoethanol. mRNA isolation, cDNA synthesis, and qPCR quantification of Ifnb1 transcription was performed as described above.

NanoString nCounter Analysis. 100 ng of RNA was isolated as previously described from tumor samples 4h after treatment and analyzed by nanoString nCounter gene expression analysis using the PanCancer Immune Profiling Panel. Fold change was calculated by comparing against average

normalized gene expression values of PBS treated tumors. All statistical significance and clustering analysis was performed in R (<http://cran.r-project.org>).

Flow Cytometric Analysis of the B16.F10 Tumor Microenvironment. B16.F10 tumors were established subcutaneously in C57BL6/J mice as previously described and treated IT with either PBS or coformulations of cGAMP (10 μ g) and cdGMP-Dy547 (0.2 μ g). 48 hours after treatment, tumors and the inguinal draining lymph node were harvested, mechanically dissociated with an OctoMACs separator, and digested in a solution of 125 μ g/mL DNase I (Worthington) and 500 μ g/mL Collagenase III (Worthington) in RPMI 1640 media for 30 minutes at 37°C. Tumors and lymph nodes were then strained through a 40 μ m cell strainer to prepare a single cell suspension and treated with ACK Lysing Buffer (Gibco). Cells were then diluted to a concentration of 2x10⁷ cells/mL in PBS containing 2% BSA for FACS staining. 100 μ L of cell suspension for each flow test was transferred into a 96 well plate and treated with FcX (Biolegend) according to manufacturer specifications. Samples were stained with several panels of the antibodies BV650- α CD45 (30-F11), PE/Cy5- α CD11b (M1/70), PE- α CD11c (N418), PE/Cy7- α NK1.1 (PK136), APC/Cy7- α F4/80 (BM8), APC/Cy7- α MHC-II (10.3.6), PE- α CD206 (C068C2), APC- α CD86 (GL-1), APC- α CD3 (17A2), APC/Cy7 α CD4 (RM4-5), and PE/Cy5- α CD8 α (53.6.7) purchased from Biolegend. Cells were washed twice, suspended in PBS containing 2% FBS and 200 nM DAPI before analysis on a BD LSRFortessa or BD LSR II flow cytometer (**Appendix B.3**).

For intracellular cytokine analysis, 10⁶ cells were seeded in a 6 well plate in DMEM containing 10% FBS and supplemented a PMA/Ionomycin/Brefeldin A cocktail (Biolegend) according to manufacturer specification. Four hours later, cells were washed, stained with antibodies against CD3, CD4, and CD8 α , and subsequently treated stained intracellularly with

antibodies against TNF- α (MP6-XT22) and IFN- γ (XMG1.2) (Biolegend) according to manufacturer specifications with Biolegend Fixation Buffer and Intracellular Staining Permeabilization Wash Buffer. All flow cytometry data was analyzed using FlowJo software (version 10; Tree Star, Inc.).

Treatment of B16.F10 subcutaneous tumors. 5×10^4 B16.F10 cells were injected subcutaneously into the flank of 6-8 year old mice in 100 μ L of serum free RPMI 1640 media. Tumor volume was measured every other day via caliper measurements, and tumor volume calculated using the equation $V = 1/2 \times L \times W \times H$. Upon reaching sizes of ~ 100 mm³, tumors were treated IT with 100 μ L of PBS containing 10 μ g of 2'3'-cGAMP in various formulations. Following treatment, mice were weighed and tumor sizes were measured every two days until reaching a tumor burden endpoint of 1500 mm³. For single tumor models, upon reaching a tumor volume of ~ 100 mm³, tumors were injected intratumorally with 100 μ L of the appropriate formulation in pH 7.4 PBS. Mice were injected 3x with treatments spaced 4 days apart. For contralateral studies, mice were inoculated on each flank subcutaneously with B16.F10 melanoma cells. When the larger of the two tumors reached ~ 100 mm³, it was injected with 100 μ L of the appropriate formulation and designated as the primary tumor, with the untreated tumor designated as the contralateral tumor (average volume = 40 mm³). For mice treated with checkpoint blockade, mice were injected intraperitoneally with 100 μ L of PBS containing 100 μ g of both anti-PD1 (RMP1-14, BioXCell), and anti-CTLA4 (9D9, BioXCell). Treatments were again spaced 4 days apart, with tumor progression and mouse health monitored as described with single tumor studies. For evaluation via systemic administration, mice were injected in the caudal vein with 100 μ L of PBS containing the appropriate formulation seven

days following a tumor inoculum of 5×10^5 B16.F10 cells (average volume = 30 mm³). Checkpoint antibodies were administered as described above, with treatments again spaced 4 days apart.

Labeling of STING-NP polymers. PEG_{2k}-DBP_{4.5k} was dissolved in ethanol and treated with 10x molar excess of Tris(2-carboxyethyl)phosphine hydrochloride (TCEP) and allowed to react for 30 minutes. Without purification, Vivotag-S 750-MAL (PerkinElmer) or Cy5-Maleimide was added to the mixture and allowed to react overnight. Excess reagent was then removed *via* dialysis against water using a 3.5kDa molecular weight cutoff membrane. The retentate was then harvested and lyophilized. The polymer was then re-dissolved in acetone, blended with 9 mass equivalents of unlabeled PEG_{2k}-DBP_{4.5k} and precipitated in pentane. Drying overnight produced a homogenous mixture polymer, which was then used normally for STING-NP formulation.

Biodistributional Analysis of STING-NPs. 5×10^4 B16.F10 cells were injected subcutaneously into the flank of 6-8 year old mice in 100 μ L of serum free RPMI 1640 media. When the tumors reached ~ 100 mm³ in size, STING-NPs were injected into the caudal vein. For qPCR analysis, unlabeled STING-NPs were used, and mice were sacrificed at the denoted time points. The liver, spleen, TDLN, and tumor was harvested, mechanically disrupted using a TissueLyser LT bead mill (Qiagen). mRNA was isolated from the lysate and characterized *via* qPCR as described above. For IVIS quantification, mice were injected with VivoTag-750S labeled STING-NPs. 24h after injection, organs were harvested and analyzed on the IVIS Lumina III. For cellular uptake of STING-NPs, mice were injected with Cy5 labeled STING-NPs. 24h after injections, mice were sacrificed for collection of tissues for analysis. A single cell suspension was prepared for the tumor and TDLN as described above. For the spleen, cells were pushed through a 70 μ m cell strainer,

treated with ACK lysis buffer (KD medical), and washed and resuspended in FACS to create a single cell suspension. Cells were then treated with multiple staining panels comprising antibodies FITC- α CD45 (30-F11), PE/Cy5- α CD11b (M1/70), PE/Cy5- α CD11c (N418), PE/Cy7- α NK1.1 (PK136), APC/Cy7- α F4/80 (BM8), APC/Cy7- α MHC-II (10.3.6) PE/Cy7- α CD3 (17A2), APC/Cy7 α CD4, and BV605- α Ly6C (HK1.4), before analysis on the BD LSRFortessa flow cytometer.

Ex vivo stimulation of resected human metastatic melanoma. All patients were consented for research use of biospecimens (Vanderbilt University Medical Center IRB # 030220). Within an hour of surgical resection at Vanderbilt University Medical Center, human melanoma tumors were submerged in DMEM/F12 media (Gibco) supplemented with 10% FBS and divided into 9 sections using a scalpel. Individual sections were then placed in a 12 well plate containing 1 mL of media and injected with STING-NP, free cGAMP, or PBS with a syringe, reaching a final concentration of 100 ng/mL of cGAMP within each well. 24 hours after treatment, sections were grinded in RLT lysis buffer (Qiagen) supplemented with 2% β -mercaptoethanol (Sigma) using an OctoMACSTM cell separator. RNA isolation, cDNA synthesis, and qPCR analysis were then performed as described previously. TaqManTM gene expression kits: Human Tnf: Hs00174128_m1. Human Ifnb1: Hs01077958_s1. Human Cxcl10: Hs00171042_m1. Human Hmbs: Hs00609296_g1.

Statistical Analysis. All statistical analyses were performed by using GraphPad Prism software, version 7.0. Tumor doubling times were calculated by truncating mean tumor volumes growth curves at the death of the first mouse in a given group. Remaining data points were used as inputs to fit to an exponential growth curve.

Chapter 4. Conclusions

Chapter 4.1. STING-NPs Improve the Delivery of cGAMP to STING, Activating Myeloid and T Cells to Tumoricidal Effect.

Through rational design of nanoparticle properties, we have designed endosomolytic polymersomes to enhance the cytosolic delivery of cGAMP. STING-NPs and related nanoparticle-cGAMP formulations synthesized and characterized *via* a robust series of *in vitro* experiments. STING-NPs demonstrated potent activity in IRF3 reporter cell lines, DC cell lines, BMDMs, and BMDCs, inducing a pro-inflammatory program in each that is expected to contribute to tumor cell death and improvement of T cell priming and activity in the TME. These experiments revealed that STING-NPs owe their activity to an ability to facilitate cGAMP uptake and a pH responsive disassembly and endosomal escape mechanism, which is achieved through precise control of block copolymer synthetic parameters and an *in situ* crosslinking method that allows for formulation of pH responsive, endosomolytic vesicles that efficiently encapsulate the cGAMP molecule.

As demonstrated through *in vivo* experimentation, STING-NPs provide advantages over existing STING agonists and CDN delivery technologies in terms of 1) superior activation of the STING pathway; 2) ability to activate STING in both the tumor and sentinel lymph node; 3) therapeutic efficacy achieved through both IV and IT administration routes, and 4) enhanced synergy with immune checkpoint blockade. We highlight key distinctions between delivery of nucleic acid therapeutics and CDNs while establishing new design principles for nanoparticle delivery of STING agonists. Our findings indicate that STING-NPs enhance cytosolic delivery of cGAMP via an endosomal escape mechanism, preferentially activating STING in myeloid cell populations within the TME and TDLN to trigger a multifaceted shift to a “hot” T cell-inflamed

TME that inhibits tumor growth. As a single agent, locally administered STING-NPs can generate robust and complete responses, eliciting systemic antitumor immunity that can protect against tumor rechallenge. Importantly, STING-NPs can be administered through both IT and IV routes either as monotherapy or in combination with ICB for therapeutic benefit, potentially opening new clinical opportunities for leveraging STING agonists.

4.2. Suggestions for Future Work.

This work has demonstrated that STING-NPs, either as a monotherapy or in combination with ICB and as such have potential for clinical translation. The most natural continuation of this work is to continue to build on pre-clinical experimentation that determines the optimal use, and applicability of STING-NPs. This includes collecting data on the effectiveness of STING-NPs in a diverse array of murine tumor models to demonstrate its ability to effect therapeutic benefit in multiple cancer types. This work has focused in large part on B16.F10 melanoma tumors, a difficult to treat and immunologically cold model. Nevertheless, as a melanoma cell line it has relatively high mutational load and thus likely relatively high expression of tumor neoantigens, several of which have already been identified in the literature.^{129,130} As the proposed mechanism for the effectiveness of STING-NPs largely relies on its ability to jump-start TAA presentation and T-cell priming in immunologically cold tumors, it may be interesting to examine, in particular, the use of STING-NPs in models that differ qualitatively from B16.F10 tumors in an immunological context such as CT26 or 4T1 colon and breast cancer tumors. These tumor cell lines are known to be highly immunogenic and likely more T cell inflamed, and as such the efficacy of STING-NPs and their ability to synergize with ICB may be different in these models. In one potential direction, STING-NPs be less effective in these models as the T-cell priming function

remains intact in these immunogenic tumors, and the ability of STING-NPs to mediate DC maturation may be redundant or unneeded. Alternatively, they may demonstrate improved efficacy, as their ability to reprogram the TME and diminish immunosuppressive function may unleash a pre-existing tumoricidal T cell response. In either case, these studies will guide the optimal use of STING-NPs in the clinic, determining which cancer types STING-NPs are likely to mediate the most benefit in. For the same reason, it is important to study the effect of STING-NPs in a model with differing mutational loads, which most commonly include pediatric cancers. While some preliminary work has already been performed by our lab showing that STING-NPs can induce complete rejection of murine NB9464D and neuro2a neuroblastoma cells, it may be interesting to experiment of cancer models that may show some correlation between mutational load and the effectiveness of STING-NPs. Detailed flow cytometric phenotyping of the myeloid and lymphatic cell compartment in the TME may further elucidate which mechanisms of action are differentially important, if any, in each tumor class.

Further study should focus on optimization of the dosing regimen for STING-NPs. The studies described in this work identified two useful doses that were able to mediate tumor rejection: 10 μ g and 20 μ g for IT and IV administration, respectively. As such the majority of studies regarding phenotyping and tumor characterization were performed with these doses. A formal dose sweeping study should be performed to determine the optimal dose for antitumor efficacy, as well as the maximum tolerated dose (MTD) that may be administered without causing intolerable toxic effects. It is important to note that while typical dose studies for antitumor therapeutics often find that the MTD is also the most effective treatment regime, this may not be the case for STING-NPs and related immunotherapeutic treatments. This is because common cancer drugs typically act through induction of tumor cell death or inhibition of tumorigenic, immunosuppressive, or

angiogenic proteins, and as such improved efficacy often corresponds with higher dosing. By contrast, STING-NPs act through a complex web of interconnected events involving cytokine secretion and T-cell priming, all of which are mediated by immune cells that may themselves be killed by overstimulation of STING. Indeed, one recent study by Sivick *et al.* have reported that administration of extremely high doses of cGAMP can result in poor T-cell infiltration due to overstimulation of APC.⁵⁰ As such, further STING-NP dosing studies should be sure to investigate both more and less intensive dosing regimens. Critically, Sivick *et al.* demonstrated that optimal T cell priming was not necessarily correlated with optimal tumor ablation. Thus, these dosing optimization studies should consider both tumor growth profiles and T cell infiltration as readouts, as higher doses may induce more tumor suppression, while more moderate doses may synergize better with ICB and generate more durable adaptive responses for resistance to metastatic recurrence.

Finally, future investigators may wish to perform a more comprehensive toxicology study on mice treated with STING-NPs. While the studies described here revealed no long-term evidence of liver toxicity in STING-NP treated mice, it may be valuable to perform a more comprehensive study on other organs such as the kidney and spleen, which themselves are seen to accumulate some quantity of STING-NPs. In general, further toxicology studies should cast as wide a net as possible, as even though STING-NPs may not accumulate in every organ, pro-inflammatory cytokines secreted by STING-NP exposed cells likely readily flow into the vasculature, themselves generating pro-inflammatory feedback loops. Furthermore, researchers may find it informative to look more closely at acute adverse effects following STING-NP treatment, which are largely uninvestigated in this work aside from basic mouse weight readouts. Collectively, these data may serve as the base for potential clinical study of STING-NPs.

A second potential field of investigation involves leveraging the ability of STING-NPs to encapsulate a variety of cargo. Critically, STING-NPs have both hydrophilic and hydrophobic domains within which a diverse array of cargo can be theoretically encapsulated. Similarly, the direct hydration process involves both organic and aqueous addition steps, allowing for facile incorporation of different cargo types into the nanoparticle. We have previously demonstrated the ability of these nanoparticles to encapsulate proteins, nucleic acids, and amphiphilic small molecules, in addition to cGAMP. Thus, STING-NPs are an excellent platform through which co-delivery of cGAMP and other cancer immunotherapeutics, be they chemotherapeutics, siRNAs, or other PRR agonists, to search for synergies between these different drugs. These types of studies are well grounded in the literature, which for instance, have reported synergistic activation of innate an adaptive immunity using different combinations of PRR ligands.^{131–133} In one report that is especially relevant, Temizoz *et al.* have reported synergistic activation of T-cells through IT injection STING ligands and the TLR9 ligand CpG ODN, which they attribute to concurrent production of IFN-I and IL-12 induced by simultaneous PRR activation.¹³⁴ STING-NPs have potential to add value to these types of studies due to their ability to drug endosomal and cytosolic targets through a platform for which various cargos can be combinatorially incorporated. For synergy studies that have historically been held back by delivery barriers involving drugs such as STING agonists, retinoic acid inducible gene-I, small interfering RNA or messenger RNA therapeutics, STING-NPs may represent a platform that enables investigation of novel drug combinations.

These types of future investigations can be guided in part by some of the data that this work has produced. In particular, nanoString gene multiplex analysis gives information on a multitude of genes that are upregulated in response to STING activation. While we did demonstrate that

STING-NPs act well in concert with PD-1 and CTLA-4 blockade, synergistic intervention targeting other genes potentially connected to STING signaling remains largely unexplored. While detailed discussion of the hundreds of examined genes is out of the scope of this work, we will provide a starting point here by highlighting several upregulated genes that may have implications for high impact drug combinations (**Figure 4.1**).

Transcription of several genes encoding PRRs is upregulated following STING activation, including those for the surface receptors TLR2 and TLR3 and the intracellular receptors RIG-I (*DDX58*) and NOD-like receptors (NLRs; *Nod1*, *Nod2*). Upregulation of these genes suggests that stimulation of STING may sensitize the TME to further immunotherapy using ligands for these receptors. The TLR3 ligand poly(ICLC) particular has shown particular promise in the field of cancer immunotherapy and has recently demonstrated the ability to stimulate potent antitumor T cell responses in clinical cancer vaccine trials targeting neoantigens for melanoma, glioblastoma, and breast cancer (refs). Another potential target, RIG-I, is a cytosolic target that senses 5' di- or triphosphorylated double stranded RNA that poses similar deliver challenges to STING ligands. It is currently being examined in clinical trials (NCT03065023), and represents an ideal target for potential synergistic targeting by STING-NPs co-loaded with 5' triphosphorylated RNA adjuvants. Similarly, several NLR ligands have been developed for cancer immunotherapy that may be candidates for co-encapsulation in STING-NPs. One such drug, mifamurtide is an amphiphilic synthetic drug that is currently encapsulated within liposomes for administration and is approved by the European Medicine Agency for use treatment of osteosarcoma, although it did not receive FDA approval. Its hydrophobic domain would likely easily incorporate into the bilayer of STING-NPs for co-delivery with cGAMP.

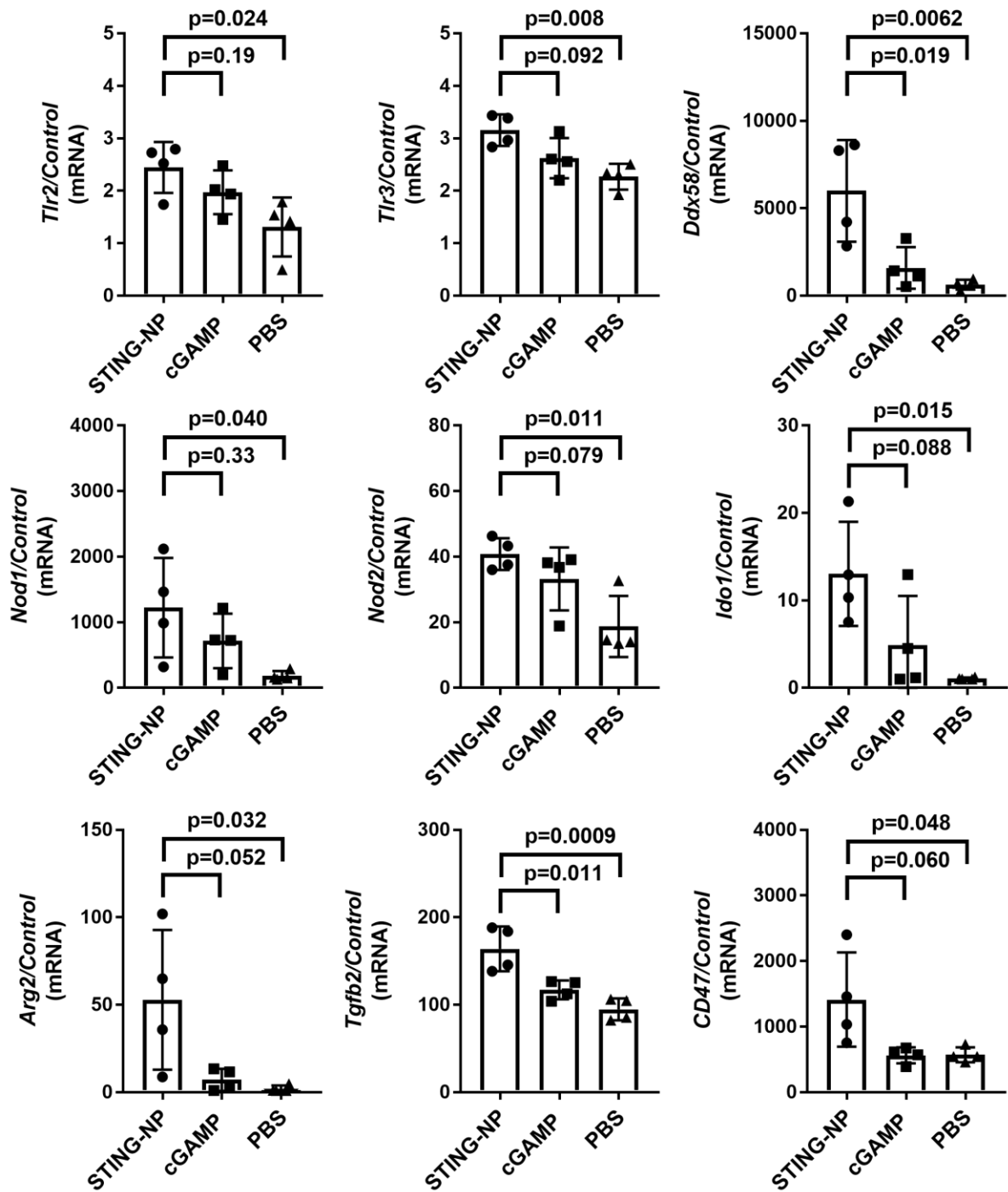


Figure 4.1. Potential targets for synergistic combination therapy with STING-NPs. Genes that were revealed by nanoString multiplex mRNA quantification to be upregulated in response to STING-NPs that are relevant to immunosuppression or stimulation of innate immunity are presented. Statistical test: one-way ANOVA with post-hoc Tukey test.

Similarly, gene expression analysis suggests that STING-NPs may be well suited for intracellular co-targeting of the IDO and Arg-2 immunosuppressive pathways. As previously described, these are two metabolic proteins that diminish T cell function by depleting the TME of the critical T cell acids tryptophan and arginase, respectively. IDO was the target of a recent high publicity clinical trial in which a synthetic inhibitor, epacadostat (Incyte) failed to improve progression free survival in a phase III trial on metastatic melanoma in combination with PD-1 blockade. Nevertheless, IDO has been strongly implicated in T cell dysfunction in tumor bearing patients, and our data suggest that it may be a critical upregulated mechanism of immunosuppression following STING activation. Encapsulation of epacadostat or similar IDO inhibitors within STING-NPs may improve efficacy by 1) sensitizing tumors, and 2) increasing rates of cellular uptake of the small molecule drug. Analogous reasoning applies to arginase inhibitors, which are currently being explored for use in solid cancers in combination with PD-1 blockade (INCB001158).

Finally, the efficacy of STING-NPs may be improved through simple co-administration of receptor blocking antibodies. TGF- β 2 (*Tgfb2*) in particular is one critical immunosuppressive protein that is upregulated following STING-NP activation. The negative effects of this response could be easily mitigated with coadministration of antibodies against TGF- β receptors. CD47 is similarly a surface receptor that appears to be upregulated in response to STING activation, which could be blocked via antibody treatment for combination therapy. Interestingly, this is a protein that is commonly expressed by healthy cells and erythrocytes throughout the body as a negative regulator for phagocytosis. Overexpression of CD47 has been implicated in decreased cross presentation of TAA by DCs and subsequent T cell activation (CD47 blockade triggers...) as well as direct tumor phagocytosis and destruction by myeloid cells (Is CD47 an innate immune). Simple

tumor growth models could rapidly determine whether these simple additional interventions could improve the efficacy and translational potential of STING-NPs.

Additional effort should be focused on the mechanisms through which STING-NPs effect tumor rejection. Investigation of the cellular players in STING-NP uptake revealed that encapsulation of CDNs within STING-NPs skewed uptake towards CD45- cell populations, which are largely assumed to be tumor cells. As previously stated, the importance of this phenomenon to the antitumor efficacy of STING-NPs was unclear, as the vast majority of IFN-I appeared to be produced from myeloid cells. However, several experiments could elucidate the relevance of direct STING activation in the tumor compartment mediated by STING-NPs. The ability of STING-NPs to induce expression of surface DAMPs such as CRT and HMGB1 that induce tumor cell phagocytosis and cross-presentation should be evaluated in B16.F10 melanoma. Additionally, comparison of treatment of tumors established using normal and STING-KO B16.F10 cells could shed light on the relative importance of STING signaling and ICB in tumor cells. Use of fluorescently labeled cells and quantification of primed antigen specific T cells would be particularly informative, allowing the investigator to determine the effect of tumor cell uptake by APCs on myeloid cell phenotype and T cell activation. Collectively, these experiments could provide more information on the importance of tumor intrinsic STING signaling in cancer immunity. These data may inform clinical studies of STING-NPs, demonstrating that STING therapy is more effective in tumor types where STING-signaling is intact, and may reveal that the ability of STING-NPs to shift the uptake profile of CDNs towards the tumor compartment is a unique advantage of nanoparticulate packing of STING agonists over small molecule synthetic strategies. Alternatively, it may demonstrate the opposite, which would indicate that STING-NPs are likely to be similarly effective in a broad array of cancer types, regardless of STING expression

by the tumor compartment. This too would have interesting implications for design of nanoparticles for STING delivery, suggesting that surface functionalization strategies to induce uptake by myeloid cells may be particularly important for maximizing efficacy.

Investigation into the importance of individual cell types on the immune response may also yield important information. Sequential examination of the effect of cellular depletion on the antitumor efficacy of STING-NPs would reveal the critical cellular players in tumor rejection. Particular attention should be paid to the neutrophil compartment; while the effect of many cell subsets discussed in this work on disease outcome is well characterized, the role of neutrophils is somewhat more ambiguous. A large body of literature characterizes neutrophils as playing primarily an immunosuppressive role in the TME, with several seminal reviews demonstrating that neutrophils are a negative prognostic marker for patient survival.^{135,136} On the other hand, neutrophils are well known to have direct tumoricidal activity, and several reports have implicated neutrophils as critical mediators of tumor rejection in response to IT immunotherapies. This ambiguity is in part due to surface marker overlap between MDSCs, particularly g-MDSCs, and neutrophils; distinguishing between the two types of cells through flow cytometric techniques is difficult, and many reports have simply conglomerated g-MDSCs and neutrophils together in their analysis, with the former demonstrating clear immunosuppressive abilities.¹³⁷ These analyses are further complicated by the phenotypic plasticity of neutrophils, and it is unclear whether the striking increase in neutrophilic tumor infiltrate following STING-NP treatment is critical to tumor rejection, diminishing other tumoricidal effects of STING-NPs, or somewhere in between, and nuanced investigation into this topic would be enlightening.

In addition to neutrophilic depletion, related cellular depletion strategies may provide information on the relative importance of the myeloid and T cell compartments in the response to

STING-NPs. As previously stated, depletion of MDSCs in particular is also of interest, as it may represent a simple method through which therapeutic outcomes may be improved. However, we also note that selective depletion of MDSCs instead of neutrophils (and to a lesser extent, neutrophils instead of MDSCs) is difficult, again due to surface marker overlap. If it is indeed found that neutrophils play a crucial role in tumor rejection in STING-NP treated tumors, depletion of the entire MDSC and neutrophil cell subsets may decrease the efficacy of STING-NPs despite mitigating the recruitment of immunosuppressive MDSCs to the TME. These cells play a complex and interconnected role in tumor progression, and their roles in the tumor immune microenvironment can and should be elucidated through future empirical investigation.

Finally, we include some suggestions for future innovation in nanoparticle design. Analysis of fluorescently labeled analogues indicates that the vast majority of STING-NPs appear to accumulate within the liver following IV administration. While we were encouraged that STING-NPs were apparently potent enough to mediate tumor rejection through this administration route, the fact remains that the biodistribution of STING-NPs is clearly suboptimal, which both may diminish their antitumor efficacy while contributing to acute toxicity in treated mice. The susceptibility of STING-NPs to RES clearance suggests that translational potential could be significantly improved through modification of the nanoparticle corona. Although the PEG hydrophilic block of PEG_{2k}-DBP_{4.5k} polymer is well known to minimize clearance by deterring the adsorption of opsonizing proteins, its ability to do so is dependent on molecular weight of the PEG block. Gref *et al.* have studied this effect in a seminal study, finding PEG coronas comprising 2kDa blocks were significantly less effective than those of larger molecular weight.¹³⁸ STING-NPs may therefore benefit from a larger PEG corona to further minimize RES clearance.

We demonstrate in this work that PEG-DB block copolymers comprising 5kDa PEG blocks are not readily formulated into vesicular structures. The same is likely true of PEG-DBP polymers, as the driving forces that favor micellar self-assembly for higher molecular weight polymers are not strongly influenced by the composition of the hydrophobic block. However, several strategies may be employed to incorporate larger PEG chains within the STING-NP. One such strategy is a hydrophobic anchoring strategy that is commonly used to PEGylate liposomal nanoparticles in which hydrophobic tails are conjugated to a high molecular weight hydrophobic chain and used to anchor the PEG to the vesicular bilayer. These PEG chains may be doped into the direct hydration PEG-DBP polymer formulation feed or may be added to preformed particles to surface functionalize STING-NPs, and each strategy carries potential formulation pitfalls. In the former case, doping large amounts high molecular weight PEG into PEG-DBP polymers may influence the self-assembled morphology, leading to lower polymer yield or encapsulation efficiency, shifts in nanoparticle size, or in the worst case an unusable self-assembled nanoparticle architecture. In the same report, Gref *et al.* found that a ~5% weight content or higher of large PEGs within the polymer feed was required for optimal inhibition of protein adsorption, and it is unclear whether or not such a high amount of additional polymer in the PEG-DBP feed is compatible with the self-assembly of STING-NPs. By contrast, addition of high molecular weight PEG with a hydrophobic tail to a colloid of pre-formed STING-NPs poses less risk to the morphological integrity of STING-NPs, but may not be able to penetrate through the PEG_{2k} corona of STING-NPs to successfully anchor into the hydrophobic bilayer. Furthermore, this grafting-to surface functionalizing strategy is well known to have difficulty achieving high grafting densities due to steric barriers in the nanoparticle corona: a problem that would be exacerbated by the high molecular weight PEGs required to mitigate surface fouling of the nanoparticle. Ultimately, both of these formulation

strategies are a good topic for future investigation and may yield vast improvements in the pharmacokinetics and efficacy of STING-NPs.

Alternatively, RES clearance of next generation STING-NPs could be minimized through alteration of the corona chemistry. While PEGylation is a commonly used and highly successful strategy to improve nanoparticle and drug circulation time, a growing body of literature suggests that the PEG corona may not be optimal for inhibition of cellular uptake. As stated before, relatively large molecular weights are required to diminish adsorption of opsonins. Even in optimal conditions of high grafting density and high molecular weight PEG (10 kDa), Pelaz *et al.* have reported protein adsorption of common blood proteins such as fibrinogen and serum albumin, given sufficiently high protein concentrations, motivating researchers to search for additional strategies to impart stealth properties to nanoparticle vehicles.¹³⁹ Zwitterionic coronas have garnered increasing interest in recent years as potential alternatives to PEGylation and have been reported to be an effective deterrence to opsonization at much lower molecular weights. In particularly striking examples, surface functionalization of inorganic nanoparticles with monolayers of zwitterions appears to inhibit protein adsorption,¹⁴⁰ suggesting that this type of surface chemistry would be well-suited to minimize RES clearance without the need to increase the molecular weight of the STING-NP corona. The potential of this approach was recently highlighted in a recent report by Jackson *et al.* who demonstrated that zwitterion functionalized polymeric carriers demonstrated significantly improved accumulation and gene deliveries in the TME than did PEGylated analogues.¹⁴¹ This approach may thus prove to be a facile method of improving circulation time without compromising the self-assembly of STING-NPs.

Furthermore, there are several available zwitterionic methacrylates that, in contrast to ethylene oxide monomers used to synthesize PEG, are compatible with the facile RAFT

polymerization process. This would facilitate the customization of the polymer corona by enabling co-polymerization of clickable groups within the hydrophilic polymer block, which would unlock a plethora of potential improvements in the STING-NP platform. From here, various stealth ligands can be grafted directly onto the nanoparticle surface without having to diffuse through the corona for access to the hydrophobic bilayer. Functionalization of nanoparticles with cellular targeting ligands may also yield interesting results and for instance, may be used to increase the rate of uptake by APCs that are critical to the T cell priming process. Targeting CD40 or CD206 for instance for DC and TAM targeting, has already been shown to improve antigen presentation in several nanoparticle vaccination platforms, and may yield similar improvements for *in situ* vaccination by STING-NPs.¹⁴²⁻¹⁴⁴

Surface functionalization with targeting ligands also affords the possibility to directly test and potentially exploit the phenomenon of active trafficking of STING-NPs to the TME. As described in section 3.10 differential cellular uptake profiles induced by IV and IT administration routes is suggestive, though not conclusive, that STING-NPs may be partially reliant on uptake and subsequent tumor migration by circulating myeloid cells for enrichment in the tumor. In particular, targeting of Ly6C or Ly6G surface proteins would increase particle association with MDSCs, allowing a future investigator to evaluate the importance of this active trafficking phenomenon, which could significantly improve the biodistribution and subsequent efficacy of STING-NPs. Indeed, similar strategies have employing monocyte or T-cell active targeting for delivery of immunosupportive cytokines and diagnostic nanoparticles have garnered significant interest in the community as potential alternatives to passive accumulation strategies.^{126,145} For MDSC and neutrophil targeted STING-NPs in particular, sequential doses may demonstrate

increasing improvements in tumor accumulation, due to large influx of these cell types into the TME following STING-NP administration.

In conclusion, the experiments detailed in this work have demonstrated that STING-NPs are effective delivery vehicles for CDNs, and likely for other cytosolically active immunotherapeutics. As demonstrated by their efficacy in a variety of immunologically cold and rigorous tumor models, STING-NPs are a powerful addition to the immunotherapeutic toolbox and synergize well with the most promising immunotherapies on the market today. Although STING-NPs as described have exciting translational potential, significant improvements in the technology can likely be made through future particle engineering as well as through further exploration of combination therapies. In addition to resulting in the production of a useful cancer therapeutic, the process of STING-NP design has highlighted several critical design concepts for efficient CDN delivery. Likewise, biological characterization of the downstream effects of STING-NP administration has yielded insight into the phenotypic shifts in the tumor and lymphoid organs caused by high magnitude STING activation. It is my hope that these results inform the rational design of the next generation of further optimized nanoparticle drug delivery vehicles and immunotherapeutic treatment regimens.

References

1. Oiseth, S. J. & Aziz, M. S. Cancer immunotherapy: a brief review of the history, possibilities, and challenges ahead. *J. Cancer Metastasis Treat.* **3**, 250 (2017).
2. Decker, W. K. *et al.* Cancer immunotherapy: Historical perspective of a clinical revolution and emerging preclinical animal models. *Front. Immunol.* **8**, (2017).
3. Coley, W. B. The treatment of inoperable sarcoma by bacterial toxins. *Practitioner* **83**, 589–613 (1909).
4. Galon, J. *et al.* Immunoscore and Immunoprofiling in cancer: An update from the melanoma and immunotherapy bridge 2015. *J. Transl. Med.* **14**, 1–6 (2016).
5. T.N., S. & R.D., S. Neoantigens in cancer immunotherapy. *Science (80-.)*. **348**, 69–74 (2015).
6. Noy, R. & Pollard, J. W. Tumor-Associated Macrophages: From Mechanisms to Therapy. *Immunity* **41**, 49–61 (2014).
7. Shibata, M., Gonda, K. & Takenoshita, S. MDSC: Myeloid-derived suppressor cells. *Immunother. Cancer An Innov. Treat. Comes Age* 323–334 (2016). doi:10.1007/978-4-431-55031-0_22
8. Tanaka, A. & Sakaguchi, S. Regulatory T cells in cancer immunotherapy. *Cell Res.* **27**, 109–118 (2017).
9. Robert, C. *et al.* Nivolumab in Previously Untreated Melanoma without *BRAF* Mutation. *N. Engl. J. Med.* **372**, 320–330 (2015).
10. Larkin, J. *et al.* Combined Nivolumab and Ipilimumab or Monotherapy in Untreated Melanoma. *N. Engl. J. Med.* **373**, 23–34 (2015).
11. Topalian, S. L. *et al.* Survival, durable tumor remission, and long-term safety in patients with advanced melanoma receiving nivolumab. *J. Clin. Oncol.* **32**, 1020–1030 (2014).
12. Hellmann, M. D. *et al.* Nivolumab plus ipilimumab as first-line treatment for advanced non-small-cell lung cancer (CheckMate 012): results of an open-label, phase 1, multicohort study. *Lancet Oncol.* **18**, 31–41 (2017).
13. Weber, J. S. *et al.* Nivolumab versus chemotherapy in patients with advanced melanoma who progressed after anti-CTLA-4 treatment (CheckMate 037): A randomised, controlled, open-label, phase 3 trial. *Lancet Oncol.* **16**, 375–384 (2015).
14. Teng, M. W. L., Ngiow, S. F., Ribas, A. & Smyth, M. J. Classifying cancers based on T-cell infiltration and PD-L1. *Cancer Res.* **75**, 2139–2145 (2015).
15. Marin-Acevedo, J. A. *et al.* Next generation of immune checkpoint therapy in cancer: New developments and challenges. *J. Hematol. Oncol.* **11**, 1–20 (2018).
16. Moore, K. W. *et al.* IL-10 acts on the antigen-presenting cell to inhibit cytokine production by Th1 cells. *The Journal of Immunology.* **6**, (2016).
17. Chen, W. *et al.* Conversion of Peripheral CD4⁺ CD25⁻ Naive T Cells to CD4⁺ CD25⁺ Regulatory T Cells by TGF- β Induction of Transcription Factor *Foxp3*. *J. Exp. Med.* **198**, 1875–1886 (2003).
18. Rodriguez, P. C. *et al.* Arginase I production in the tumor microenvironment by mature myeloid cells inhibits T-cell receptor expression and antigen-specific T-cell responses. *Cancer Res.* **64**, 5839–5849 (2004).
19. Munn, D. H. & Mellor, A. L. IDO in the Tumor Microenvironment: Inflammation,

- Counter-Regulation, and Tolerance. *Trends Immunol.* **37**, 193–207 (2016).
20. Mezrich, J. D. *et al.* An Interaction between Kynurenine and the Aryl Hydrocarbon Receptor Can Generate Regulatory T Cells. *J. Immunol.* **185**, 3190–3198 (2010).
 21. Michot, J. M. *et al.* Immune-related adverse events with immune checkpoint blockade: A comprehensive review. *Eur. J. Cancer* **54**, 139–148 (2016).
 22. Biswas, S. K. & Mantovani, A. Macrophage plasticity and interaction with lymphocyte subsets: Cancer as a paradigm. *Nat. Immunol.* **11**, 889–896 (2010).
 23. Tcyganov, E., Mastio, J., Chen, E. & Gabrilovich, D. I. Plasticity of myeloid-derived suppressor cells in cancer. *Curr. Opin. Immunol.* **51**, 76–82 (2018).
 24. Coyne, C. B., Zeh, H. J., Lotze, M. T., Tang, D. & Kang, R. PAMPs and DAMPs: signal 0s that spur autophagy and immunity. *Immunol. Rev.* **249**, 158–75 (2012).
 25. Tonegawa, S. Somatic generation of antibody diversity. *Nature* **302**, 575–581 (1983).
 26. Guermontprez, P., Valladeau, J., Zitvogel, L., Théry, C. & Amigorena, S. Antigen Presentation and T Cell Stimulation by Dendritic Cells. *Annu. Rev. Immunol.* **20**, 621–667 (2002).
 27. Sallusto, F. *et al.* Rapid and coordinated switch in chemokine receptor expression during dendritic cell maturation. *Eur. J. Immunol.* **28**, 2760–2769 (1998).
 28. Lenschow, D. J., Walunas, T. L. & Jeffrey, A. Cd28 / B7 System of T Cell. *Annu. Rev. Immunol.* **14**, 233–58 (1996).
 29. Mar, V. J. *et al.* BRAF/NRAS wild-type melanomas have a high mutation load correlating with histologic and molecular signatures of UV damage. *Clin. Cancer Res.* **19**, 4589–4598 (2013).
 30. Pinzon-Charry, A., Maxwell, T. & López, J. A. Dendritic cell dysfunction in cancer: A mechanism for immunosuppression. *Immunol. Cell Biol.* **83**, 451–461 (2005).
 31. Gabrilovich, D. I., Corak, J., Ciernik, I. F., Kavanaugh, D. & Carbone, D. P. Decreased antigen presentation by dendritic cells in patients with breast cancer. *Clin. Cancer Res.* **3**, 483–490 (1997).
 32. Almand, B. *et al.* Clinical significance of defective dendritic cell differentiation in cancer. *Clin. Cancer Res.* **6**, 1755–1766 (2000).
 33. Gabrilovich, D. I. Myeloid-derived suppressor cells. *Cancer Immunol. Res.* 323–334 (2016). doi:10.1007/978-4-431-55031-0_22
 34. Sharma, M. D. *et al.* The PTEN pathway in Tregs is a critical driver of the suppressive tumor microenvironment. *Sci. Adv.* **1**, 1–16 (2015).
 35. Neefjes, J., Jongstra, M. L. M., Paul, P. & Bakke, O. Towards a systems understanding of MHC class I and MHC class II antigen presentation. *Nat. Rev. Immunol.* **11**, 823–836 (2011).
 36. Spranger, S., Dai, D., Horton, B. & Gajewski, T. F. Tumor-Residing Batf3 Dendritic Cells Are Required for Effector T Cell Trafficking and Adoptive T Cell Therapy. *Cancer Cell* **31**, 711–723.e4 (2017).
 37. Hildner, K. *et al.* Batf3 Deficiency Reveals a Critical Role for CD8 α + Dendritic Cells in Cytotoxic T Cell Immunity. *Publ. Sci.* **322**, 1097–1101 (2008).
 38. Bonnotte, B. *et al.* Role of tumor cell apoptosis in tumor antigen migration to the draining lymph nodes. *J. Immunol.* **164**, 1995–2000 (2000).
 39. Li, X.-D. *et al.* Pivotal Roles of cGAS-cGAMP Signaling in Antiviral Defense and Immune Adjuvant Effects. *Science (80-.)*. **341**, 1390–1394 (2013).
 40. Shen, Y. J. *et al.* Genome-derived cytosolic DNA mediates type I interferon-dependent

- rejection of B cell lymphoma cells. *Cell Rep.* **11**, 460–473 (2015).
41. Jiaxi, W. *et al.* Cyclic GMP-AMP Is an Endogenous Second Messenger in Innate Immune Signaling by Cytosolic DNA. *Science* (80-.). **339**, 826–830 (2013).
 42. Woo, S. R. *et al.* STING-dependent cytosolic DNA sensing mediates innate immune recognition of immunogenic tumors. *Immunity* **41**, 830–842 (2014).
 43. Song, S. *et al.* Decreased expression of STING predicts poor prognosis in patients with gastric cancer. *Sci. Rep.* **7**, (2016).
 44. Downey, C. M., Aghaei, M., Schwendener, R. A. & Jirik, F. R. DMXAA causes tumor site-specific vascular disruption in murine non-small cell lung cancer, and like the endogenous non-canonical cyclic dinucleotide STING agonist, 2'3'-cGAMP, induces M2 macrophage repolarization. *PLoS One* **9**, 10–12 (2014).
 45. Ager, C. R. *et al.* Intratumoral STING Activation with T-cell Checkpoint Modulation Generates Systemic Antitumor Immunity. *Cancer Immunol. Res.* **5**, 676–684 (2017).
 46. Ohkuri, T. *et al.* Intratumoral administration of cGAMP transiently accumulates potent macrophages for anti-tumor immunity at a mouse tumor site. *Cancer Immunol. Immunother.* **66**, 705–716 (2017).
 47. Demaria, O. *et al.* STING activation of tumor endothelial cells initiates spontaneous and therapeutic antitumor immunity. *Proc. Natl. Acad. Sci.* **112**, 15408–15413 (2015).
 48. Corrales, L. *et al.* Direct Activation of STING in the Tumor Microenvironment Leads to Potent and Systemic Tumor Regression and Immunity. *Cell Rep.* **11**, 1018–1030 (2015).
 49. Nakamura, T. *et al.* Liposomes loaded with a STING pathway ligand, cyclic di-GMP, enhance cancer immunotherapy against metastatic melanoma. *J. Control. Release* **216**, 149–157 (2015).
 50. Sivick, K. E. *et al.* Magnitude of Therapeutic STING Activation Determines CD8+ T Cell-Mediated Anti-tumor Immunity. *Cell Rep.* **25**, 3074–3085.e5 (2018).
 51. Koshy, S. T., Cheung, A. S., Gu, L., Graveline, A. R. & Mooney, D. J. Liposomal Delivery Enhances Immune Activation by STING Agonists for Cancer Immunotherapy. *Adv. Biosyst.* **1**, 1600013 (2017).
 52. Hanson, M. C. *et al.* Nanoparticulate STING agonists are potent lymph node-targeted vaccine adjuvants. *J. Clin. Invest.* **125**, 2532–2546 (2015).
 53. Li, T. *et al.* Antitumor Activity of cGAMP via Stimulation of cGAS-cGAMP-STING-IRF3 Mediated Innate Immune Response. *Sci. Rep.* **6**, 1–14 (2016).
 54. Nathanson, S. D. Insights into the mechanisms of lymph node metastasis. *Cancer* **98**, 413–423 (2003).
 55. Munn, D. H. *et al.* Expression of indoleamine 2,3-dioxygenase by plasmacytoid dendritic cells in tumor-draining lymph nodes. *J. Clin. Invest.* **114**, 280–290 (2004).
 56. Imai, K. *et al.* Inhibition of dendritic cell migration by transforming growth factor-1 increases tumor-draining lymph node metastasis. *J. Exp. Clin. Cancer Res.* **31**, 3 (2012).
 57. Munn, D. H. & Mellor, A. L. The tumor-draining lymph node as an immune-privileged site. *Immunol. Rev.* **213**, 146–158 (2006).
 58. Thomas, S. N., Vokali, E., Lund, A. W., Hubbell, J. A. & Swartz, M. A. Targeting the tumor-draining lymph node with adjuvanted nanoparticles reshapes the anti-tumor immune response. *Biomaterials* **35**, 814–824 (2014).
 59. Liu, H. *et al.* Structure-based programming of lymph-node targeting in molecular vaccines. *Nature* **507**, 519–522 (2014).
 60. Le Bon, A. *et al.* Direct Stimulation of T Cells by Type I IFN Enhances the CD8+ T Cell

- Response during Cross-Priming. *J. Immunol.* **176**, 4682–4689 (2006).
61. Hervas-Stubbs, S. *et al.* Conventional but Not Plasmacytoid Dendritic Cells Foster the Systemic Virus-Induced Type I IFN Response Needed for Efficient CD8 T Cell Priming. *J. Immunol.* **193**, 1151–1161 (2014).
 62. Curtsinger, J. M. & Mescher, M. F. Inflammatory cytokines as a third signal for T cell activation. *Curr. Opin. Immunol.* **22**, 333–340 (2010).
 63. Scallan, J. P., Zawieja, S. D., Castorena-Gonzalez, J. A. & Davis, M. J. Lymphatic pumping: mechanics, mechanisms and malfunction. *J. Physiol.* **594**, 5749–5768 (2016).
 64. Sarin, H. *et al.* Physiologic upper limit of pore size in the blood-tumor barrier of malignant solid tumors. *J. Transl. Med.* **7**, 1–13 (2009).
 65. Reddy, S. T., Rehor, A., Schmoekel, H. G., Hubbell, J. A. & Swartz, M. A. In vivo targeting of dendritic cells in lymph nodes with poly(propylene sulfide) nanoparticles. *J. Control. Release* **112**, 26–34 (2006).
 66. Maeda, H., Wu, J., Sawa, T., Matsumura, Y. & Hori, K. Tumor vascular permeability and the EPR effect in macromolecular therapeutics: a review. *J. Control. Release* **13**, 1145–1160 (2000).
 67. Soo Choi, H. *et al.* Renal clearance of quantum dots. *Nat. Biotechnol.* **25**, 1165–1170 (2007).
 68. Yu, M. & Zheng, J. Clearance Pathways and Tumor Targeting of Imaging Nanoparticles. *ACS Nano* **9**, 6655–6674 (2015).
 69. Varkouhi, A. K., Scholte, M., Storm, G. & Haisma, H. J. Endosomal escape pathways for delivery of biologicals. *J. Control. Release* **151**, 220–228 (2011).
 70. Nelson, C. E. *et al.* Balancing cationic and hydrophobic content of PEGylated siRNA polyplexes enhances endosome escape, stability, blood circulation time, and bioactivity in vivo. *ACS Nano* **7**, 8870–8880 (2013).
 71. Murthy, N., Campbell, J., Fausto, N., Hoffman, A. S. & Stayton, P. S. Design and synthesis of pH-responsive polymeric carriers that target uptake and enhance the intracellular delivery of oligonucleotides. *J. Control. Release* **89**, 365–374 (2003).
 72. Lin, S. *et al.* An Acid-Labile Block Copolymer of Poly(2-dimethylamino)ethyl methacrylate and Poly(ethylene glycol) as Potential Carrier for Intelligent Gene Delivery Systems. *Biomacromolecules* **9**, 109–115 (2008).
 73. Urban-Klein, B., Werth, S., Abuharbid, S., Czubayko, F. & Aigner, A. RNAi-mediated gene-targeting through systemic application of polyethylenimine (PEI)-complexed siRNA in vivo. *Gene Ther.* **12**, 461–466 (2005).
 74. Werth, S. *et al.* A low molecular weight fraction of polyethylenimine (PEI) displays increased transfection efficiency of DNA and siRNA in fresh or lyophilized complexes. *J. Control. Release* **112**, 257–270 (2006).
 75. Zintchenko, A. *et al.* Simple modifications of branched PEI lead to highly efficient siRNA carriers with low toxicity. *Pharmaceutical Biology - Biotechnology and Center for NanoScience (CeNS), a. Pharm. Biol.* **1**, 5–6 (2008).
 76. Kocak, G., Tuncer, C. & Bütün, V. PH-Responsive polymers. *Polym. Chem.* **8**, 144–176 (2017).
 77. Vermeulen, L. M. P., De Smedt, S. C., Remaut, K. & Braeckmans, K. The proton sponge hypothesis: Fable or fact? *Eur. J. Pharm. Biopharm.* **129**, 184–190 (2018).
 78. Chiefari, J. *et al.* Living free-radical polymerization by reversible addition - Fragmentation chain transfer: The RAFT process. *Macromolecules* **31**, 5559–5562 (1998).

79. Mayadunne, R. T. A. *et al.* Living radical polymerization with reversible addition-fragmentation chain transfer (RAFT polymerization) using dithiocarbamates as chain transfer agents. *Macromolecules* **32**, 6977–6980 (1999).
80. Chong, B. Y. K., Le, T. P. T., Moad, G., Rizzardo, E. & Thang, S. H. More versatile route to block copolymers and other polymers of complex architecture by living radical polymerization: the RAFT process. *Macromolecules* **32**, 2071–2074 (1999).
81. Manganiello, M. J., Cheng, C., Convertine, A. J., Bryers, J. D. & Stayton, P. S. Diblock copolymers with tunable pH transitions for gene delivery. *Biomaterials* **33**, 2301–2309 (2012).
82. O’Neil, C. P., Suzuki, T., Demurtas, D., Finka, A. & Hubbell, J. A. A novel method for the encapsulation of biomolecules into polymersomes via direct hydration. *Langmuir* **25**, 9025–9029 (2009).
83. Murthy, N., Robichaud, J. R., Tirrell, D. A., Stayton, P. S. & Hoffman, A. S. The design and synthesis of polymers for eukaryotic membrane disruption. *J. Control. Release* **61**, 137–143 (1999).
84. Rothen-Rutishauser, B. M., Schurch, S., Haenni, B., Kapp, N. & Gehr, P. Interaction of Fine Particle and Nanoparticles with Red Blood Cells Visualized with Advanced Microscopic Techniques. *Environ. Sci. Technol.* **40**, 4353–4359 (2006).
85. Ahmed, F. & Discher, D. E. Self-porating polymersomes of PEG-PLA and PEG-PCL: Hydrolysis-triggered controlled release vesicles. *J. Control. Release* **96**, 37–53 (2004).
86. Bermudez, H., Brannan, A. K., Hammer, D. A., Bates, F. S. & Discher, D. E. Molecular weight dependence of polymersome membrane structure, elasticity, and stability. *Macromolecules* **35**, 8203–8208 (2002).
87. Mai, Y. & Eisenberg, A. Self-assembly of block copolymers. *Chem. Soc. Rev.* **41**, 5969–5985 (2012).
88. Lee, J. C. *et al.* Preparation, Stability, and In Vitro Diblock Copolymers. *Biotechnology* **46**, 135–145 (2001).
89. Discher, D. E. & Ahmed, F. Polymersomes. *Annu. Rev. Biomed. Eng.* **8**, 323–341 (2006).
90. Jain, S. & Bates, F. S. Consequences of Nonergodicity in Aqueous Binary PEO-PB Micellar Dispersions. *Macromolecules* **37**, 1511–1523 (2004).
91. Battaglia, G. & Ryan, A. J. The evolution of vesicles from bulk lamellar gels. *Nat. Mater.* **4**, 869–876 (2005).
92. Alexandridis, P., Olsson, U. & Lindman, B. Structural Polymorphism of Amphiphilic Copolymers: Six Lyotropic Liquid Crystalline and Two Solution Phases in a Poly(oxybutylene)-b-poly(oxyethylene)-Water-Xylene System. *Langmuir* **13**, 23–34 (1997).
93. Parker, B. S., Rautela, J. & Hertzog, P. J. Antitumour actions of interferons: Implications for cancer therapy. *Nat. Rev. Cancer* **16**, 131–144 (2016).
94. Zitvogel, L., Galluzzi, L., Kepp, O., Smyth, M. J. & Kroemer, G. Type I interferons in anticancer immunity. *Nat. Rev. Immunol.* **15**, 405–414 (2015).
95. Yin, H. *et al.* Non-viral vectors for gene-based therapy. *J. World Trade* **51**, 43–66 (2017).
96. Wilson, D. R. *et al.* Biodegradable STING agonist nanoparticles for enhanced cancer immunotherapy. *Nanomedicine Nanotechnology, Biol. Med.* **14**, 237–246 (2018).
97. Ghosh, S., Basu, S. & Thayumanavan, S. Simultaneous and reversible functionalization of copolymers for biological applications. *Macromolecules* **39**, 5595–5597 (2006).
98. Matini, T. *et al.* Synthesis and characterization of variable conformation pH responsive

- block co-polymers for nucleic acid delivery and targeted cell entry. *Polym. Chem.* **5**, 1626–1636 (2014).
99. Gaffney, B. L., Veliath, E., Zhao, J. & Jones, R. A. One-Flask Synthesis of c-diGMP and the [Rp,Rp] and [Rp,Sp] Thiophosphate Analogues. *Org. Lett.* **12**, 3269–3271 (2010).
 100. Lechner, M. G. *et al.* Immunogenicity of murine solid tumor models as a defining feature of in vivo behavior and response to immunotherapy. *J. Immunother.* **36**, 477–489 (2013).
 101. Harlin, H. *et al.* Chemokine Expression in Melanoma Metastases Associated with CD8+ T-cell Recruitment. *Cancer Res.* **69**, 3077–3084 (2009).
 102. Corrales, L., McWhirter, S. M., Dubensky, T. W. & Gajewski, T. F. The host STING pathway at the interface of cancer and immunity. *J. Clin. Invest.* **126**, 2404–2411 (2016).
 103. Chen, Q., Sun, L. & Chen, Z. J. Regulation and function of the cGAS-STING pathway of cytosolic DNA sensing. *Nat. Immunol.* **17**, 1142–1149 (2016).
 104. Sokolowska, O. & Nowis, D. STING Signaling in Cancer Cells: Important or Not? *Arch. Immunol. Ther. Exp. (Warsz)*. **66**, 125–132 (2018).
 105. Galluzzi, L., Buqué, A., Kepp, O., Zitvogel, L. & Kroemer, G. Immunogenic cell death in cancer and infectious disease. *Nat. Rev. Immunol.* **17**, 97–111 (2017).
 106. Ahn, J., Xia, T., Rabasa Capote, A., Betancourt, D. & Barber, G. N. Extrinsic Phagocyte-Dependent STING Signaling Dictates the Immunogenicity of Dying Cells. *Cancer Cell* **33**, 862–873.e5 (2018).
 107. Walker, M. M., Crute, B. W., Cambier, J. C. & Getahun, A. B Cell–Intrinsic STING Signaling Triggers Cell Activation, Synergizes with B Cell Receptor Signals, and Promotes Antibody Responses. *J. Immunol.* **201**, 2641–2653 (2018).
 108. Tomura, M. *et al.* Tracking and quantification of dendritic cell migration and antigen trafficking between the skin and lymph nodes. *Sci. Rep.* **4**, 1–11 (2014).
 109. Crow, M. K. Type I Interferon in the Pathogenesis of Lupus. *J. Immunol.* **192**, 5459–5468 (2014).
 110. Majer, O. *et al.* Type I interferons promote fatal immunopathology by regulating inflammatory monocytes and neutrophils during *Candida* infections. *PLoS Pathog.* **8**, 10 (2012).
 111. Shaul, M. E. *et al.* Tumor-associated neutrophils display a distinct N1 profile following TGF β modulation: A transcriptomics analysis of pro- vs. antitumor TANs. *Oncoimmunology* **5**, 1–14 (2016).
 112. Fridlender, Z. G. *et al.* Polarization of Tumor-Associated Neutrophil Phenotype by TGF- β : ‘N1’ versus ‘N2’ TAN. *Cancer Cell* **16**, 183–194 (2009).
 113. Lizotte, P. H. *et al.* In situ vaccination with cowpea mosaic virus nanoparticles suppresses metastatic cancer. *Nat. Nanotechnol.* **11**, 295–303 (2016).
 114. Liang, H. *et al.* Host STING-dependent MDSC mobilization drives extrinsic radiation resistance. *Nat. Commun.* **8**, 1–10 (2017).
 115. Ries, C. H. *et al.* Targeting tumor-associated macrophages with anti-CSF-1R antibody reveals a strategy for cancer therapy. *Cancer Cell* **25**, 846–859 (2014).
 116. Rudqvist, N.-P. *et al.* Radiotherapy and CTLA-4 blockade shape the TCR repertoire of tumor-infiltrating T cells. *Cancer Immunol. Res.* canimm.0134.2017 (2017). doi:10.1158/2326-6066.CIR-17-0134
 117. Shi, L. *et al.* PD-1 blockade boosts radiofrequency ablation-elicited adaptive immune responses against tumor. *Clin. Cancer Res.* **22**, 1173–1184 (2016).
 118. Li, Z., Li, D., Tsun, A. & Li, B. FOXP3⁺ regulatory T cells and their functional regulation.

- Cell. Mol. Immunol.* **12**, 558–565 (2015).
119. Murthy, V., Minehart, J. & Serman, D. H. Local Immunotherapy of Cancer: Innovative Approaches to Harnessing Tumor-Specific Immune Responses. *JNCI J. Natl. Cancer Inst.* **109**, 1–12 (2017).
 120. Overwijk, W. W. *et al.* Tumor Regression and Autoimmunity after Reversal of a Functionally Tolerant State of Self-reactive CD8⁺ T Cells. *J. Exp. Med.* **198**, 569–580 (2003).
 121. Moynihan, K. D. *et al.* Eradication of large established tumors in mice by combination immunotherapy that engages innate and adaptive immune responses. *Nat. Med.* **22**, 1402–1410 (2016).
 122. Danhier, F. To exploit the tumor microenvironment: Since the EPR effect fails in the clinic, what is the future of nanomedicine? *J. Control. Release* **244**, 108–121 (2016).
 123. Ugel, S. *et al.* Immune Tolerance to Tumor Antigens Occurs in a Specialized Environment of the Spleen. *Cell Rep.* **2**, 628–639 (2012).
 124. Wu, C. *et al.* Spleen mediates a distinct hematopoietic progenitor response supporting tumor-promoting myelopoiesis. *J. Clin. Invest.* **128**, 3425–3438 (2018).
 125. Kumar, V., Patel, S., Tcyganov, E. & Gibrilovich, D. I. The Nature of Myeloid-Derived Suppressor Cells in the Tumor Microenvironment. *Trends Immunol.* **37**, 208–220 (2016).
 126. Smith, B. R. *et al.* Selective uptake of single-walled carbon nanotubes by circulating monocytes for enhanced tumour delivery. *Nat. Nanotechnol.* **9**, 481–487 (2014).
 127. Mak, I. W. Y., Evaniew, N. & Ghert, M. Lost in translation: Animal models and clinical trials in cancer treatment. *Am. J. Transl. Res.* **6**, 114–118 (2014).
 128. Conlon, J. *et al.* Mouse, but not Human STING, Binds and Signals in Response to the Vascular Disrupting Agent 5,6-Dimethylxanthenone-4-Acetic Acid. *J. Immunol.* **190**, 5216–5225 (2013).
 129. Kreiter, S. *et al.* Mutant MHC class II epitopes drive therapeutic immune responses to cancer. *Nature* **520**, 692–696 (2015).
 130. Castle, J. C. *et al.* Exploiting the mutanome for tumor vaccination. *Cancer Res.* **72**, 1081–1091 (2012).
 131. Whitmore, M. M. *et al.* Synergistic activation of innate immunity by double-stranded RNA and CpG DNA promotes enhanced antitumor activity. *Cancer Res.* **64**, 5850–5860 (2004).
 132. Ouyang, X. *et al.* Cooperation between MyD88 and TRIF pathways in TLR synergy via IRF5 activation. *Biochem. Biophys. Res. Commun.* **354**, 1045–1051 (2007).
 133. Shima, F., Uto, T., Akagi, T. & Akashi, M. Synergistic stimulation of antigen presenting cells via tlr by combining CpG ODN and Poly(γ -glutamic acid)-based nanoparticles as vaccine adjuvants. *Bioconjug. Chem.* **24**, 926–933 (2013).
 134. Temizoz, B. *et al.* TLR9 and STING agonists synergistically induce innate and adaptive type-II IFN. *Eur. J. Immunol.* **45**, 1159–1169 (2015).
 135. Li, M. X. *et al.* Prognostic role of neutrophil-to-lymphocyte ratio in colorectal cancer: A systematic review and meta-analysis. *Int. J. Cancer* **134**, 2403–2413 (2014).
 136. Yamanaka, T. *et al.* The baseline ratio of neutrophils to lymphocytes is associated with patient prognosis in advanced gastric cancer. *Oncology* **73**, 215–220 (2008).
 137. Coffelt, S. B., Wellenstein, M. D. & De Visser, K. E. Neutrophils in cancer: Neutral no more. *Nat. Rev. Cancer* **16**, 431–446 (2016).
 138. Gref, R., Lück, M. & Quellec, P. 'Stealth' corona-core nanoparticles surface modified by

- polyethylene glycol (PEG): influences of the corona (PEG chain length and surface density) and of the core. *Colloids Surfaces B ...* **18**, 301–313 (2000).
139. Pelaz, B. *et al.* Surface Functionalization of Nanoparticles with Polyethylene Glycol: Effects on Protein Adsorption and Cellular Uptake. *ACS Nano* **9**, 6996–7008 (2015).
 140. Liu, W. *et al.* Compact cysteine-coated CdSe(ZnCdS) quantum dots for in vivo applications. *J. Am. Chem. Soc.* **129**, 14530–14531 (2007).
 141. Jackson, M. A. *et al.* Zwitterionic Nanocarrier Surface Chemistry Improves siRNA Tumor Delivery and Silencing Activity Relative to Polyethylene Glycol. *ACS Nano* **11**, 5680–5696 (2017).
 142. Keler, T., Ramakrishna, V. & Fanger, M. W. Mannose receptor-targeted vaccines. *Expert Opin. Biol. Ther.* **4**, 1953–1962 (2004).
 143. Rosalia, R. A. *et al.* CD40-targeted dendritic cell delivery of PLGA-nanoparticle vaccines induce potent anti-tumor responses. *Biomaterials* **40**, 88–97 (2015).
 144. Hatzifoti, C. & Heath, A. W. CD40-mediated enhancement of immune responses against three forms of influenza vaccine. *Immunology* **122**, 98–106 (2007).
 145. Tang, L. *et al.* Enhancing T cell therapy through TCR-signaling-responsive nanoparticle drug delivery. *Nat. Biotechnol.* **36**, (2018).

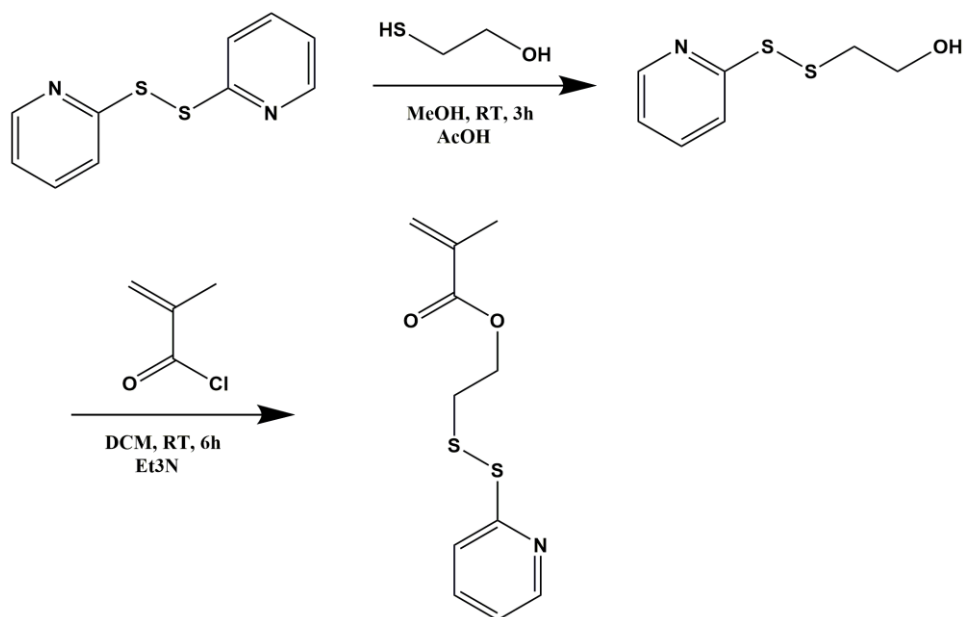
Appendix

Appendix A.1

Frequency x_i	Diameter (nm)
.034	50.8
.127	58.7
.206	68.0
.210	78.8
.161	91.2
.106	105.7
.064	122.4
.037	141.8
.021	164.2
.013	190.1
.008	220.2
.005	255.0
.003	295.3
.002	342.0
.001	396.1
.001	458.7

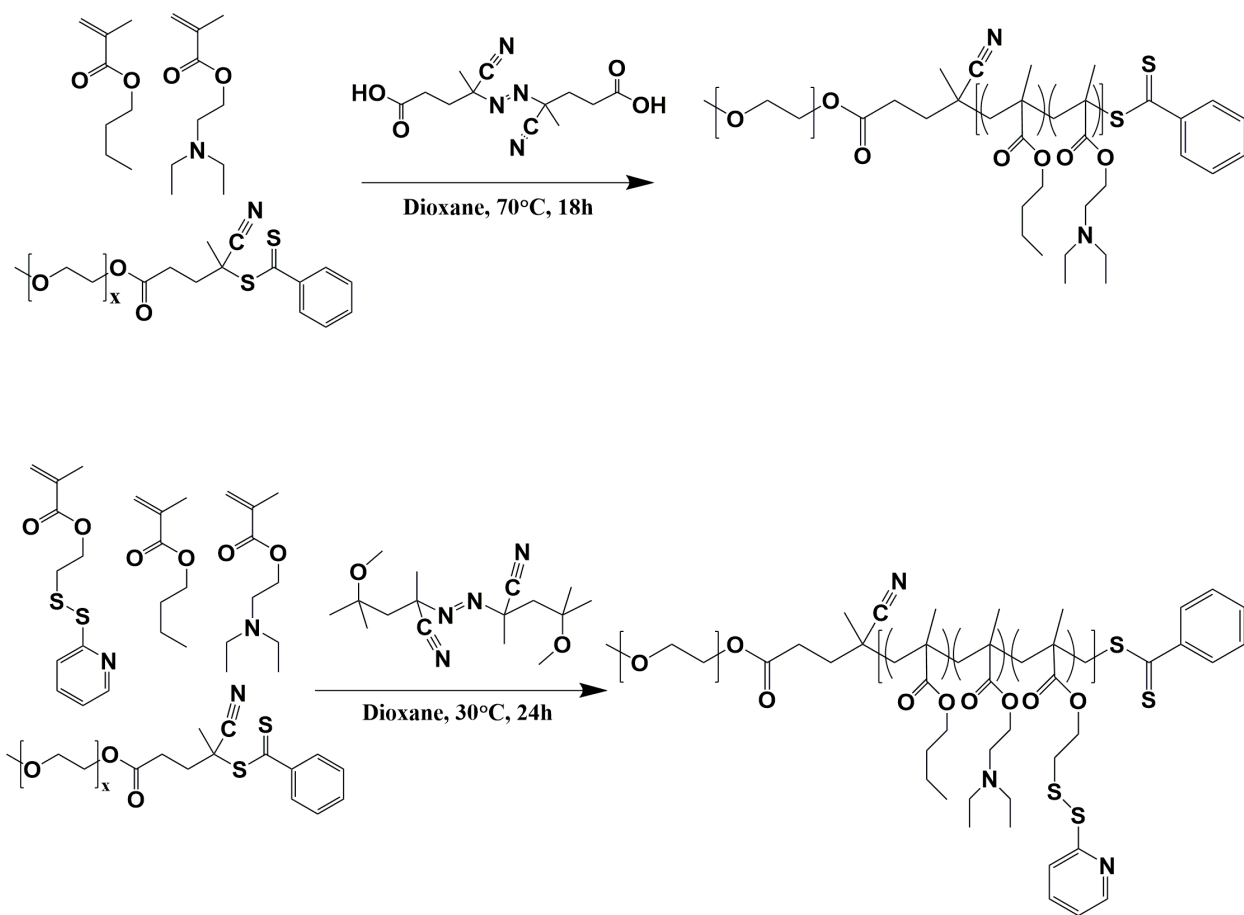
Nanoparticle size distribution used for theoretical encapsulation efficiency calculations. Size distribution was determined by dynamic light scattering and represents the number average hydrodynamic radius.

Appendix A.2



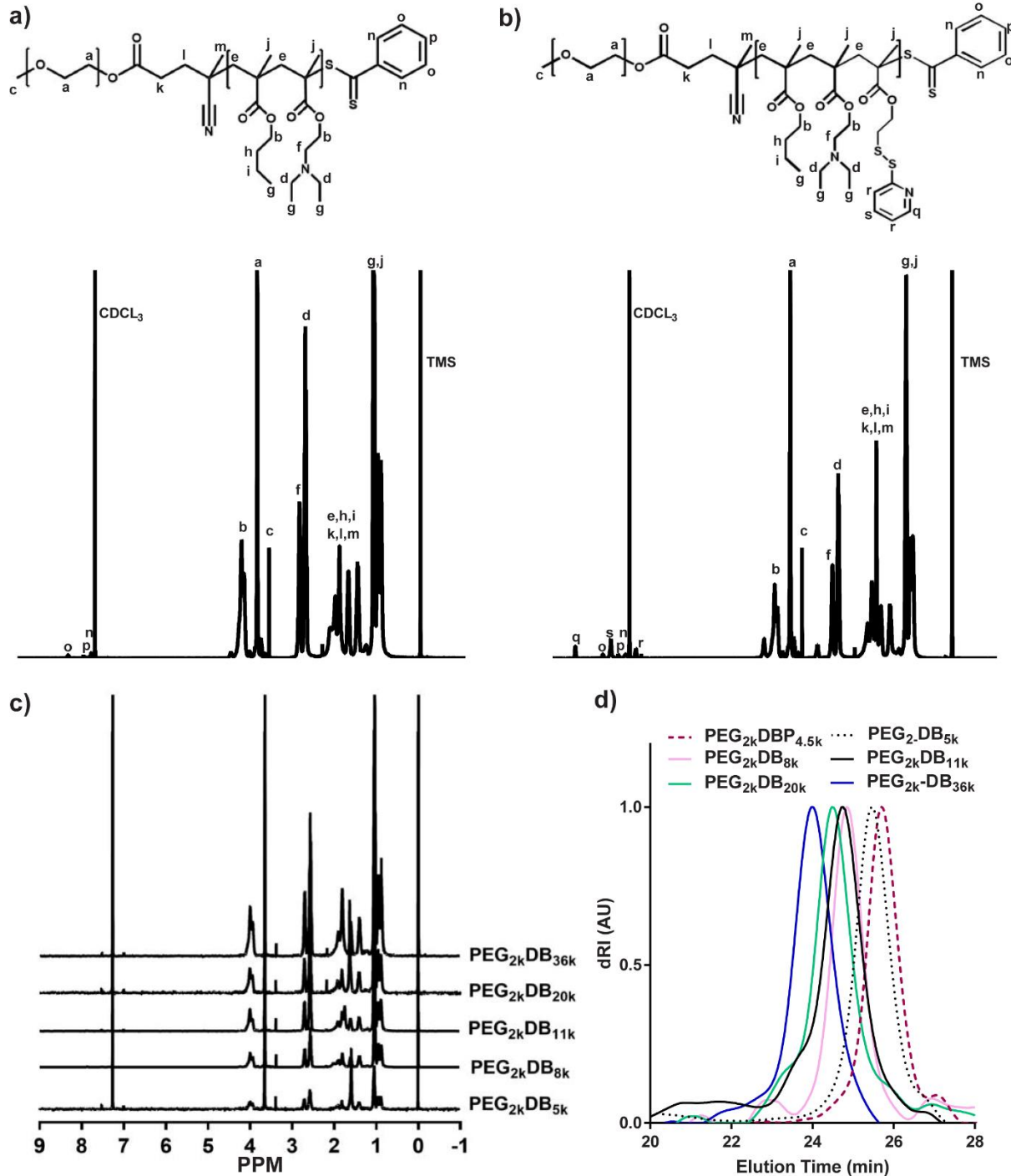
Synthetic scheme for PDSMA.⁹⁷

Appendix A.3



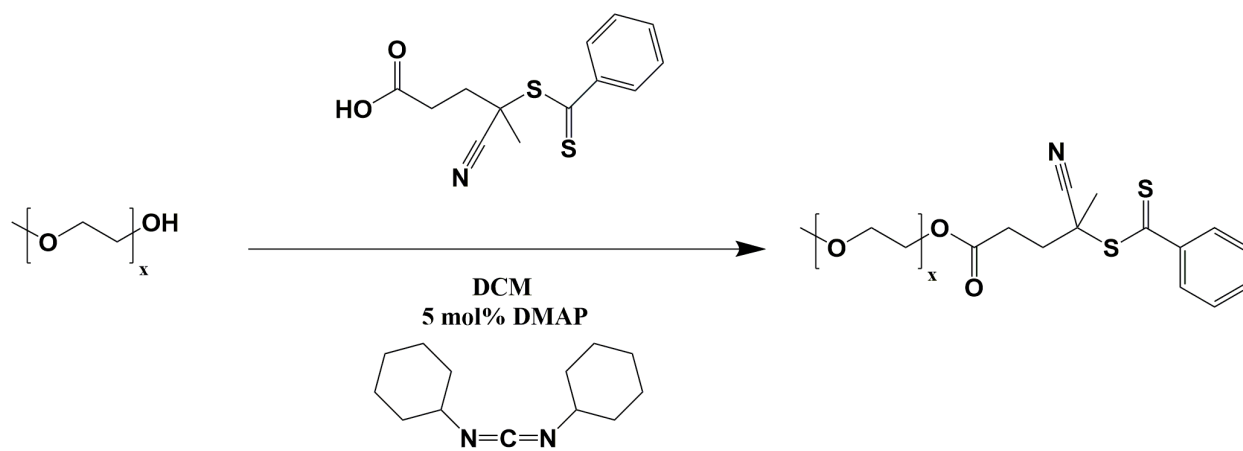
Synthetic scheme for PEG-DB and PEG-EBP block copolymers.

Appendix A.4



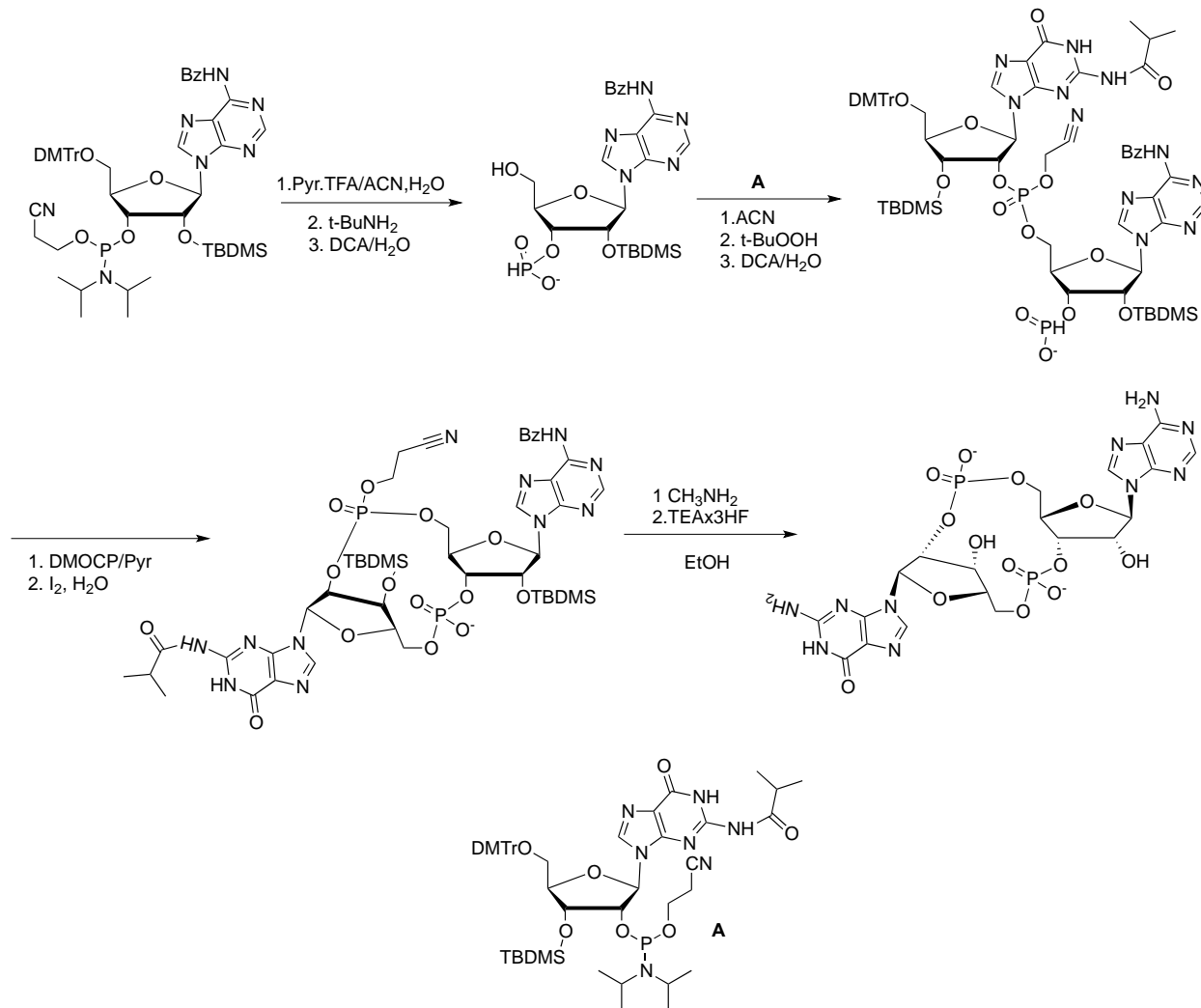
^1H NMR and GPC Characterization of pH-responsive diblock polymers. a) Representative ^1H NMR spectrum of poly[(ethylene glycol)-b-(((2-(diethylamino)ethyl methacrylate)-c-(butyl methacrylate)))] polymer (PEG-b-DB). b) spectrum of poly[(ethylene glycol)-b-(((2-(diethylamino)ethyl methacrylate)-c-(butyl methacrylate)-c-(pyridyl disulfide ethyl methacrylate)))] polymer. c) Stacked plot of PEG_{2k}-b-DB_x ^1H NMR spectra. d) GPC chromatograms of PEG_{2k}-DB_x polymers and PEG_{2k}-DBP_{4.5k}.

Appendix A.5



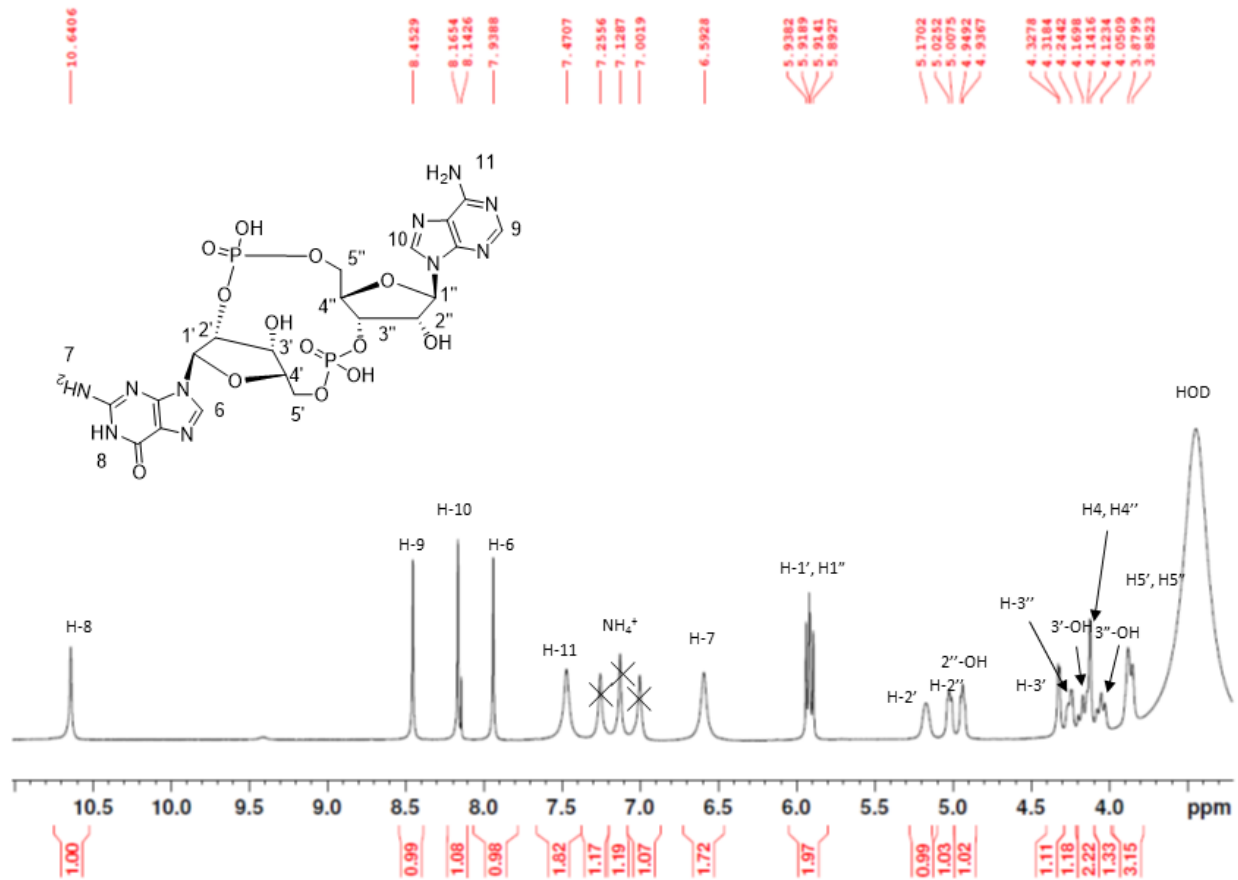
Synthetic scheme for PEG-CTA synthesis.

Appendix A.6



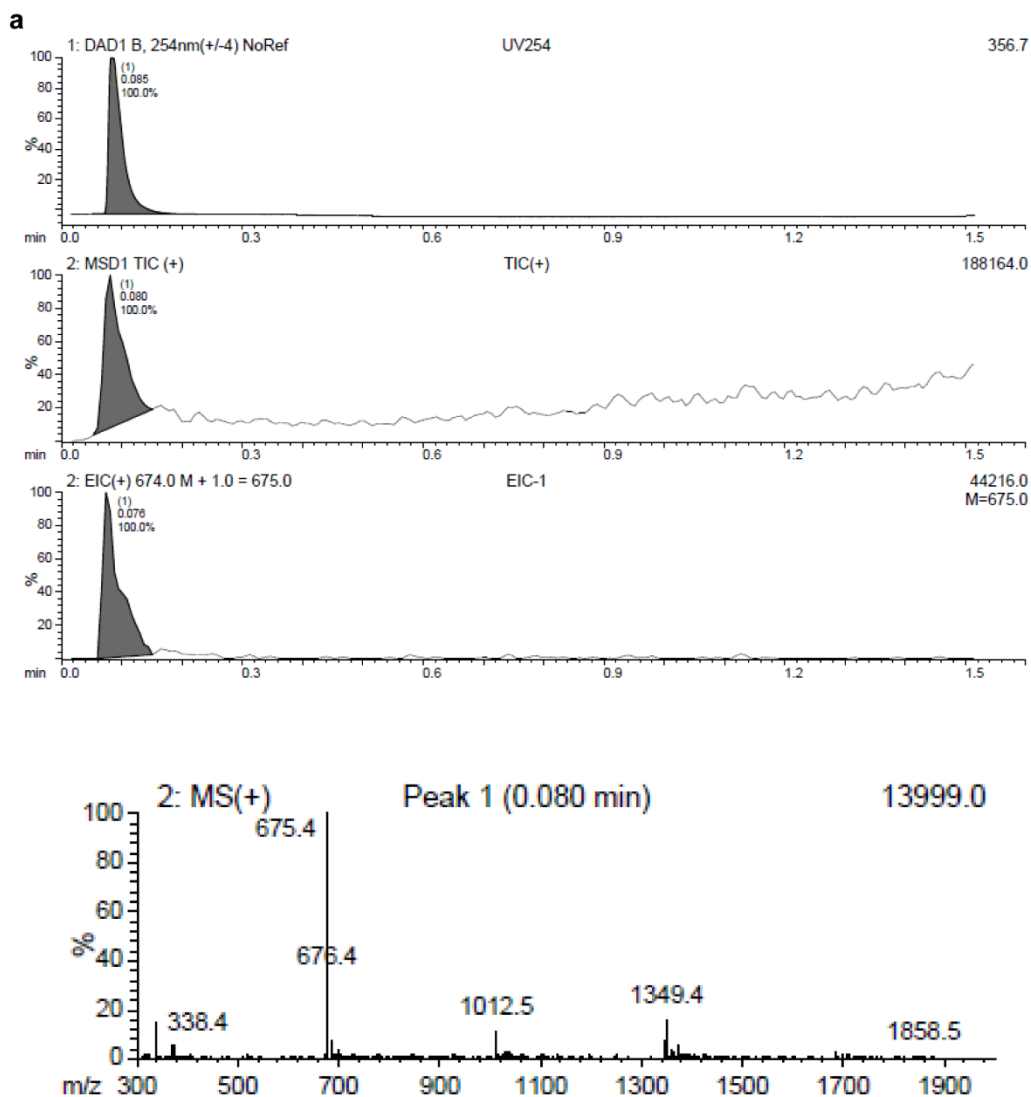
Synthetic scheme for 2'3'-cGAMP.

Appendix A.7



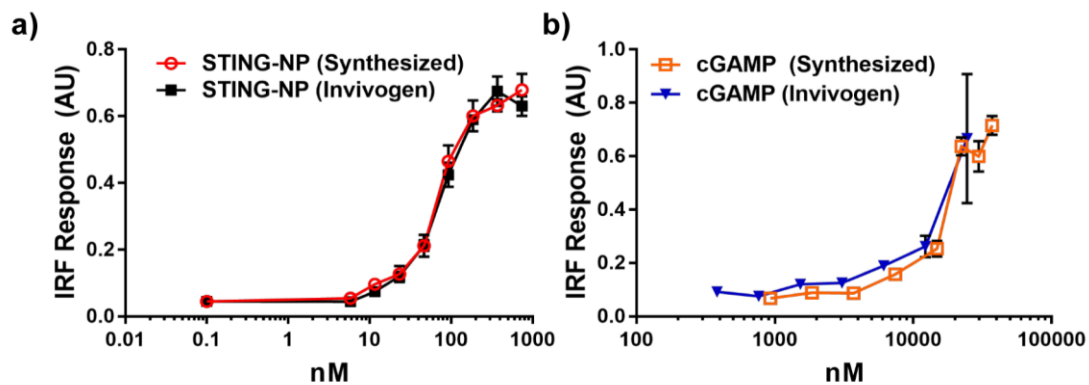
¹H-NMR spectrum of synthesized 2'3-cGAMP. ¹H-NMR (DMSO-d₆) δ 10.64 (broad s, H-8), 8.45 (s, 1H, H-9), 8.16 (s, 1H, H-10), 7.93 (s, 1H, H-6), 7.47 (broad s, 2H, H-11), 6.59 (broad s, 1H, H-7), 5.92 (d, 1H, *J* = 8 Hz, H-1'), 5.90 (d, 1H, *J* = 8 Hz, H-1''), 5.17 (m, 1H, H-2'), 5.01 (m, 1H, H-2''), 4.92 (m, 1H, 2''-OH), 4.32 (m, 1H, H-3'), 4.24 (m, 1H, H-3''), 4.16 (m, 1H, 3'-OH), 4.14 (m, 2H, H-4' and H-4), 4.05 (m, 1H, 3'''-OH), 3.86 (m, 2H, H-5' and H-5'').

Appendix A.8



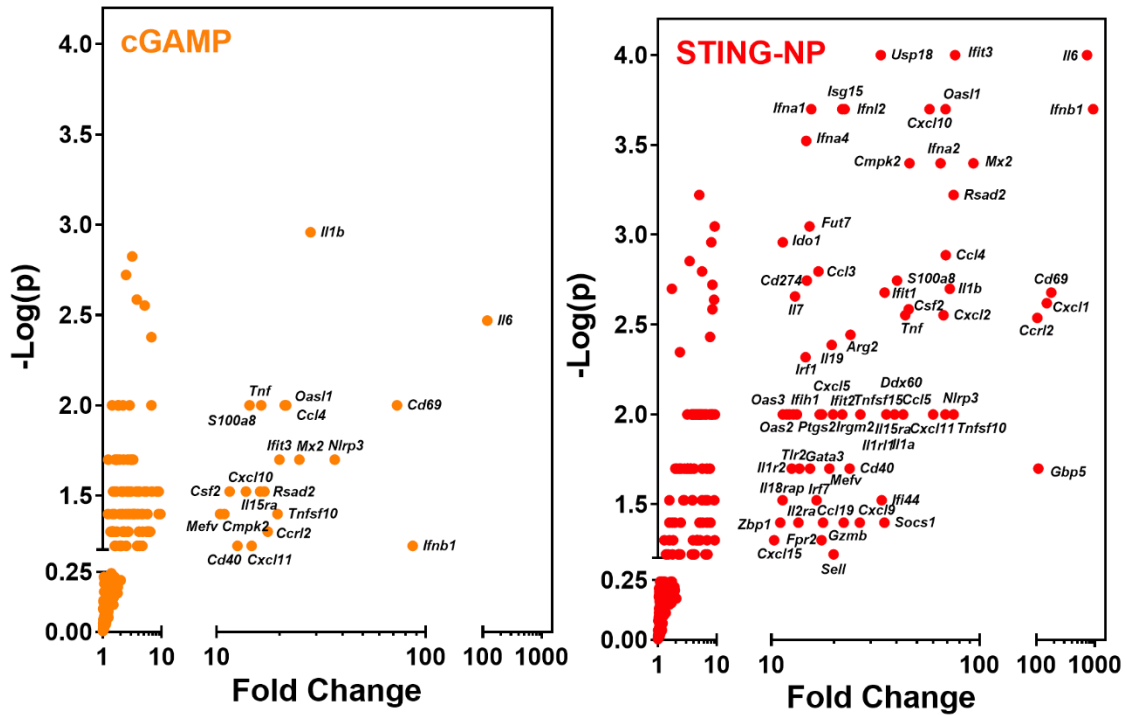
LCMS characterization of 2'3'-cGAMP. Mass calculated for $C_{20}H_{24}N_{10}O_{13}P_2$, 674.4; m/z found, 675.0 [M + H]⁺, Rf = 0.08

Appendix A.9



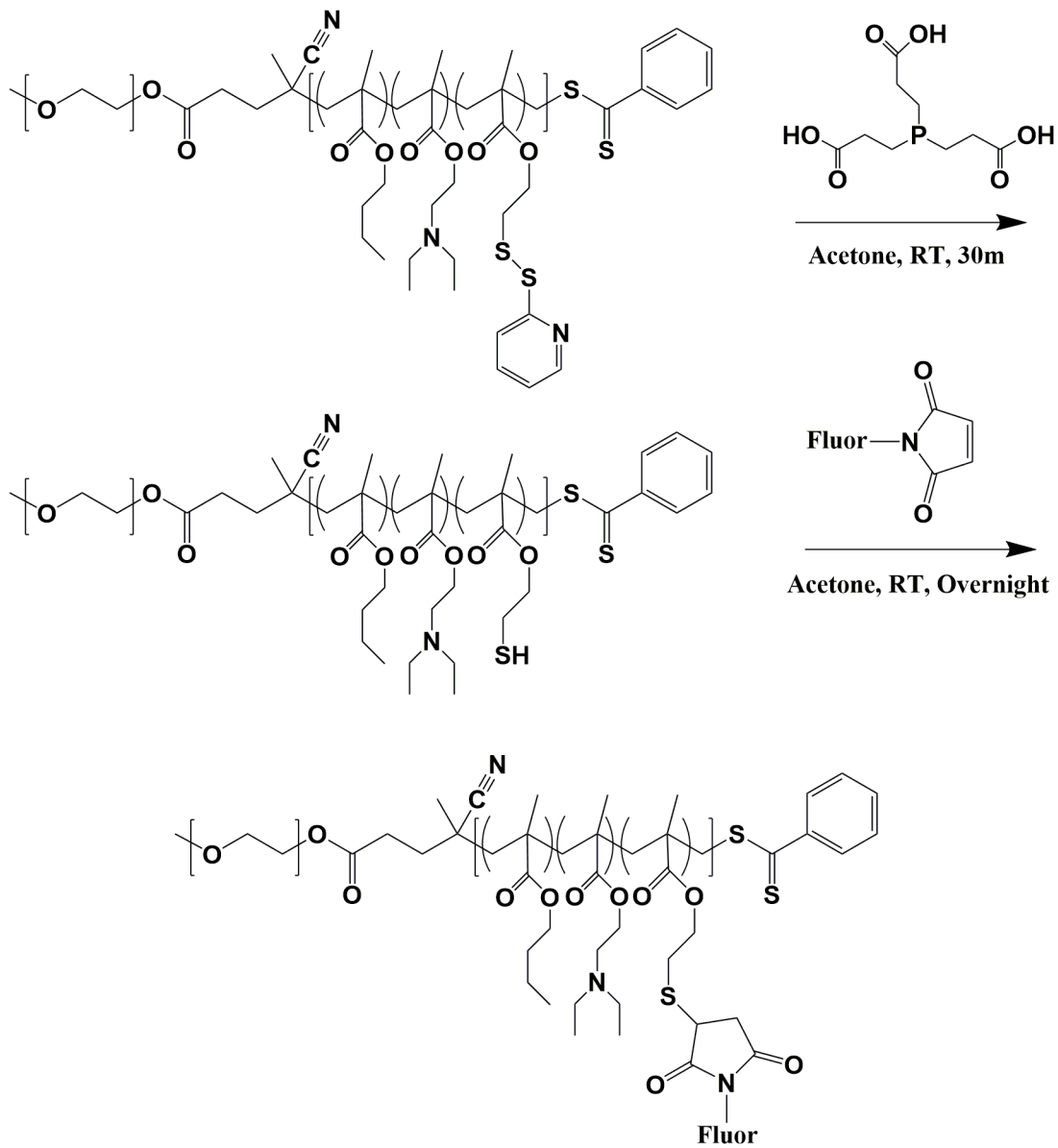
Comparison of biological activity of synthesized and commercially available 2'3'-cGAMP. a) Dose response curve of STING-NPs formulated with 2'3'-cGAMP produced in house or purchased from Invivogen in THP-1 ISG reporter cell lines. b) Activity dose curve of free 2'3'-cGAMP in THP-1 ISG reporter cell lines.

Appendix B.1



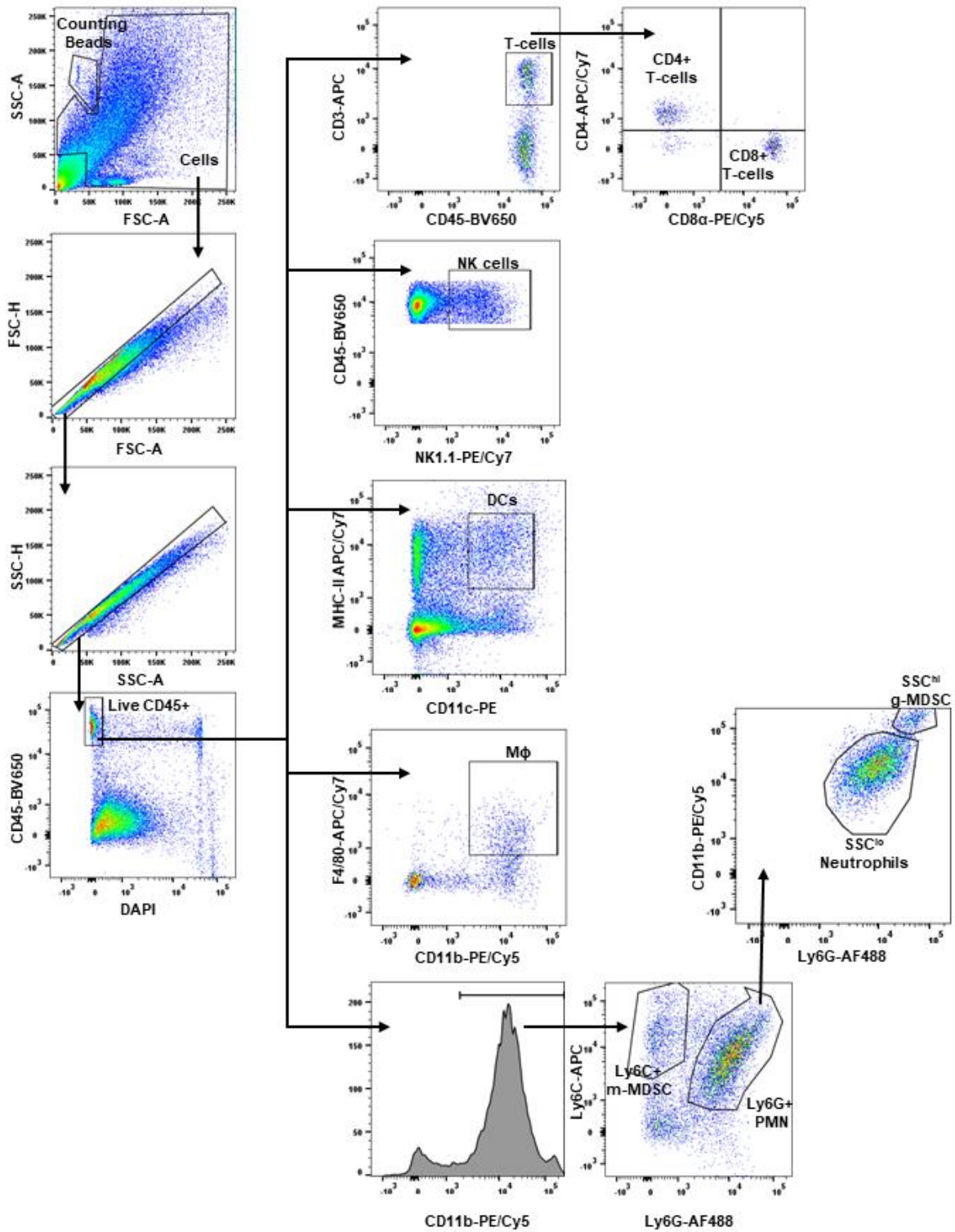
Nanostring analysis of upregulated genes following IT STING-NP or cGAMP treatment. cGAMP treatment triggers upregulation of several of the same genes as does STING-NP treatment, but mostly with a lower magnitude fold change and higher p value. Fold change is calculated with respect to PBS treated control tumors. Genes with a greater than 10 fold change are denoted.

Appendix B.2



Synthetic scheme for fluorescent polymer labeling.

Appendix B.3



Gating scheme for flow cytometric analysis of immune cell populations in the TME. Cells were stained separately with distinct panels of antibody conjugated fluorophores for analysis.